Transition Metal Oxides as Selective Carrier Transport Layers in Silicon Heterojunction Solar Cells

Cao, L.

DOI
10.4233/uuid:ab96d1a2-58a3-4966-b180-0e8eb5a4936a

Publication date
2025

Document Version
Final published version

Citation (APA)
Cao, L. (2025). *Transition Metal Oxides as Selective Carrier Transport Layers in Silicon Heterojunction Solar Cells*. [Dissertation (TU Delft), Delft University of Technology]. https://doi.org/10.4233/uuid:ab96d1a2-58a3-4966-b180-0e8eb5a4936a

Transition Metal Oxides as Selective Carrier Transport Layers in Silicon Heterojunction Solar Cells

Liqi CAO

曹立奇

Transition Metal Oxides as Selective Carrier Transport Layers in Silicon Heterojunction Solar Cells

Proefschrift

ter verkrijging van de graad van doctor
aan de Technische Universiteit Delft,
op gezag van de Rector Magnificus Prof. dr. ir. T.H.J.J. van der Hagen,
voorzitter van het College voor Promoties,
in het openbaar te verdedigen op donderdag 30 januari 2025 om 10:00 uur

door

Liqi CAO

Dit proefschrift is goedgekeurd door de promotoren.

Samenstelling promotiecommissie bestaat uit:

Em.prof.dr. M. Zeman	Technische Universiteit Delft, promotor
Prof.dr.ir. O. Isabella	Technische Universiteit Delft, promotor
Dr. L. Mazzarella	Technische Universiteit Delft, copromotor

Onafhankelijke leden:

Prof.dr. F.C. Grozema	Technische Universiteit Delft
Prof.dr. I.M.F. Gordon	Technische Universiteit Delft
Dr.rer.nat. S. Essig	University of Stuttgart, Stuttgart, Germany
Prof.dr. P. Gao	Sun Yat-Sen University, Shenzheng, China
Prof.dr.ir. P. Bauer	Technische Universiteit Delft, reservelid

Keywords: transition metal oxide (TMO), interface engineering method, indium use reduction, c-Si solar cells

Printed by: Gildeprint Printing

Front & Back: Designed by L. Cao and Y. Wang utilizing DALL·E along with Adobe Photoshop.

ISBN 978-94-6496-337-3

An electronic version of this dissertation is available at
`http://repository.tudelft.nl/`.

To my parents

献给我的父母

Contents

Summary ix

Samenvatting xi

Nomenclature xiii

1 Introduction 1
- 1.1 Sustainable energy: an urgent path forward . . . 1
- 1.2 Photovoltaic cell technology . . . 2
  - 1.2.1 Innovations in photovoltaic cell technologies . . . 2
  - 1.2.2 Dopant-free materials applied in silicon solar cell . . . 6
- 1.3 Motivation . . . 6
- 1.4 Outline of this thesis . . . 7
- 1.5 Main contributions to the field . . . 8

2 TMO in c-Si solar cells: mechanisms and challenges 11
- 2.1 Working principle of TMO materials in SHJ solar cells . . . 11
- 2.2 TMO materials choice for devices . . . 12
  - 2.2.1 Original passivation of TMO materials in silicon solar cell . . . 12
  - 2.2.2 Electron transport materials . . . 13
  - 2.2.3 Hole transport materials . . . 13
  - 2.2.4 Interaction of TMO and Si substrate . . . 13
- 2.3 The opto-electrical properties of TMOs . . . 15
- 2.4 TMO deposition technology . . . 17
- 2.5 Architecture of SHJ solar cells with dopant-free HTLs . . . 18
- 2.6 Conclusion . . . 20

3 23.83% efficiency SHJ solar cells with ultra-thin MoO_x layer 21
- 3.1 Introduction . . . 22
- 3.2 Methodology . . . 23
  - 3.2.1 Experimental . . . 23
  - 3.2.2 Simulations . . . 24
- 3.3 Results and Discussion . . . 25
  - 3.3.1 Significance of Si/MoO_x interface . . . 25
  - 3.3.2 Modification of (*i*)a-Si:H to control the properties of MoO_x . . . 27
  - 3.3.3 The role of oxygen at (*i*)a-Si:H/MoO_x interface . . . 28
  - 3.3.4 Solar cells' performance . . . 30
- 3.4 Conclusion . . . 30

4 Indium reduction in bifacial SHJ solar cells with MoO_x collector 33
4.1 Introduction . . . 34
4.2 Experiment . . . 35
4.2.1 Solar cells with different *n*-type layers . . . 35
4.2.2 Deposition of IWO films . . . 36
4.2.3 Characterizations . . . 36
4.3 Results and discussion . . . 36
4.3.1 The influence of different *n*-type layers on cell performance . . . 36
4.3.2 Optical and electrical properties of IWO . . . 38
4.3.3 Optical simulation results with ultra-thin IWO . . . 39
4.3.4 Ultra-thin IWO layers for bifacial silicon heterojunction solar cells . 41
4.4 Conclusion . . . 43

5 Universal interface engineering method for applying TMO in SHJ solar cell 45
5.1 Introduction . . . 46
5.2 Experimental methods . . . 47
5.3 Result and discussion . . . 49
5.3.1 Control the oxygen content of WO_x and V_2O_x . . . 49
5.3.2 Performance of WO_x-based SHJ solar cells . . . 50
5.3.3 Performance of V_2O_x-based SHJ solar cells . . . 53
5.4 Conclusion . . . 55

6 Conclusions and outlook 57
6.1 Conclusions . . . 57
6.2 Outlook . . . 58

Appendices: 63

A 23.83% Efficiency SHJ Solar Cells with Ultra-Thin MoO_x Layer 63

B Indium reduction in bifacial SHJ solar cells with MoO_x collector 71

C Universal interface engineering method for applying TMO in SHJ solar cell 77

Bibliography 81

Acknowledgements 111

List of Publications 115

Curriculum Vitae 119

Summary

Silicon heterojunction (SHJ) technology is gaining increasing attention due to its low-temperature and simple fabrication process. Intrinsic hydrogenated amorphous silicon ((*i*)a-Si:H) serves as a passivation layer, providing excellent chemical passivation, while doped a-Si:H offers good field passivation and selective contact. Thanks to these features, SHJ has achieved a high conversion efficiency of 27.09%, approaching the theoretical limit for silicon-based solar cells. However, achieving excellent passivation performance results in optical and electrical losses, as the band gap of doped a-Si:H causes parasitic absorption. One strategy to address this issue is to replace the doped layer with transition metal oxides (TMOs), which can enable selective contact due to their high or low work functions. Few researchers have integrated TMOs in silicon-based solar cells to replace silicon-based doped thin films as selective contact layers. Wide-bandgap TMOs improve the optical performance of the cells. However, interface reaction between TMOs and the silicon substrate becomes an issue limiting the electronic properties of the device.

In this research, we first present three different interface engineering methods: no plasma treatment (noPT), plasma treatment (PT), and plasma treatment with boron (PTB). We applied these methods to SHJ solar cells with MoO_x ($2.9 < x < 3$) as the hole transport layer (HTL). MoO_x thin-film is deposited by thermal evaporation. The methods were implemented at the MoO_x/(*i*)a-Si:H interface. Additionally, to address sustainability concerns related to indium consumption and fully exploit the optical advantages of MoO_x, we propose bifacial SHJ solar cells with MoO_x as the HTL to reduce the thickness indium doped tin oxide (ITO) films. Furthermore, to test the capability of these interface engineering methods with other TMO materials, we used WO_x ($2.9 < x < 3$) and V_2O_x ($2.9 < x < 3$) as the hole transport films in SHJ solar cells. The TMO thin-films are deposited by thermal evaporation. The specific results are summarized as follows.

Chapter 3 explores using MoO_x as a HTL to address these issues. By tailoring the interface between MoO_x and (*i*)a-Si:H using interface engineering methods, the oxygen content in MoO_x layers has been successfully optimized. The PTB method reduces the formation of SiO_x layer resulting in improved electronic properties and low contact resistivity. PTB treated samples showed the best performance, with high open-circuit voltage (V_{OC}) and fill factor (*FF*). This approach achieved a certified conversion efficiency of 23.83% with an ultra-thin MoO_x layer of 1.7 nm. Notably, a short-circuit current density (J_{SC}) above 40 mA/cm² has been achieved.

Chapter 4 explores reducing indium consumption by optimizing *n*-contacts as electron collector layer and MoO_x as a hole collector layer. Bifacial SHJ solar cells with MoO_x as the HTL and various electron transport layers (ETL) were fabricated and optimized using optical simulations. The results showed that bilayer ((*n*)nc-Si:H/a-Si:H) and trilayer ((*n*)nc-SiO_x:H/nc-Si:H/a-Si:H) better than monolayer (a-Si:H) in electronic and optical performance. The use of ultra-thin transparent conductive oxide (TCO) layers combined with MgF_2 as double layer antireflection coatings (DLARC) significantly reduced TCO con-

sumption while maintaining high performance. Devices exhibiting 10-nm thick indium tungsten oxide (IWO) on both side and bilayer *n*-contact achieved certified efficiencies of 21.66% and 20.66% when measured from the MoO_x and *n*-contact side, respectively. This device realizes 90% TCO-reduction. The best-performing bifacial cells exhibited conversion efficiencies of 23.25% and 22.75% measuring from front and back side, respectively. The bifaciality factor of the champion device is 0.96. It demonstrates over 67% reduction in TCO usage compared to traditional SHJ solar cells. This study successfully shows that reducing TCO thickness and optimizing the interface with MoO_x can lead to high-efficiency bifacial SHJ solar cells, contributing to sustainability challenges related to indium consumption.

Chapter 5 investigates the application of TMOs like WO_x, and V_2O_x as HTLs combined with interface engineering methods in SHJ solar cells. The study aims to investigate the applicability of interface engineering methods to other TMOs. X-ray photoelectron spectroscopy (XPS) is employed to measure oxygen content and defects within TMO films. The XPS results demonstrate that PTB resulted in higher oxygen content and fewer oxygen vacancies. The optimal WO_x thickness was found to be 2 nm, achieving a champion cell with 23.30% efficiency with PTB and improved *FF* of over 80%. Similarly, with PTB method, the highest efficiency of 22.04% has been realized with 3-nm thick V_2O_x layer. The PTB method effectively controlled interface reactions, leading to better electronic properties of TMOs. The study concludes that the PTB method offers suitable interface conditions for depositing TMOs, enhancing SHJ solar cell performance.

Our findings in this study may provide valuable insights into applying TMOs in SHJ solar cells to achieve high performance. With optimized interface engineering methods, we can significantly reduce the optimal thickness of TMOs and achieve world-record efficiency. Furthermore, by applying TMOs in bifacial SHJ solar cells, we can decrease the thickness of indium-based TCOs, realizing both high efficiency and high bifaciality factor. This approach makes it possible to develop sustainable and efficient solar cells.

Samenvatting

Dutch translation by Google translate and modified by Peer Sluijs.

De technologie van silicium-heterojunctie (SHJ) krijgt steeds meer aandacht vanwege het lage temperatuur en het eenvoudige fabricageproces. Intrinsiek gehydrogeneerd amorf silicium ((*i*)a-Si:H) fungeert als een passivatielaag, die uitstekende chemische passivatie biedt, terwijl gedoteerd a-Si:H goede veldpassivatie en selectief contact biedt. Dankzij deze eigenschappen heeft SHJ een hoge conversie-efficiëntie van 27,09% bereikt, wat dicht in de buurt komt van de theoretische limiet voor siliciumgebaseerde zonnecellen. Het bereiken van uitstekende passivatieresultaten leidt echter tot optische en elektrische verliezen, aangezien de bandkloof van (*p*)a-Si:H parasitaire absorptie veroorzaakt. Een strategie om dit probleem aan te pakken is het vervangen van de gedoteerde laag door overgangsmetaaloxiden (TMO's), die selectief contact kunnen mogelijk maken vanwege hun hoge of lage werkfuncties. Veel onderzoekers hebben TMO's geïntegreerd in siliciumgebaseerde zonnecellen om siliciumgebaseerde dunne gedoteerde films te vervangen als selectieve contactlagen. TMO's met een brede bandkloof verbeteren de optische prestaties van de cellen. Echter, de interface-reactie tussen TMO's en het siliciumsubstraat wordt een probleem dat de elektronische eigenschappen van het apparaat beperkt.

In dit onderzoek presenteren we eerst drie verschillende interface-engineering methoden: geen plasmabehandeling (noPT), plasmabehandeling (PT) en plasmabehandeling met boor (PTB). We hebben deze methoden toegepast op SHJ-zonnecellen met MoO_x ($2.9 < x < 3$) als de gatentransportlaag (HTL). De methoden werden geïmplementeerd op de MoO_x/(*i*)a-Si:H interface. ovendien, om de zorgen over de duurzaamheid in verband met het indium gebruik aan te pakken en volledig te profiteren van de optische voordelen van MoO_x, stellen we bifaciale SHJ-zonnecellen voor met MoO_x als de HTL. Verder, om de capaciteit van deze interface-engineeringmethoden met andere TMO-materialen te testen, hebben we WO_x ($2.9 < x < 3$) en V_2O_x ($2.9 < x < 3$) gebruikt als de gatentransportlagen in SHJ-zonnecellen. De specifieke resultaten worden als volgt samengevat.

Chapter 3 onderzoekt het gebruik van MoO_x als een HTL om deze problemen aan te pakken. Door de interface tussen MoO_x en (*i*)a-Si:H aan te passen met interface-engineering methoden, is het zuurstofgehalte in MoO_x-lagen met succes geoptimaliseerd. De PTB-methode vermindert de vorming van SiO_x-lagen, wat resulteert in verbeterde elektronische eigenschappen en een lage contactweerstand. PTB-behandelde monsters vertoonden de beste prestaties, met een hoge open-klemspanning (V_{OC}) en vullingsfactor (*FF*). Deze aanpak behaalde een conversie-efficiëntie van 23,83% met een ultradunne MoO_x-laag van 1,7 nm. Opmerkelijk is dat een kortsluitstroomdichtheid (J_{SC}) boven 40 mA/cm² is bereikt.

Chapter 4 onderzoekt het verminderen van het indiumverbruik door de *n*-contacten te optimaliseren als elektronenverzamelaarlaag en MoO_x als een gatverzamelaarlaag.

Bifaciale SHJ-zonnecellen met MoO_x als de HTL en verschillende elektronentransportlagen (ETL) werden vervaardigd en geoptimaliseerd met behulp van optische simulaties. De resultaten toonden aan dat de dubbellaags ((*n*)nc-Si:H/a-Si:H) en drielaag ((*n*)nc-SiO_x:H/nc-Si:H/a-Si:H) beter presteren dan een enkele laag (a-Si:H) in elektronische en optische prestaties. Het gebruik van ultradunne transparante geleidende oxide (TCO)-lagen in combinatie met MgF_2 als dubbele laag antireflectiecoatings (DLARC) verminderde het TCO-verbruik aanzienlijk, terwijl de prestaties hoog bleven. Apparaten met een 10-nm dikke indium-wolfraamoxide (IWO) aan beide zijden en een dubbellaag *n*-contact bereikten gecertificeerde efficiënties van 21,66% en 20,66% wanneer er gemeten wordt vanaf respectievelijk de MoO_x- en *n*-contactzijde. Dit apparaat realiseerde een vermindering van 90% van het TCO-verbruik. De best presterende bifaciale cellen vertoonden conversie-efficiënties van 23,25% en 22,75% gemeten vanaf de voor- en achterkant, respectievelijk. De bifacialiteitsfactor van het best presterende apparaat is 0,96. Dit demonstreet dat er meer dan 67% TCO-verbruik is gereduceerd in vergelijking met traditionele SHJ-zonnecellen. Deze studie toont met succes aan dat het verminderen van de TCO-dikte en het optimaliseren van de interface met MoO_x kan leiden tot bifaciale SHJ-zonnecellen met hoge efficiëntie, wat bijdraagt aan duurzaamheidsuitdagingen met betrekking tot het indiumverbruik.

Chapter 5 onderzoekt de toepassing van TMO's zoals WO_x en V_2O_x als HTL's, gecombineerd met interface-engineeringmethoden in SHJ-zonnecellen. Het onderzoek richt zich op de toepasbaarheid van interface-engineeringmethoden voor andere TMO's. Röntgenfoto elektronspectroscopie (XPS) wordt gebruikt om het zuurstofgehalte en defecten in TMO-films te meten. De XPS-resultaten tonen aan dat PTB resulteerde in een hoger zuurstofgehalte en minder zuurstofvacatures. De optimale WO_x-dikte bleek 2 nm te zijn, waarbij een kampioenscel een efficiëntie van 23,30% bereikte met PTB en een verbeterde *FF* van meer dan 80%. Evenzo werd met de PTB-methode de hoogste efficiëntie van 22,04% gerealiseerd met een 3 nm dikke V_2O_x-laag. De PTB-methode controleerde effectief interface-reacties, wat leidde tot betere elektronische eigenschappen van TMO's. Het onderzoek concludeert dat de PTB-methode geschikte interfaceomstandigheden biedt voor de depositie van TMO's, wat de prestaties van SHJ-zonnecellen verbetert.

Onze bevindingen in dit onderzoek kunnen waardevolle inzichten bieden in de toepassing van TMO's in SHJ-zonnecellen om hoge prestaties te bereiken. Met geoptimaliseerde interface-engineeringmethoden kunnen we de optimale dikte van TMO's aanzienlijk verminderen en een wereldrecordefficiëntie bereiken. Bovendien kunnen we door TMO's toe te passen in bifaciale SHJ-zonnecellen de dikte van indiumgebaseerde TCO's verminderen, waardoor zowel een hoge efficiëntie als een hoge bifacialiteitsfactor wordt gerealiseerd. Deze aanpak maakt het mogelijk om duurzame en efficiënte zonnecellen te ontwikkelen.

Nomenclature

Abbreviations

AZO	aluminum doped zinc oxide
DLARC	double-layer anti-reflection coating
EDX	energy dispersive X-Ray spectroscopy
EQE	external quantum efficiency
ETL	electron transport layer
FBC	front/back-contacted
GHG	greenhouse gase
GISS	Goddard Institute for Space Studies
HTL	hole transport layer
IBC	interdigitated back contact cell
ITO	indium tin oxide (or, tin-doped indium oxide)
IWO	tungsten-doped indium oxide
LiF	lithiumfluoride
MF	monofacial
MgF_2	magnesium fluoride
MoO_3	molybdenum oxide
noPT	without plasma treatment
PECVD	plasma enhanced chemical vapour deposition
PERC	passivated emitter and rear cell
PT	plasma treatment
PTB	plasma treatment with boron
PV	photovoltaic
SHJ	silicon heterojunction
STC	standard test condition
TAT	trap-assisted tunnelling
TCO	transparent conductive oxide
TEM	transmission electron microscope
TiO_2	titanium oxide
TMO	transition metal oxide
TOPCon	tunnel oxide passivated contact
V_2O_5	vanadium oxide
WF	work function, eV
WO_3	tungsten oxide
XPS	X-ray photoelectron spectrometer

Letters

ρ	resistivity, Ω cm
σ	conductivity, S/cm
μ	carrier mobility, $cm^2 V^{-1} s^{-1}$
τ	carrier relaxation time
λ	wavelength, nm
α	absorption coefficient, cm^{-1}
η	power conversion efficiency, %
ρ_c	contact resistivity, mΩ cm^2
φ	bifaciality factor
N	carrier density, cm^{-3}
A	absorptance, %
R	reflectance, %
T	transmittance, %
n	refractive index, -
k	extinction coefficient, -
E_g	band gap, eV
E_U	Urbach energy, meV
E_{vac}	vacuum level energy
E_F	Fermi energy, eV
E_c	conduction band energy, eV
Δn	excess carrier density under illumination, cm^{-3}
V_{OC}	open-circuit voltage, mV
i-V_{OC}	implied open-circuit voltage, mV
$J_{implied}$	implied photocurrent density, $mAcm^{-2}$
J_{SC}	short-circuit current density, $mAcm^{-2}$
$J_{SC,EQE}$	EQE integrated short-circuit current densidy, $mAcm^{-2}$
FF	fill factor, %
R_{sh}	sheet resistance, Ω/□

1

Introduction

1.1. Sustainable energy: an urgent path forward

Concerns over climate change are increasing. There are two notable factors: the continuous increase in global temperatures and the rising intensity of extreme weather events [1]. Human activities are the primary reason for the events. The activities include burning of fossil fuels, deforestation, industrial processes and etc. The concentration of greenhouse gases (GHGs) like carbon dioxide (CO_2), methane (CH_4), and nitrous oxide (N_2O) in the atmosphere is increasing because of the human activities [2]. Climate change will result in rising global temperatures, melting ice caps and glaciers, more frequent and severe weather events, rising sea levels, and disruptions to ecosystems and biodiversity [3]. Figure 1.1 shows the current global surface temperature compared to the temperatures observed from 1951 to 1980. The cooling areas in Figure 1.1 result from complex interactions between ocean currents [4], atmospheric circulation [5], aerosol effects [6], and natural climate variability [7], which can create localized cooling despite the overall trend of global warming.

The transition from transitional fossil fuels to sustainable energy source is urgent. The urgent need also drives the development of technologies that utilize sustainable energy. It is important to reduce GHG emissions to alleviate climate change. Achieving the balance between emitting carbon and absorbing carbon from the atmosphere is ideal solution to control the greenhouse gas in the atmosphere. The balance is named as carbon neutrality or 'net-zero' carbon emissions [10]. The stated goal in the Paris Agreement is to limit global warming to 1.5 °C [11]. Achieving carbon neutrality is essential to realize the goal. There are several strategies that can be adopted to reduce carbon emission. For instance, this can be achieved through improved insulation of buildings, the adoption of energy-efficient appliances, and the electrification of industrial processes [12]. Carbon capture and storage (CCS) technology can help reduce the amount of carbon in the atmosphere. CCS captures and stores CO_2 from industrial processes and power generation. So, it may help to achieve net-zero emissions [13]. Furthermore, sustainable energy is a feasible alternative to replace traditional energy sources [14]. Renewable energy is obtained from

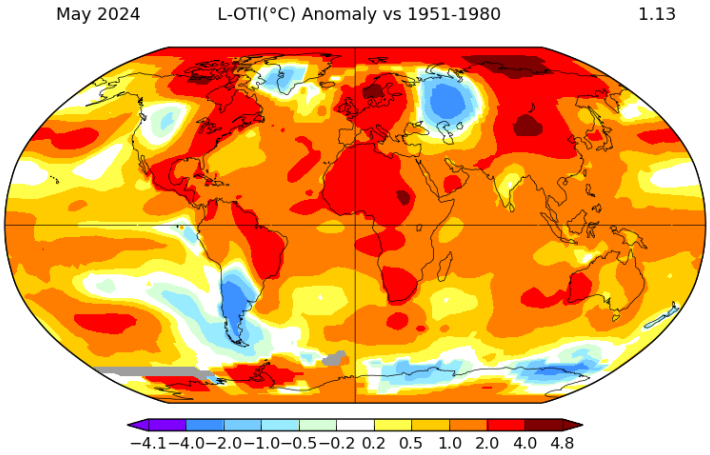

Figure 1.1: Goddard Institute for Space Studies (GISS) surface temperature analysis [8] [9].

nature sources. It can be regarded as unlimited energy compare to human time scale. The renewable energy includes sunlight, wind, rain, tides, waves, and geothermal heat [15]. Unlike fossil fuels, such sustainable energy sources produce little to no greenhouse gases or pollutants. This property makes them necessary for alleviating climate change and reducing environmental impact of mankind activities.

1.2. Photovoltaic cell technology

1.2.1. Innovations in photovoltaic cell technologies

There are various technologies to convert sustainable energy into the forms of energy needed by humans. But Photovoltaic (PV) technology is the dominant technology in the field. This is because it is easy to realize industrial production at low cost level. The most important factor is that solar energy as the supply for PV technology is abundant. The PV effect converts sunlight directly into electricity through solar cells. It was first discovered in 1839 by Alexander Edmond Becquerel [16]. Over the years, the development of photovoltaic technology has made remarkable progress. Early solar cells were relatively inefficient and costly, but huge advances in materials science, manufacturing processes, and cell design have dramatically increased efficiency and reduced costs.

Among various photoabsorbing materials, crystalline silicon (c-Si) has risen as the dominant semiconductor for PV applications. The evolution of c-Si solar cell technology from aluminum back surface field (Al-BSF) to advanced tandem cells with III-V and perovskite materials highlights significant strides in enhancing efficiency and performance. The evaluation of the increasing in the cell efficiency is presented in Figure 1.2.

Initially, Al-BSF cells [18, 19] improved performance with a rear aluminum layer, achieving efficiencies around 20.29% [20]. While the production process of Al-BSF solar cells is simple, their efficiency is limited by insufficient rear-side passivation. This was followed by passivated emitter and rear cell (PERC) technology [21], which introduced passivation layers on the rear surface, boosting conversion efficiencies to 22.61%

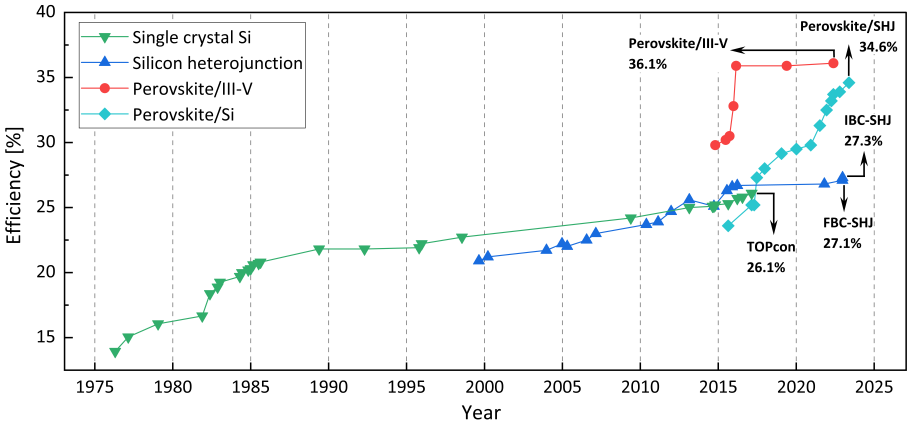

Figure 1.2: Best Research-Cell Efficiency Chart [17].

[22]. The world record efficiency of 24.06% has been achieved by LONGi using a bifacial monocrystalline silicon PERC solar cell [23]. The bifaciality of PERC cell is around 70%. The development of tunnel oxide passivated contact (TOPCon) cells [24], incorporating a thin tunnel oxide layer and doped poly-Si, further improved passivation and efficiencies to 26.89% [25]. Additionally, the bifacial TOPCon cell, with approximately 80% bifaciality, can generate more electricity than a bifacial PERC cell. Subsequently, silicon heterojunction (SHJ) cells [26], using amorphous silicon layers for excellent passivation, reached efficiency up to 27.09% [27]. However, higher manufacturing costs compared to the before mentioned cells limit its mass production. Interdigitated back contact (IBC) cells [28], with all electrical contacts at the rear side, minimized shading losses, achieving up to 27.3% efficiency [29]. The most recent development in solar cell technology is c-Si based tandem solar cells. This technology significantly improves conversion efficiency. The tandem solar cells combine two photoabsorbing materials with different bandgaps to minimize thermalization losses. III-V/silicon tandem exhibit conversion efficiency up to 36.1% [30]. The most widely studied tandem solar cell device contains perovskite top cell and a c-Si bottom cell. The absorption spectrum of perovskite/c-Si tandem device is presented in Figure 1.3.

Perovskite materials are ideal for tandem solar cells due to their high efficiency, tunable bandgaps, excellent opto-electronic properties. Besides, perovskite materials can be produced at low costs, and perovskite film can be deposited on various substrate [32–34]. Perovskite/silicon tandems have achieved around 34.6% efficiency [29], while perovskite/organic tandems have reached above 24% [35]. Each technological development builds upon the previous innovations. The progresses push the improvement of photovoltaic efficiency and the reduction of production-cost.

The market shares of various c-Si PV technologies for 2023 and predictions for future market distribution are presented in Figure 1.4 [36]. In 2023, PERC technology dominates the market. However, its share is projected to decline steadily over time. Conversely, TOPCon and SHJ technologies, which start with moderate shares, are expected to maintain and increase their market presence, respectively. SHJ, in particular, shows a significant

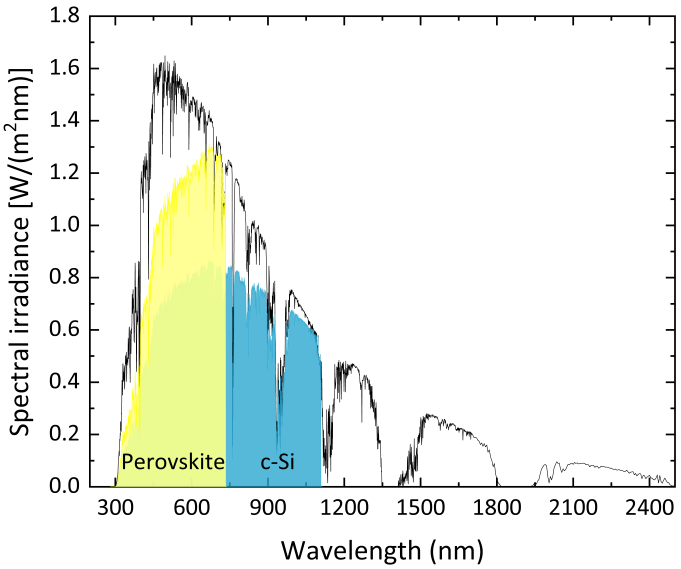

Figure 1.3: The absorption spectrum of a tandem solar cell based on a c-Si absorber (blue) and a perovskite (yellow). The AM 1.5G solar spectrum is the background (black line) [31].

growth trend, becoming one of the dominant technologies by 2034 due to its higher efficiency and better compatibility with perovskite-bottom tandem PV technology. IBC cells maintain a smaller but steady market share throughout the period. Additionally, Si-based tandem cells begin gaining market share around 2028 and continue to rise through 2034.

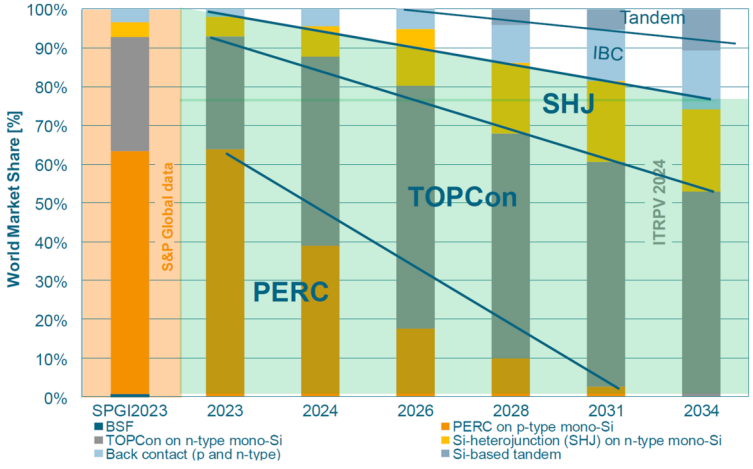

Figure 1.4: World market shares evolution for different cell technologies [36].

Among the abovementioned technologies, SHJ solar cells offer many advantages compared to other silicon solar cells. The advantages make them increase the portion in the PV industry. One of the key benefits is their high efficiency. The world record efficiency of single junction c-Si solar cells which is 27.09% has been achieved by SHJ solar cells [27]. The impressive achievements is due to excellent surface passivation [37] and high open-circuit voltages of SHJ technology [38]. The thin intrinsic and doped hydrogenated amorphous silicon (a-Si:H) layers used in SHJ cells provide excellent passivation, significantly reducing recombination losses. Additionally, SHJ cells can be fabricated at relatively low temperatures (below 200 °C). The low temperature process minimizes thermal stress on the silicon wafers. Beside, SHJ technology allows to use thinner wafers, which can reduce material costs and energy consumption during manufacturing [39–41]. Furthermore, SHJ solar cells are compatible with bifacial structure. The high bifacility factor of SHJ solar cells enable them to generate more power from light incident on both the front and back surfaces [42]. They also exhibit excellent long-term stability. Their resistance to potential-induced degradation and other environmental factors make them sustained high performance over their life [43]. These benefits make SHJ technology as a competitive and promising option for the future of PV.

However, despite these advancements, several challenges still limit the mass production of SHJ solar cells. These challenges include initial high production costs, mostly come from the equipment which require working at vacuum condition. Besides, the high production cost comes from the high consumption of rare materials like silver. The low-temperature silver paste is widely used in SHJ technology for metallization [44]. A lot of efforts has been put on reducing production costs by optimizing cell processing, such as lowering indium and silver consumption and using thinner wafers [44]. Transitioning to copper metallization has been proposed as a solution to reduce costs and improve cell efficiency due to copper's lower cost and better performance, which reduces shading losses and increases the fill factor [45]. Material and processing challenges involve the need for materials such as indium doped transparent conductive (TCO) layers [46]. Developing alternatives like aluminum-doped zinc oxide (AZO) and optimizing deposition techniques can help mitigate these issues [47]. Reducing the thickness of the indium-doped TCO layer is also a solution to decrease the rate of indium consumption in mass production of SHJ solar cells [48–50].

Additionally, the conventional silicon-based doped layers are not optically transparent, especially when applied on the illuminated side of the solar cell. The doped a-Si:H layers induce parasitic absorption due to their bandgap (~1.7eV). Parasitic absorption in the intrinsic layer, doped layer, and TCO films results in a current density loss up to 2.1 mA/cm^2 at the illumination side of solar cells [51]. Additionally, the doping process itself can be complex and costly, introducing complex deposition optimizations [52]. Concurrently, it is a challenge to achieve *p*-type hydrogenated silicon thin-films exhibit high conductivity using plasma enhanced chemical vapour deposition (PECVD). This is because it requires precise control over deposition conditions [53]. The degradation caused by the dopant atoms impacts the long-term stability and performance of solar cells [54]. Furthermore, while hydrogenated nanocrystalline silicon oxide (nc-SiO_x:H) film is essential for achieving high-efficiency SHJ solar cells [55–57], its low deposition rate limits its feasibility for SHJ mass production [58, 59].

1

1.2.2. Dopant-free materials applied in silicon solar cell

A notable advancement within SHJ technology is the use of dopant-free materials that can act as carrier-selective contacts. Energy band alignment in SHJ solar cells is important to ensure that photogenerated charge carriers are efficiently separated and collected. For a successful use of dopant-free material a proper energy band alignment is essential for efficient charge transport. Dopant-free materials align well with the silicon valence and conduction bands, minimizing energy barriers and facilitating carrier extraction. For example, molybdenum trioxide (MoO_3) and divanadium pentaoxide (V_2O_5) create favorable energy band alignments with silicon, enabling efficient hole transport and collection. These materials have low or high work functions (WFs) that selectively allow one type of charge carrier (either electrons or holes) to pass while blocking the other. As an example, MoO_3 has a high WF (~6.9 eV) that effectively selects holes, while blocking electrons, forming an efficient hole-selective contact [60].

Aside MoO_3 and V_2O_5, several transition metal oxide (TMO) layers (e.g. titanium oxide (TiO_2), tungsten trioxide (MoO_3), nickel oxide (NiO_2)) along alkali metal fluoride (AMF) layers (e.g. lithium fluoride (LiF) and magnesium fluoride (MgF_2)) have been used or tested in solar cells. Figure 1.5 illustrates the significant evolution in the conversion efficiencies of c-Si solar cells through the development and optimization of various HTLs and ETLs from 2012 to 2024 [61–103].

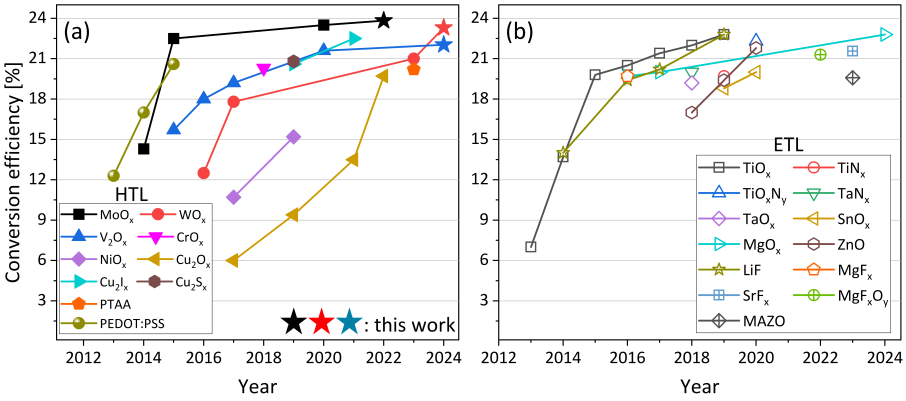

Figure 1.5: Evolution of record efficiencies in c-Si solar cells with various non-Si-based hole transport layers (HTL) on the left and electron transport layers (ETL) on the right. The graphs detail the specific materials used for HTL and ETL. [61–103]

1.3. Motivation

The integration of TMOs into silicon solar cells is driven by many factors aimed at enhancing conversion efficiency. These materials provide compatible benefits in several perspective. They are becoming an option for advancing solar cell technology.

• Improved optical properties. Dopant-free materials often exhibit high transparency, reducing parasitic absorption and enhancing light management within the solar cell [41]. The wide band gap of MoO_3 (~3 eV) ensures high transparency, contributing to higher

short-circuit current densities (J_{SC}) by allowing more light to reach the silicon absorber [104].

• Low-temperature processing. Dopant-free materials can be deposited at low temperatures, making them compatible with the thermal budget of SHJ solar cell fabrication [105]. This reduces energy consumption. The use of thermally evaporated MoO_3 as a hole-selective contact can be processed at temperatures < 200 °C, simplifying fabrication compared to traditional doping methods [106].

• Cost reduction. A significant benefit of using TMOs in silicon solar cells is cost reduction. Many TMOs are abundant on earth. In this case, application of TMOs can reduce the overall manufacturing costs of silicon solar cells. Additionally, TMOs make them attractive for large-scale production [107, 108]. Beside, many deposition technologies are compatible to deposit TMOs films. Especially, thermal evaporation exhibits less complexity. While it involves an additional step, it compensates for the time-consuming nature of depositing the *p*-type layer. Compared to PECVD, thermal evaporation offers a more straightforward and efficient process. These technologies can be easily merged into existing silicon solar cell fabrication processes [109].

• Simplified device architecture. Dopant-free materials allow for simplifying solar cell fabrication process, such as IBC designs [110]. These architectures reduce optical and electrical losses associated with front-side contacts. IBC-SHJ solar cells using MoO_3 and MgF_2 as dopant-free contacts have achieved efficiencies up to 22% [111]. These results indicate the potential of TMOs to simplify fabrication process and achieve high performance solar cells.

• Integration with different solar cell technologies. TMOs are also attractive for their compatibility with different solar cell technologies. They can be integrated into high thermal budget solar cells like PERC and TOPCon and low thermal budget solar cells like SHJ as selective transport layers [112]. TMOs play a crucial role in perovskite tandem solar cells. They serve as the transition interface between different layers to guarantee better band alignment and efficient carrier transport [113, 114].

• Tunable opto-electronic properties. The opto-electronic properties of TMOs can be tailored through modifying the oxygen content in TMOs. The different oxygen content corresponding to different WF of TMOs. This characteristic provide the opportunity to design customized TMO-interfaces and layers that optimize solar cell performance according to specific needs or applications [115, 116]. This tunability expands the application of TMOs to meet various requirements of solar cells.

In conclusion, TMOs enhance light management of solar cells and allow for low-temperature manufacturing. They are abundant, cost-effective, and work well with existing solar cell technologies, making them suitable for a wider range of applications. TMOs can be customized for various applications and improving efficiency of solar cells. Overall, TMOs are important for the future of solar technology because of their abovementioned advantages.

1.4. Outline of this thesis

This chapter provides a general introduction of the climate change and the request for sustainable energy source, development of photovoltaic technologies and the current state of high efficiency silicon heterojunction solar cells. Beside, dopant-free materials

such as TMOs are introduced for application in SHJ solar cells.

Chapter 2 discusses fundamentals of SHJ solar cells including the optical and electrical properties of TMOs, the most widely utilized deposition approaches and their comparison, and the challenges that need to be considered when practically integrating TMOs into solar cells.

Chapter 3 introduces a suitable interface treatment, developed for application of MoO_x in SHJ solar cells, and reports a word record efficiency with 2-nm thick MoO_x as hole transport layer.

Chapter 4 discusses strategies to lower indium consumption by utilizing thinner TCO and realize high efficiency MoO_x-based bifacial SHJ solar cells.

Chapter 5 provides insights on a universal interface engineering method developed for WO_x and V_2O_x to realize high efficiency SHJ solar cells integrated with 2-nm thick WO_x or 3-nm thick V_2O_x.

Chapter 6 summarizes this thesis and gives an outlook for the future research on high performance of SHJ solar cells integrating TMO materials as well as the application of TMO materials in other fields.

1.5. Main contributions to the field

This work contributes to the SHJ solar cells field in the following aspects:

1. Exploring universal interface engineering method for TMO materials applied in SHJ solar cells. We explored different interface engineering methods to alleviate the interface reaction between TMO and (*i*)a-Si:H via plasma treatment performed in the same PECVD chamber after the passivation layer deposition. It is worth to note that the optimized interface engineering method offers a novel approach to control these reactions and optimize TMO deposition conditions. Using the optimized method, we achieved record efficiencies for MoO_x-, WO_x- and V_2O_x- based SHJ solar cells, demonstrating its effectiveness in improving fill factor and conversion efficiency. Additionally, controlling the oxygen content and WF of TMOs through the optimized method ensures sustainable and efficient material use, essential for the scalability and economic viability of SHJ solar cells. The successfully application of optimized method with several TMOs, such as MoO_x, WO_x and V_2O_x indicates its potential applicability to other TMO materials, paving the way for further high-efficiency solar cell innovations. Moreover, the compatibility of the plasma treatment with boron (PTB) method with industrial SHJ production lines ensures these advancements can be adopted in large-scale manufacturing.

2. Unveiling mechanism of the reaction of MoO_x and silicon based films. Through electrical simulations and a series of characterizations of the MoO_x/(*i*)a-Si:H interface, we investigated the interface reaction and the impact on the electronic properties of SHJ devices. We found that a SiO_x thin film is found as a result of the interface reaction setting up a dipole layer, which is the primary contributors to the degradation of electronic properties of the device. Our research elucidates the underlying reaction mechanisms and proposes potential strategies to mitigate this degradation.

3. Reducing the use of indium-based TCO in bifacial copper-plated SHJ devices. Through the innovative use of MoO_x as a hole transport layer and the optimization of *n*-contact layers, the study achieved conversion efficiencies of over 23% while reducing IWO layer thickness by more than 67% (from total 225 nm to total 100 nm). This reduc-

tion addresses the critical issue of indium scarcity, making large-scale production more sustainable and cost-effective.

4. Demonstrating high bifaciality of MoO_x based bifacial SHJ solar cells. By integrating MoO_x as a hole transport layer and optimizing Si-based *n*-contact layer in bifacial SHJ solar cells, we maximize the bifaciality factor, highlighting the potential for these cells to achieve higher energy yields under real outdoor conditions, leading to more efficient and ecofriendlier solar energy solutions.

2

TMO in c-Si solar cells: mechanisms and challenges

2.1. Working principle of TMO materials in SHJ solar cells

As mentioned in the previous chapter, there are several kinds of dopant-free materials. In this work, we focus on TMOs as the dopant-free materials applied in SHJ solar cells. TMOs can realize selective carrier transport based on different WFs [109, 117].

ETL materials normally have low WFs [52, 118–120], as indicated by the red dashed line in Figure 2.1. Band diagram of c-Si/TMOs interfaces are presented in Figure 2.2. Additionally, ETL materials exhibit a low conduction band offset with c-Si (E_C = 4.1 eV [121]), while the valence band offset is relatively higher, as presented in Figure 2.2a. With this property, electrons can be transported from the conduction band of c-Si to the ETL materials while holes are blocked, thereby selective carrier selectivity [122].

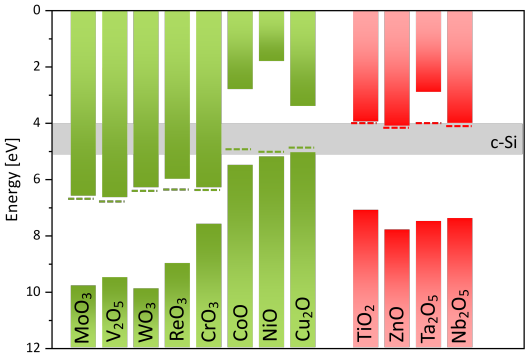

Figure 2.1: The approximate band alignment between c-Si and TMO materials is illustrated. HTLs are labelled in green, while ETLs are labelled in red. The WF positions are indicated by green dashed lines for HTLs and red dashed lines for ETLs, respectively. For reference, the band edges of c-Si are represented by a gray bar [61, 64, 75, 76, 86, 96, 123–125, 125–139].

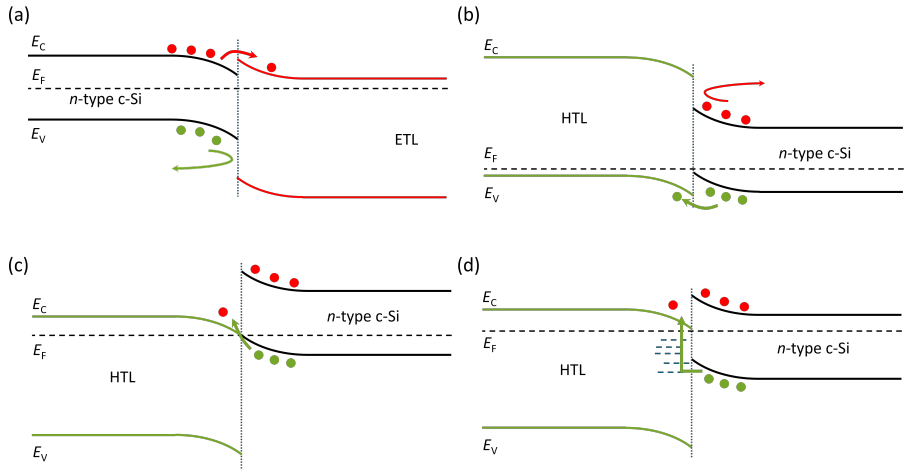

Figure 2.2: Band diagram of different c-Si/TMOs interfaces: (a) *n*-c-Si/low WF TMO (ETL), (b) *n*-c-Si/ high WF (*p*-type) TMO (HTL), (c) *n*-c-Si/high WF (*n*-type) TMO (HTL), (d) as (c) but with realistic gap states at the interfaces. This allow in (d) indicates as selective contact layer. The red and green arrows indicate the movement direction of electrons and holes, respectively. The dashed line indicates the Fermi level.

On the other hand, HTL materials with relatively higher WFs than ETL materials are classified into two categories: *n*-type and *p*-type materials [140]. *p*-type materials, such as CoO, NiO, and Cu_2O, as shown in Figure 2.1, have a large conduction band offset and a lower valence band offset compared to c-Si. Thus, *p*-type HTL materials align with bands of c-Si, enabling selective hole transport from the valence band of c-Si to the valence band of HTL materials [141]. The transport mechanism is shown in Figure 2.2b. Conversely, *n*-type HTL materials, including MoO_x [106], V_2O_x [142], WO_x [143], ReO_3 [130], and CrO_3, possess high WFs (> 5.2 eV). The high WF of these materials induces band bending in c-Si [144], accumulating holes at the TMO/c-Si interface, as depicted in Figure 2.2c. The conduction band of these TMOs is close to the valence band of c-Si, ensuring recombination of electron and holes at the interface to generate electricity [145].

Typically, TMO materials tend to react with the substrate [109], such as c-Si, creating gap states at the interface. Figure 2.2d shows that these gap states facilitate carrier transport at the interface [146]. Consequently, trap-assisted tunneling (TAT) is utilized for carrier transport in this context [147].

2.2. TMO materials choice for devices

2.2.1. Original passivation of TMO materials in silicon solar cell

The passivation of silicon surfaces plays an important role in the efficiency of solar cells, as it minimizes recombination losses and improves charge carrier transport. TMOs have been investigated as they can provide effective passivation effects and selective carrier transport properties [148]. This chapter explores the original passivation effects of TMOs.

TMOs provide both chemical and field-effect passivation [140]. Chemical passivation occurs when TMOs interact with the silicon surface, reducing the density of dangling bonds that act as recombination centers. This results in enhanced minority carrier

lifetimes which is critical to achieve high open-circuit voltages. On the other hand, field-effect passivation generates from the large WF differences between TMO and Si substrate. These differences generate strong electric fields at the silicon interface and results in selective transport of electrons or holes while blocking the opposite charge carrier.

Different TMOs exhibit unique properties that make them suitable for specific functions within a solar cell. For instance, MoO*x* is widely recognized for its high WF, making it an excellent hole-selective contact [69]. V_2O_x, another prominent TMO, balances chemical and field-effect passivation effectively, contributing to superior carrier dynamics in silicon heterojunctions [69]. Similarly, TiO_x, with wide bandgaps and high electron mobility, is ideal for electron-selective contacts.

2.2.2. Electron transport materials

TiO_x ($2.9 < x < 3$) has been studied as the most promising dopant-free ETL [149–151]. The moderate conduction band offset between TiO_x and c-Si supports the selective transport of electrons. The large valence band offset between TiO_x and c-Si blocks holes from moving towards c-Si/TiO_x interface [152]. Figure 1.4 presents the notable conversion efficiency achieved by silicon solar cells endowed with TiO_x as ETL materials. Moreover, other TiO_x-based compound act as ETL also showing favorable electronic properties. Promising result has been realized with TiO_xN_y based solar cells. It improves the conversion efficiency by reducing the interface recombination [153]. Other TMOs, including ZnO [90], Ta_2O_5 [62], and Nb_2O_5 [154], listed in Figure 2.1, have also been investigated as ETLs. These materials also have suitable band alignment with c-Si.

2.2.3. Hole transport materials

More options for HTL materials are available compared to the ETL materials listed in Figure 2.1. These HTL materials can be categorized into *n*-type and *p*-type materials. As mentioned in Section 2.1, *p*-type HTLs are potential candidates due to their small valence band offset with c-Si. Currently, only CoO [131], NiO_x [155], and Cu_2O_x [156] exhibit promising potential in this scenario. However, the performance of working devices is still limited by insufficient surface passivation at the TMO/c-Si interface [157].

For *n*-type TMO materials, promising choices include MoO_x [158], WO_x [159], and V_2O_x [160]. They are also the focus of this thesis. Currently, the record conversion efficiency of SHJ solar cells featuring a dopant-free HTL, specifically a MoO_x hole collector, is 23.83% [102]. This will be presented in Chapter 3. While the reported conversion efficiencies regarding other HTL materials are still not satisfied [161].

2.2.4. Interaction of TMO and Si substrate

The most prominent issue limiting the conversion efficiency is the interface reaction between TMO materials and the substrate [162]. The reaction can be simplified and express as follow:

$$TO_a + Si = TO_{a-b} + SiO_b \tag{2.1}$$

where T stands for transition metal, TO_a stands for stoichiometry TMO, $TO_{a\text{-}b}$ stands for the non-stoichiometry oxide formed after the reaction, SiO_b stands for the silicon

and oxide compound formed because of the reaction. This issue is due to the inherent thermodynamic sensitivity of TMO materials [163]. After contacting with c-Si, TMOs would react with c-Si at the interface. The reaction results in the formation of a thin SiO_x layer at the interface and introducing gap states in TMOs as well [164]. The formation of the SiO_x film at the interface is shown in Figure 2.3. When (*i*)a-Si:H is applied as the passivation layer in SHJ solar cells, the TMO layer comes into contact with the (*i*)a-Si:H layer, leading to a reaction at the TMO/(*i*)a-Si:H interface [140]. Furthermore, the oxygen vacancies created by the interface reaction reduce the average cation oxidation state of the transition metal elements [165], decreasing the WF of TMO materials and hindering carrier extraction from the c-Si absorber [166].

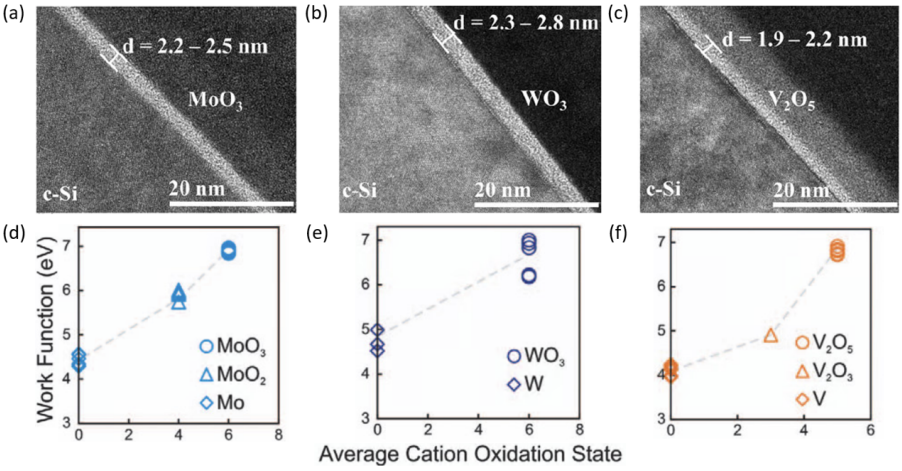

Figure 2.3: HR-TEM images of the TMO/*n*-Si heterostructures showing SiO_x interlayer between *n*-Si and (a) MoO_x, (b) WO_x and (c) V_2O_x [140]. Plots of WF versus nominal average oxidation state of metal atoms in (d) MoO_x, (e) WO_x and (f) V_2O_x [162]. Images from [140, 162]

Prior TMO deposition, there are three solutions to address this issue. First, growing a SiO_x layer is a promising solution to alleviate the interface reaction. A pre-grown high-quality SiO_x layer significantly enhances the performance and thermal stability of MoO_x-passivated contacts in Si solar cells by improving surface passivation, reducing interfacial defects, and maintaining stoichiometry during thermal treatments. However, this improvement results in an increase in contact resistivity, indicating the need for further optimization [167]. Li *et al.* report that inserting an ultra-thin SiO_x tunneling layer between V_2O_x and the c-Si surface by suppressing recombination, enhancing the open-circuit voltage and fill factor, resulting in a power conversion efficiency (PCE) of 21.60% [168].

Another alternative solution is to employ a multilayer of TMO materials as HTL. This multilayer structure improves electrical and optical properties, enhances carrier transport, and reduces recombination losses [169, 170]. The $V_2O_x/SiO_x/NiO_x$ contact structure greatly enhances the efficiency and performance of c-Si solar cells by improving hole selectivity, reducing contact resistivity, and maintaining high surface passivation quality. The incorporation of an ultra-thin SiO_x interlayer is key to these enhancements, leading

to a record PCE of 22.03% for V_2O_x-based selective contacts [67]. CrO_x is an effective hole-selective contact material for *p*-type Si solar cells. It offers low contact resistivity and improvement in conversion efficiency. The CrO_x/Ag/CrO_x multilayer structure is an effective solution as well. The device integrated the structure has achieved a power conversion efficiency of 20.3% with excellent stability and passivation quality [75].

Last but not least, prior to TMO deposition, (*i*)a-Si:H is deposited to provide surface passivation in SHJ solar cells. However, the reaction between TMO and (*i*)a-Si:H will harm the passivation quality. Besides, the H inside (*i*)a-Si:H will cause the O defects in TMO materials. Annealing the cell precursors improved the cell efficiency to 23.5% [66].

2.3. The opto-electrical properties of TMOs

TMOs are attractive to SHJ solar cells due to their unique optical and electronic properties. MoO_x is particularly notable for its high WF (> 6 eV) and wide bandgap (~ 3 eV). The wide bandgap contributes to high transparency and low absorption coefficient [171–173]. These properties make MoO_x an excellent hole extraction layer to replace traditional *p*-type hydrogenated silicon based layers. The electronic structure of MoO_3 is presented in Figure 2.4a. It illustrates the local coordination environment around a molybdenum center in MoO_3 [174]. The molybdenum atom is surrounded by three nonequivalent types of oxygen atoms which labeled O(1), O(2), and O(3). The oxygen atoms occupy distinct crystallographic positions and exhibit different bonding geometries. These unique oxygen positions give rise to the characteristic wide bandgap and influence the material's opto-electronic properties in applications [175]. MoO_3, WO_3 and V_2O_5 which are the main focus of this work share similar key features in electronic structure and opto-electronic properties [176, 177].

The extinction coefficient of several TMO materials is presented in Figure 2.4b. In this plot, the extinction coefficients (*k*) of various TMO thin films are shown as a function of wavelength from the ultraviolet (UV) to the near-infrared (NIR). The transparent *n*-type and *p*-type nc-SiO_x are included as well as references. Overall, large *k* values in the UV region (around 300 – 400 nm) illustrate strong absorption near the onset of each material's bandgap, while orders-of-magnitude decrease in *k* reveals significant transparency extending into the visible and NIR regimes. Notably, Nb_2O_5, Ta_2O_5 and TiO_2 exhibit particularly low *k* beyond 400 nm, demonstrating their ability as transparent electrodes and antireflection layers. ZnO and WO_3 also exhibit moderate absorption and drop at longer wavelengths. Meanwhile, the (*n*) and (*p*) SiO_x:H curves generally underscore higher absorption than TMO films. Comparing to transitional doped nc-SiO_x, these TMO materials are transparent at wavelengths above 500 nm, indicating their excellent transparency in the visible light range.

Another promising TMO is vanadium oxide (V_2O_x), which can also serve as a hole-selective contact due to its high WF [80, 92, 133]. The performance of V_2O_x, along with other TMOs like WO_3 and ReO_3, is primarily influenced by the presence of oxygen vacancies and the resulting electronic structure. These vacancies can modulate the electronic properties, improving the hole conductivity and carrier selectivity, which are crucial for the efficiency of SHJ solar cells [69]. Additionally, the ability to deposit these TMOs at low temperatures further reduced costs. The combined effect of high WF, wide bandgap, and low-temperature processing makes TMOs as a potential candidate in high-efficiency SHJ

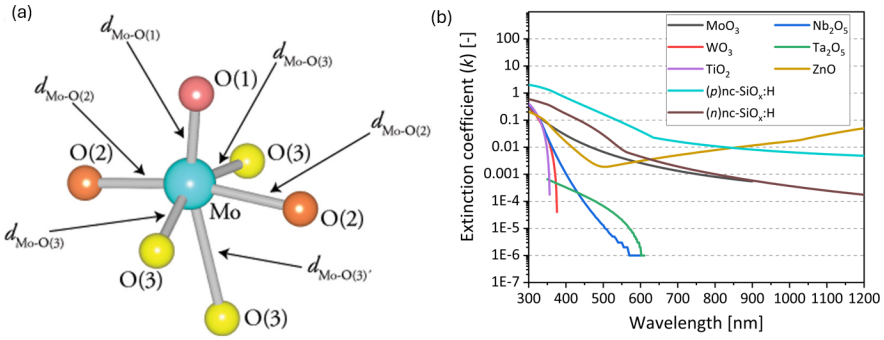

Figure 2.4: (a) The electronic structure of MoO_3 molecule [174]. (b) The extinction coefficient of TMO materials [178–183].

solar cells [184].

The application of TMOs in silicon solar cell are influenced by many factors during deposition and post-processing. For instance, the deposition angle influences TMO properties [173]. The TMO films exhibit increased surface roughness at the condition of tilted deposition angles of substrate. The changes in surface morphology affect the TMO's optical and electronic properties [173, 185]. Additionally, the substrate temperature plays an important role in determining the stoichiometry of TMO materials and affects the passivation quality at the Si/TMO interface [186]. Furthermore, the deposition rate and pressure affect their stoichiometry and properties as well. TMOs change to substoichiometry because of variations in deposition conditions. The sub-stoichiometry state is attributed to the oxygen vacancies in TMOs [69, 112, 187–189]. Besides, the stoichiometry and WF of TMOs are significantly influenced by film-thickness. Thinner films may exhibit more defects and a lower WF, whereas thicker films can achieve a higher WF but also have increased resistivity [66, 93, 102, 190, 191].

Moreover, TMOs are highly sensitive to post-treatments. Annealing as commonly used as post-treatment to influence the properties of TMOs [192–198]. The ambient environment is another essential condition to be considered. Interactions with humidity and atmospheric gases from environment can further degrade electronic property of TMOs over time. The ambient temperature may accelerate these changes [194]. In addition, TMOs tend to react with substrate materials such as silicon thin films during or after deposition. This reaction can lead to the formation of silicon oxide, which may impact the electronic properties of the TMO layer [142, 199]. So, inserting a buffer layer is crucial to mitigate interface reactions and support the formation of more stoichiometric TMOs. [167, 200]. Understanding and controlling these factors is crucial for optimizing the performance of TMOs applied in SHJ solar cells.

TMOs are a great opportunity to enhance the performance of SHJ solar cells due to their high WFs, wide bandgaps, and transparency in the visible light range. These properties make TMOs as carrier-selective contacts and enable low-temperature deposition, reducing fabrication costs. However, their application is limited by factors such as sensitivity to processing and environmental conditions, which can affect their electronic

properties. Understanding and controlling these factors are essential for optimizing TMOs' performance and reliability in SHJ solar cells.

2.4. TMO deposition technology

Various deposition methods are compatible with TMO materials which can be applied in SHJ solar cell fabrication process, including vacuum-based techniques like physical vapor deposition (PVD) and chemical vapor deposition (CVD), as well as atomic layer deposition (ALD), solution processing, and more recent development such as hot wire oxidation–sublimation deposition (HWOSD). Each offers distinct benefits regarding film quality, process scalability, process speed, and cost.

PVD includes thermal evaporation and sputtering. It can provide uniform films with strong adhesion, and high deposition rate. Most of the TMO films can be deposited with PVD method [199]. This method enables the fabrication of MoO_x layers, which act as HTL with high transmittance and low absorption [102][66]. Nevertheless, the requirement for high vacuum levels substantially increases capital and operational expenses, and upscaling to large-area substrates can be challenging.

CVD is another applicable method to deposit TMO thin films with gas-phase precursors [201]. CVD is recognized for its highly conformal coatings, making it particularly appealing for flat and textured silicon surfaces in SHJ devices. Plasma enhanced CVD allows the growth of high-quality TMO thin films directly onto silicon substrates at low temperatures [202]. However, CVD can be limited by the toxicity and instability of TMO precursors, in addition to the cost and complexity of the reactor systems required.

Similarly, ALD is another effective method used for depositing. This method is attractive for its excellent conformal and uniform thickness, even on complex or textured substrates [203]. ALD deposited V_2O_x films can provide excellent surface passivation and low contact resistance in SHJ solar cells [98, 204]. However, the disadvantages of ALD comes from its low growth rate and high precursor costs, which makes it less favorable for large-area and high-volume manufacturing.

By contrast, solution-based processing like spin coating is outstanding by low investment and simple instrumentation [205]. It offers a low-cost method for depositing TMO films [206, 207]. Besides its scalability for large-area deposition, solution processing often struggles with film uniformity and may required post-deposition thermal treatments to improve crystallinity and conductivity [208]. Moreover, issues like film defects, cracking, and pinholes can arise during solvent evaporation and annealing.

Innovative approaches such as HWOSD are also employed for the deposition of TMOs in SHJ solar cells [88]. The HWOSD technique has been developed to prepare MoO_x thin films, achieving a power conversion efficiency of 21.10% in SHJ solar cells with a 14-nm thick MoO_x layer as HTL [209]. HWOSD requires lower vacuum demands. Yet it remains limited by material versatility, stoichiometry control, and scalability.

In summary, the choice of TMO deposition method exerts a profound influence on the performance of SHJ solar cells. Vacuum-based methods like PVD, CVD, and ALD tend to yield higher-quality, more uniform layers with well-controlled properties at the expense of higher costs and more stringent processing conditions. Alternatively, spin-coating offer a lower-cost route yet may require careful engineering to match the performance of high-vacuum processes.

2.5. Architecture of SHJ solar cells with dopant-free HTLs

SHJ solar cell as one of the latest technology exhibit great advancements. It has achieved high efficiencies through the use of passivating contacts [40]. The front junction and rear junction are two different configurations. These two designs both present unique benefits and challenges that influence their performance and industrial applicability [37].

Front junction (FJ) SHJ solar cells position the minority charge carrier collecting contact at the front of the solar cell absorber [210]. The sketch of FJ-SHJ solar cell is presented in Figure 2.5a. This configuration has proven effective in simplifying the manufacturing process and lowering initial costs. One of the primary challenges of this design is the high parasitic absorption in the front contact layers, especially in case of (*p*)a-Si:H due to its high absorption coefficient in the visible spectrum [211]. Despite these challenges, FJ-SHJ solar cells can achieve high efficiencies when high-quality wafers and excellent surface passivation are utilized.

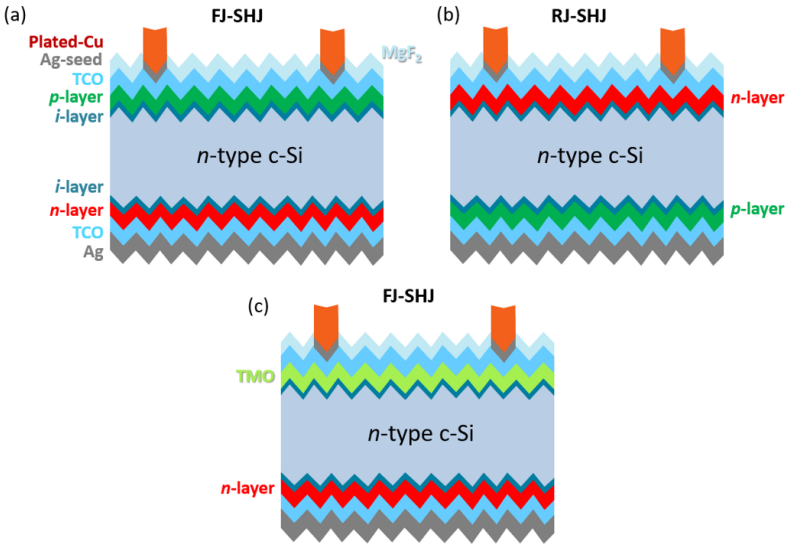

Figure 2.5: The typical architectures of SHJ solar cells: (a) front junction SHJ; (b) rear junction SHJ; (c) front junction SHJ exhibiting TMO as HTL.

Rear junction (RJ) SHJ solar cells, on the other hand, place the minority charge carrier collecting contact at the rear of the solar cell [212]. This allows for the use of less conductive but more transparent TCOs at the front side, reducing the need for high transparency in the rear contact materials [213]. Consequently, rear emitter configurations can use different materials for the rear contact, which can be thicker or more highly doped, potentially improving contact formation and band alignment without affecting the optical response of the device [214]. In case of monofacial devices, RJ is the go-to architecture to ensure excellent hole collection. Additionally, Si-based *n*-type layers can easily balance the trade off between optical and electronic properties. Currently, the RJ structure is mainstream in industrial production. In conclusion, both front emitter and rear emitter SHJ solar cells offer distinct advantages and face unique challenges.

Dopant-free TMOs as the potential carrier selective contacts have been integrated in SHJ solar cells and achieved promising results [92, 102, 215]. To fully exploit the optical advantages of TMO materials, the HTL-TMO material is applied at the front side of the device, resulting in FJ-SHJ structure [66, 123, 216]. The architecture of SHJ solar cells integrated TMO as HTL is presented in Figure 2.5c. The use of HTL-TMOs in SHJ solar cells has several advantages. These materials avoid the doping process, thereby simplified the manufacturing process and reducing the risks of performance degradation associated with doped layers [217, 218]. High WF TMOs like MoO_x and WO_x facilitate efficient hole collection and significantly lower recombination losses [219]. Moreover, their high transparency (see Figure 2.4) ensures minimal parasitic absorption losses [100]. This property is particularly beneficial for front junction configurations where light management is crucial. The band diagram of the SHJ solar cell integrated TMO as hole collector (see Figure 2.5c) is presented in Figure 2.6. This diagram illustrates the energy band alignment across the different layers of the solar cell. The valence bands and conduction bands of each layer are highlighted in black and pink, respectively. The Fermi level (E_F) is represented by the dotted line. TMO exhibits high WF which facilitates efficient hole extraction while blocking electron flow. The band bending at the interfaces between different layers indicates built-in electric fields which are essential for driving charge carriers towards their respective electrodes.

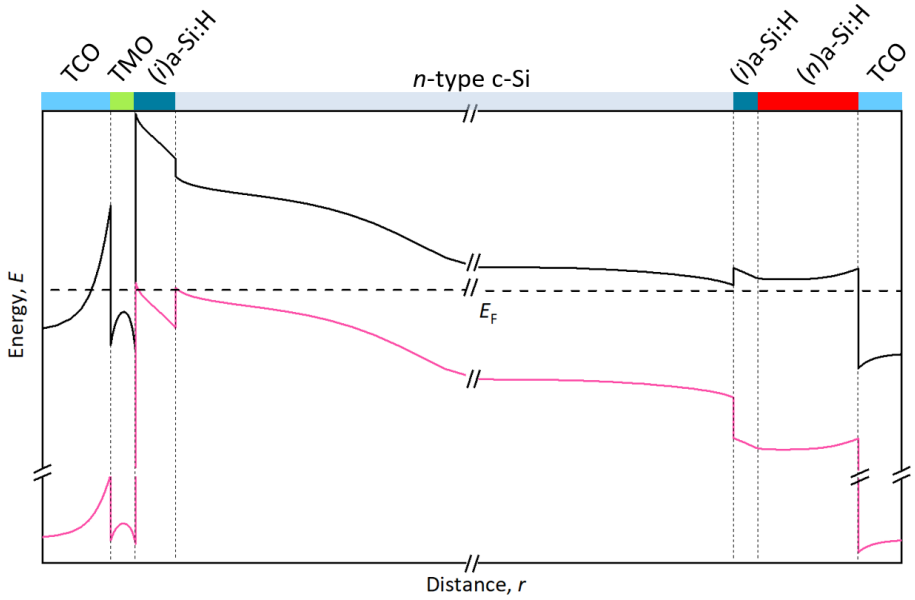

Figure 2.6: The band diagram of the front side of SHJ solar cells integrated TMO as HTL. The band diagram was numerically generated using Sentaurus by Dr. Paul Procel.

2.6. Conclusion

This chapter gives an overview of the working principles and advantages of TMOs in SHJ solar cells. TMOs serve as dopant-free selective contact layers due to their high or low WFs relative to *n*-type c-Si bulk, enabling efficient selective transport of charge carriers. High WF TMOs act as hole transport layers (HTLs) could selectively transport holes and block electrons. On the contrary, low WF TMOs serve as electron transport layers (ETLs) could selectively transport electrons and block holes.

TMO materials, like MoO_x, V_2O_x, WO_x, TiO_x, ZnO, and Ta_2O_x have been explored for their well band alignment with c-Si. TMOs provide passivation effect by reducing surface recombination through chemical interactions and field-effect mechanisms. Besides, these materials help selective carrier extraction, which is important for high-efficiency solar cells. For instance, MoO_x and V_2O_x have shown promising results as HTLs due to their high WFs and wide bandgaps. These materials improve carrier selectivity and reduce parasitic losses in the device.

The opto-electrical properties of TMOs are outstanding. Their high transmittance and ability to facilitate efficient hole transport while reducing recombination losses in combination with excellent surface passivation enabled by (*i*)a-Si:H are crucial for high-efficiency solar cells.

Various deposition technologies are compatible with TMOs, such as thermal evaporation, ALD, PECVD, sputtering, and spin coating. Each method can be incorporated into existed mass production line. In order to fully exploit the optical potential of TMO materials, the typical architecture of SHJ solar cells endowed with TMO-HTL is a FJ architecture.

In conclusion, TMOs are applicable in SHJ solar cells due to their excellent opto-electronic properties. They can improve efficiency by reducing parasitic absorption and improving hole transport. These materials are promising candidate for the development of high-performance solar cells.

3

23.83% efficiency SHJ solar cells with ultra-thin MoO_x layer

This chapter was published in *Progress in Photovoltaics: Research and Applications* * [102]

Abstract

Thin films of transition metal oxides such as MoO_x are attractive for application in silicon heterojunction solar cells for their potential to yield large short-circuit current density. However, full control of electrical properties of thin MoO_x layers must be mastered to obtain an efficient hole collector. Here we show that the key to control the MoO_x layer quality is the interface between the MoO_x and the hydrogenated intrinsic amorphous silicon passivation layer underneath. By means of ab-initio modeling, we demonstrate a dipole at such interface and study its minimization in terms of work function variation to enable high performance hole transport. We apply this knowledge to experimentally tailor the oxygen content in MoO_x by plasma treatments (PTs). PTs act as a barrier to oxygen diffusion/reaction and result in optimal electrical properties of the MoO_x hole collector. With this approach we can thin down the MoO_x thickness to 1.7 nm and demonstrate short-circuit current density well above 40 mA/cm^2 and a champion device exhibiting 23.83% conversion efficiency.

*Cao, L., Procel, P., Alcañiz, A., Yan, J., Tichelaar, F., Özkol, E., Zhao, Y., Can, H., Yang, G., Yao, Z., Zeman, M., Santbergen, R., Mazzarella, L. and Isabella, O. (2023). Achieving 23.83% conversion efficiency in silicon heterojunction solar cell with ultra-thin MoO_x hole collector layer via tailoring (*i*)a-Si:H/MoO_x interface. Progress in Photovoltaics: research and applications, 31(12), 1245-1254. https://doi.org/10.1002/pip.3638

**Cao, L., Procel, P. contribute equally to this work.

3.1. Introduction

Silicon based solar cells dominate the market of photovoltaics, which hold the highest potential for green electricity production [42, 220]. A front/back-contacted architecture combined with silicon heterojunction (SHJ) concept realized a world record efficiency of 27.09% [29]. However, conventional silicon-based doped layers, which work as carrier-selective transport layers, are not ideally transparent [51]. Furthermore, misalignment of the band structure at doped a-Si:H/c-Si interface and doped a-Si:H/transparent conductive oxide (TCO) interface translates into fill factor losses [221, 222].

Transition metal oxide (TMO) materials have been investigated to circumvent this fundamental limitation [63, 64, 75, 94, 96, 215]. The interest in TMO thin films stems mainly from their wide-range tunable work function (WF), electronic properties, and good transparency, all of which are important for application in SHJ solar cells [105, 223]. Molybdenum oxide (MoO_x) as one of the most promising hole transport layers (HTL) has been well examined [61, 68, 104, 224, 225]. In this respect, different processing methods have been investigated to exploit the potential of MoO_x layers. For instance, MoO_x films have been produced by a solution process using organic precursors followed by thermal treatment [226], atomic layer deposition [189, 227, 228] and thermal evaporation [189, 229]. Furthermore, SHJ solar cells using MoO_x have achieved above 22% efficiency [16], [19] and, so far, a record performance of 23.5% with the potential for further improvements [66].

However, several issues occurring at a-Si:H/MoO_x interface have been reported [230, 231]. Most prominently, the formation of a thin SiO_x layer during the deposition of MoO_x has been shown in [66, 68, 224, 232]. Some research reported that the electronic properties of MoO_x are regulated by its oxygen content [120, 164, 233] and by the interfacial condition with its growth substrate. Controlling these aspects is thus crucial for the effective application of MoO_x in high-efficiency solar cells. In particular, several works attempted to limit the reaction between the MoO_x and the intrinsic hydrogenated amorphous silicon, (*i*)a-Si:H, underneath by annealing [66] and by pre-growth of a SiO_x layer [167, 234]. Specifically, a surface treatment on the (*i*)a-Si:H layer before MoO_x deposition improves solar cell performance [225]. Nevertheless, the fundamental knowledge of the phenomena occurring at the (*i*)a-Si:H/MoO_x interface and its application for achieving efficient solar cells devices is not well understood yet.

This work presents a complete study of SHJ solar cells based on MoO_x hole collector from fundamental theory up to device-level integration. We first present a theoretical framework of MoO_x properties depending on silicon-based substrates (i.e. (*i*)a-Si:H). Accordingly, we investigate an industry-appealing plasma treatment method to control the growth of high quality MoO_x thin films by achieving an optimal oxygen content. Then, we evaluate the transport properties of the whole hole contact stack by measuring its contact resistivity. Finally, we showcase high efficiency heterojunction solar cells with ultra-thin MoO_x films, achieving short-circuit current density equal to 40.2 mA/cm^2 and, in the same device, a champion conversion efficiency of 23.83%.

3.2. Methodology

3.2.1. Experimental

Figure 3.1 shows the flow chart for the manufacturing of MoO_x based SHJ solar cell. The samples were prepared using 4-inch double-side polished *n*-type FZ wafers with <100> orientation. The resistivity and thickness of the wafers are 3 ± 2 cm and 280 ± 20 µm, respectively. Wafer texturing process was conducted in a TMAH solution with ALKA-TEX as an additive [235]. Next, the wafers were cleaned using wet-chemical cleaning and dipping them in 0.55% hydrogen fluoride (HF) for 5 min [235]. Afterwards, the wafers were loaded into a multi-chamber PECVD equipment for thin-film silicon layers deposition. Rear side layers consist of (*i*)/(*n*)a-Si:H layers stack deposited according to ref [236] [237] [238] and same deposition conditions were used for all the samples within this work. Subsequently, (*i*)a-Si:H layer was deposited on the front side of the samples. In order to control the growth of high quality MoO_x thin films by achieving an optimal oxygen content, different (*i*)a-Si:H/MoO_x interface treatments were employed to investigate their effect on MoO_x properties. Accordingly, two different conditions were adopted after depositing (*i*)a-Si:H: using a highly hydrogen diluted (~170 sccm) gas mixture of (1) SiH_4, H_2, and CO_2 namely PT (Plasma Treatment) or (2) SiH_4, H_2, CO_2 and B_2H_6 namely PTB (Plasma Treatment with Boron radicals). The inclusion of boron is optimal for deposition MoO_x as successfully demonstrated in our previous work [225]. As it will be shown in Section 3.3.3, these plasma treatments introduce two layers on top of porous (*i*)a-Si:H consisting of a-SiO_x:H/a-Si:H. PT and PTB processes used the same pressure (2.2 mbar) but different power density (76 and 90 mW/cm^2, respectively). Note that we also fabricated a sample without plasma treatment (i.e. noPT). Then, MoO_x layers were thermally evaporated at a base pressure of 5×10^{-6} mbar from a stoichiometric MoO_3 powder source at a deposition rate of about 0.1 nm/s. We used a reference front-junction SHJ sample for comparison purposes featuring 21-nm thick *p*-layer as reported elsewhere [58]. After that, optimized 50-nm and 150-nm thick tungsten-doped indium oxide (IWO) layers were sputtered through a hard mask at front and rear side, respectively, defining six 2×2 cm^2 solar cells per wafer [239]. The front metal electrode consists of electroplated Cu fingers at room temperature on top of 200-nm thick thermally evaporated Ag seed layer [240] [241]. The rear metal electrode was formed by 500-nm thick thermally evaporated Ag. Finally, 100-nm thick MgF_2 was e-beam evaporated on the front side as an additional antireflection coating layer. All abovementioned layer thickness were calculated from the nominal thickness applying the geometrical factor of 1.7 for a textured surface [242].

Effective minority carrier lifetimes were measured at different steps of the fabrication by Sinton-120 equipment. Current-voltage characteristics of solar cells were determined using an AAA-rated Wacom WXS-90S-L2 solar simulator under standard test conditions. In-house external quantum efficiency (EQE) equipment, operated with photodiode calibrated at Fraunhofer ISE, was employed to obtain the $J_{SC,EQE}$. Measuring the spectral response was performed on a dedicated cell w/o metal grid. Compositional investigation of MoO_x layers was carried out with a ThermoFisher K-Alpha X-ray photoelectron spectrometer (XPS) [243] [244]. The XPS uses an Al Kα X-ray source with an energy of 1486.68 eV. The base pressure of the processing chamber is 2×10^{-9} mbar. The measurement was carried out at room temperature after the high vacuum was obtained. Note that samples for XPS analysis were prepared using 280 ± 20 um flat <111> *n*-type float-zone (FZ)

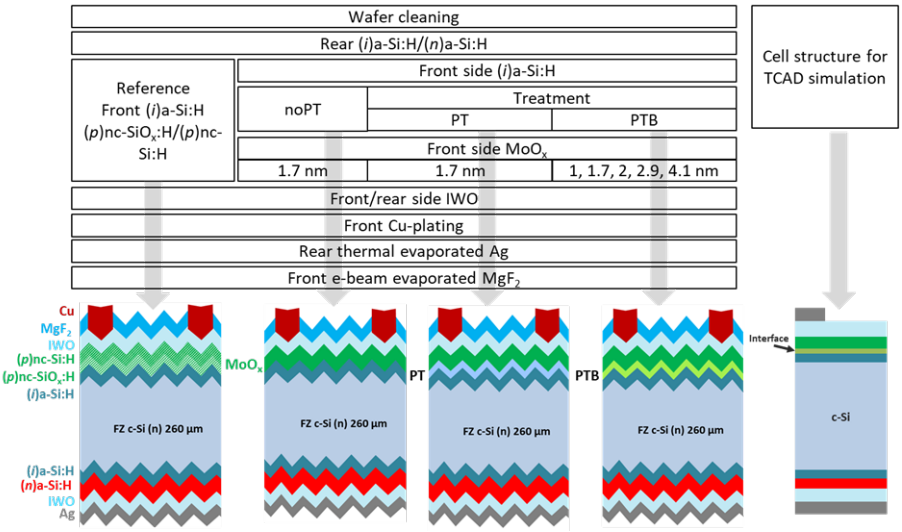

Figure 3.1: Flow chart of solar cells fabrication and cross-sectional sketches of the studied devices.

wafers with the identical processes as reported in Figure 3.1 to mimic the same surface orientation available at the pyramid facets in solar cells and adapting the deposition time to achieve the same thicknesses as in textured samples. High-resolution transmission electron microscope (HR-TEM) combined with energy dispersive X-Ray spectroscopy (EDX) was employed to evaluate the structure and composition of the contact stack on lamellas taken from solar cells with higher performance (i.e. cells endowed with 1.7-nm thick MoO_x layers). Finally, contact resistivity (ρ_c) of the contact stack was measured in samples using double textured *p*-type <100> FZ wafers (260 ± 20 μm thick after texturing) [58]. The schematic structure of these stacks of layers can be found in Figure A.1.

3.2.2. Simulations

We investigated the atomistic phenomena at the Si/MoO_x interface by means of first-principle density functional theory (DFT) calculations via Vienna *Ab* initio Simulation Package (VASP). We analyzed the thermodynamically stable orthorhombic α-phase of molybdenum trioxide. α-MoO_3 crystallizes with four formula units of MoO_3 in an orthorhombic cell with symmetry Pbnm [245]. This makes the unit cell to be composed of 4 Mo atoms and 12 O atoms, with lattice constants a = 3.96 Å, b = 13.85 Å and c = 3.70 Å. The structure of molybdenum oxide is based on bilayers oriented perpendicular to the y axis fastened across that axis by weak van der Waals forces. Each bilayer consists of two sublayers of distorted MoO_6 octahedra that form edge-sharing zigzag rows along the z direction, and corner sharing rows along the x direction [246]. These internal interactions are held by strong covalent and ionic bonds. For silicon, we considered crystals in a cubic diamond structure with a lattice constant of 5.43 Å [247], corresponding to the Fd3m space group [248]. Its structure can be seen as two interpenetrating face centered cubic sub-lattices with one sub-lattice displaced from the other by one-quarter of the distance along the

body diagonal of the cube [121]. All Si atoms are bonded to four equidistant neighbors to form a tetrahedron. Accordingly, Si is simulated in combination with α-MoO_3 to mimic the interface between the two materials, based on the Perdew-Burke-Ernzerhof (PBE) functional. We then calculated the WF of MoO_x structures as the difference between the vacuum potential and the Fermi energy [249]. For the calculation of the dipole formed at Si/MoO_x interface we used the lattice coincidence method [250].

Electrical simulations of SHJ solar cells were carried out using TCAD Sentaurus [251]. The input optical generation profile was obtained by raytracing simulations executed in GenPro4 [252]. Therefore, a two-dimensional domain of the solar cell (see Figure 3.1) is considered for the solution of drift-diffusion equations consistently coupled with charge transport models at heterointerfaces. We accounted models and parameters reported in ref [147] [253] for c-Si and thin-film silicon. Note that in TCAD we took into consideration a virtual layer to mimic the interface phenomena resulted from DFT simulations (i.e. dipole formation) [225][254].

3.3. Results and Discussion

3.3.1. Significance of Si/MoO_x interface

Electronic properties of MoO_x strongly depend on the oxidation states [164]. Moreover, by controlling the oxidation-reduction reaction between a substrate and MoO_x it is possible to adjust the WF of MoO_x [164]. Accordingly, we theoretically evaluate the Si/MoO_x interface [250]. Figure 3.2a reports the differential charge as function of the position after the formation of such interface for different oxygen content in MoO_x (x in MoO_x) from 3 to 2.875. The curves indicate the charge variation due to the interaction between the two adjacent materials. We observe that there is an interface region, which does not accomplish the lattice conditions for Si or MoO_x materials. Such a region exhibits differential charge variation due to interaction between Si and O atoms forming the Si-O bonds at the interface between Si and MoO_x. Interestingly, we observe that the largest peaks are at the edge of Si lattice (6 Å) and MoO_x lattice (8.5 Å), respectively. Such peaks exhibit similar magnitudes but opposite charge fulfilling the conditions to form a dipole [255]. Eventually, the dipole implies potential drops across the interface attenuating the WF of MoO_x. The magnitude of such dipole decreases for lower oxygen content in MoO_x as shown in the Table A.1. We then calculate the WF of MoO_x for different x by simulating different oxygen deficiencies, that is removing O3 or O2 states. Figure 3.2b shows that the WF strongly increases as x in MoO_x gets closer to 3. In fact, we observe a 2 eV rise in WF when x in MoO_x changes from 2.85 to 3. Looking at experimental evidence in literature, it is worth noting that the oxygen state of MoO_x depends on oxidation potential of the adjacent layer [166] and deposition conditions [194]. In addition, although the thickness of MoO_x does not directly denotes its oxidation state, there is a clear correlation between layer thickness and x in MoO_x, for which the thicker the MoO_x layer is, the more stoichiometric the resulting material is. This was experimentally observed in MoO_x deposited on different substrates as reported in ref [164].

In this work we are specifically interested in the (*i*)a-Si:H/MoO_x interface. Ideally, given the abovementioned dependencies, a MoO_x film should straightaway exhibit a certain WF value (anywhere between 5.8 and 7 eV [172] [256] [257] [258] as long as the

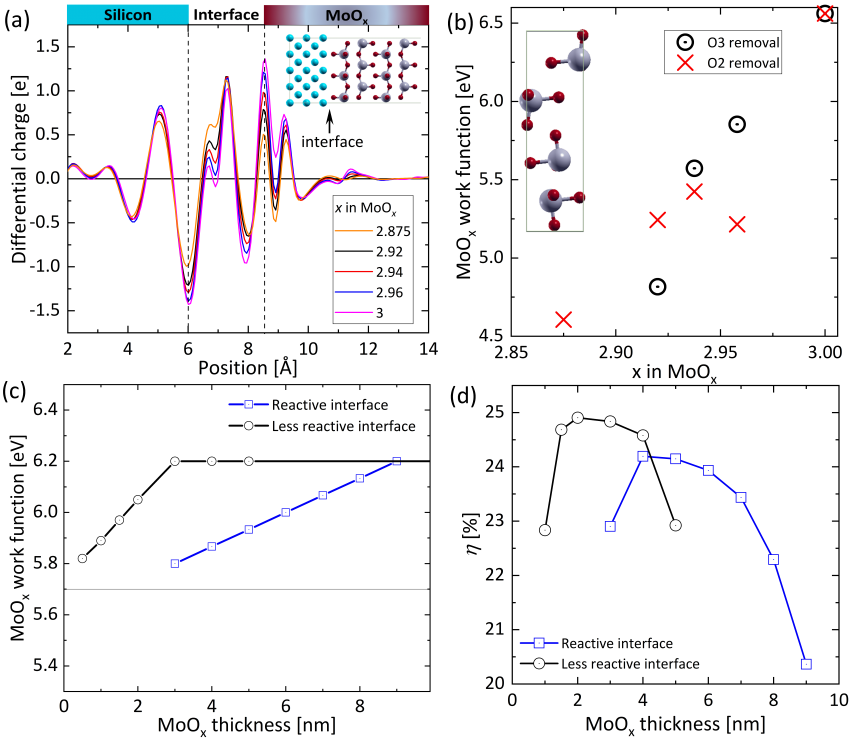

Figure 3.2: (a) Differential charge at the interface between Si and MoO_x for different stoichiometry in MoO_x. The inset depicts the cross-sectional view of the Si/MoO_x interface and the arrow indicates the 2.5-Å thick interface in which the dipole forms (silicon is represented by light blue atoms while MoO_x is represented by grey atoms for Mo and red atoms for oxygen). (b) Calculated work functions of MoO_x as a function of x in MoO_x for different oxygen deficiencies: O3 and O2 removal. The inset depicts the unit cell of MoO_3 as modeled in DFT simulations. (c) Work function profile used to emulate different (*i*)a-Si:H/MoO_x interfaces: reactive (blue squares) and less reactive (black circles). (d) Simulated conversion efficiency (n) of SHJ with MoO_x hole collector using WF profiles taken from (c) as input. Simulated *FF*, J_{SC} and V_{OC} are shown in Figure A.2.

dipole is formed between the MoO_x film and its substrate. That is, a step-like function for WF as function of MoO_x thickness should be ideally established (WF = 0 for thickness ~0 nm and WF = constant for thickness > 0 nm). However, this is not what happens as the MoO_x material grows on a substrate. The approach reported in [225] links the dependence of MoO_x WF on its thickness to the (*i*)a-Si:H WF, the built-in potential at the (*i*)a-Si:H/MoO_x interface and the attenuation of MoO_x WF due to the presence of the abovementioned dipole. Based on that approach, we expect that the dependency of MoO_x WF on its thickness reaches a saturation value which depends on (*i*) the deposition process, (ii) the growth condition of MoO_x and (iii) the reactivity of the substrate with oxygen states. In case of silicon substrate, silicon indeed reacts with the oxygen diffused from MoO_x leading to the formation of a thin SiO_x layer film at Si/MoO_x interface [166]. We illustrate this concept in Figure 3.2c, where a less reactive interface prior the MoO_x deposition would saturate the WF within a 3-nm thick MoO_x films [166], while a reactive

interface would achieve similar WF only for 9-nm thick MoO_x films [225]. The reported trend of the less reactive interface is one of the several possibilities that could be experimentally feasible between the reactive interface case on the one hand and the previously mentioned ideal WF step function on the other hand. We chose that specific trend with its saturated WF value at 6.2 eV because, once used in our TCAD-based simulation campaign to validate our simulation framework, it could explain well both our experimental trends as well as those in [225] and [66].

So, to evaluate the effect of different (*i*)a-Si:H interface conditions on SHJ solar cell performance, we performed TCAD simulations accounting for these two different WF profiles. After considering the interface dipole and SiO_x formation as reported in ref [225], we obtained the conversion efficiency (η) trends reported in Figure 3.2d as function of the MoO_x thickness. The simulated *FF*, J_{SC} and V_{OC} trends are provided in Figure A.2. We observe a bell-shaped η which is dominated by the *FF* trend as shown in Figure A.2 and discussed in [225]. The trend of η demonstrates a maximum value of 24.2% and 24.9% at around 4 nm and 2 nm MoO_x for reactive and less reactive WF profiles, respectively. Maximum values in each curve result indeed from the trade-off between WF and interfacial dipole [225]. The interfacial dipole leads to an attenuation of MoO_x WF. Accordingly, increasing MoO_x thickness amplifies WF but also the WF attenuation. Note that WF attenuation has a negative impact on the c-Si band bending and energy alignment within c-Si/(*i*)a-Si:H/TCO and thus affects the *FF* of solar cells as discussed in [225]. It is possible to achieve the best trade-off between WF and WF attenuation with thinner MoO_x in case of a less reactive surface. We observe that the highest η of 24.9% is achieved by means of a less reactive interface and for 2-nm thick MoO_x. Indeed, interfaces that are less reactive with oxygen have the potential to improve η and minimize the MoO_x layer thickness. To mitigate such oxygen reactivity with silicon molecules and therefore to control MoO_x WF and dipole formation at Si/MoO_x interface, we then proposed in ref [225] the approach to modify the interface before MoO_x deposition by applying a PECVD plasma treatment on top of (*i*)a-Si:H layer.

3.3.2. Modification of (*i*)a-Si:H to control the properties of MoO_x

We used two different plasma treatments (PT and PTB) to modify (*i*)a-Si:H before MoO_x deposition as described in Section 3.2.1. Accordingly, we evaluate the oxygen (O) vacancies in MoO_x films for three different interface conditions: without treatment (noPT), PT and PTB. Among these interface conditions, we also evaluate oxygen vacancies in samples with different MoO_x thickness: 1, 1.7, 2, 2.9 and 4.1 nm. Additionally, we included a 20-nm thick MoO_x sample as reference. Then, we conducted XPS to evaluate the elemental composition of these samples. Figure 3.3a shows the valence band photoemission spectra of MoO_x. We relate this parameter with the gap states between the Fermi level and valence band [164] and they are indicated as d1 and d2. The idle oxidation state of Mo is +6, corresponding to MoO_3 (see Figure A.2). Instead, the gap states are the dominant defect resulting in degradation of Mo cation state from +6 to +5 [120] [259]. In general, we observe that (i) samples with noPT show the highest gap states concentration and (ii) the gap states signal decreases for samples with thicker MoO_x layer. Note that the 20-nm thick MoO_x sample exhibits almost no signal of gap states. This is consistent with observation from Mo core-level spectra as shown in Figure A.2. In fact, according

to the Mo core-level spectra, we confirm the presence of different Mo oxidation states (Mo^{+6} and Mo^{+5}) in different MoO_x-thickness films. These results are in agreement with observations reported in [244] by evaluating Mo oxidation states in MoO_x layers grown onto different reactive substrates [166]. As the Mo^{+5} decreases when the thickness of MoO_x film increases, we can correlate such a reduction to an increase in MoO_x WF. Thus, we expect a rise in the WF for thicker MoO_x samples [223] [224]. We notice that all three interface conditions (noPT, PT and PTB) show a similar trend. Also, we see that gap states signal is lower for PT than PTB and noPT in case of samples with MoO_x layer thinner than 2.9 nm. Figure 3.3b shows the O and Mo content calculated from XPS as a function of the thickness of MoO_x samples. In particular, the atomic concentration of O and Mo under three conditions and for 1-nm thick and 1.7-nm thick MoO_x are provided in Table A.2. In general, we observe that molybdenum content remains the same independently of the interface condition. However, the O content increases with the layer thickness for the three different treatments. We noted that O content is the lowest for noPT samples which indicates that MoO_x layers is less stoichiometric compared to PTB and PT cases. MoO_x samples treated with PT exhibit higher oxygen content. This trend is observed systematically up to 2.9 nm, after this value the effect of PT or PTB is not detectable. This suggests that noPT samples exhibit interface features allowing oxygen to diffuse from MoO_x. Instead, PTB and PT processes modify the interface preventing the oxygen diffusion from the MoO_x layer. Moreover, looking at the oxygen content of MoO_x films and its relation to the WF reported in ref [260], we expect that samples with PT provide the highest WF followed by those with PTB and noPT.

3.3.3. The role of oxygen at (*i*)a-Si:H/MoO_x interface

To evaluate the element composition and the morphology of the (*i*)a-Si:H/MoO_x interface, we conducted HR-TEM and EDX measurements for solar cells fabricated under different interface conditions (i.e. noPT, PT and PTB) with nominal 1.7-nm thick MoO_x layer and including the IWO as TCO layer. As this thickness yields the best performing solar cells (see Section 3.3.4), it was chosen for this evaluation. Figure 3.3c shows the EDX map and the element composition profile of Si, O, Mo, In and W. The origin of depth profiling analysis was set at the interface between c-Si bulk and the (*i*)a-Si:H layer (see detailed cross-sectional TEM images in Figure A.3) and EDX raw data in Figure A.7. Note also that we evaluate the thickness of each (sub) layer in the supporting information Figure A.3.

We observe that samples with PT and PTB exhibit a thicker Si-rich layer than the sample with noPT. This suggests that PT and PTB form on the original (*i*)a-Si:H layer an interlayer with different interface conditions with respect to the sample with noPT . In case of PT, as observed in [261] too, we speculate that oxygen radicals do not incorporate in film incubation phase (~2 nm) under the aforementioned plasma processing conditions. In case of PTB, the presence of boron radicals in the plasma leads to faster reaction [262] with oxygen atoms that are incorporated in the film nucleation phase. In this scenario boron atoms act no longer as a dopant, but as oxidation agent [263]. This is consistent with XPS and TEM measurements in which boron cannot be detected (see Figure A.4 and Figure A.5). For the noPT sample, we note in both Figure 3.3c and Figure A.4 that oxygen is extended inside (*i*)a-Si:H forming an oxygen-rich interlayer at (*i*)a-Si:H/MoO_x interface. We ascribe the origin of such a sub-layer to the O diffusion from MoO_x to the

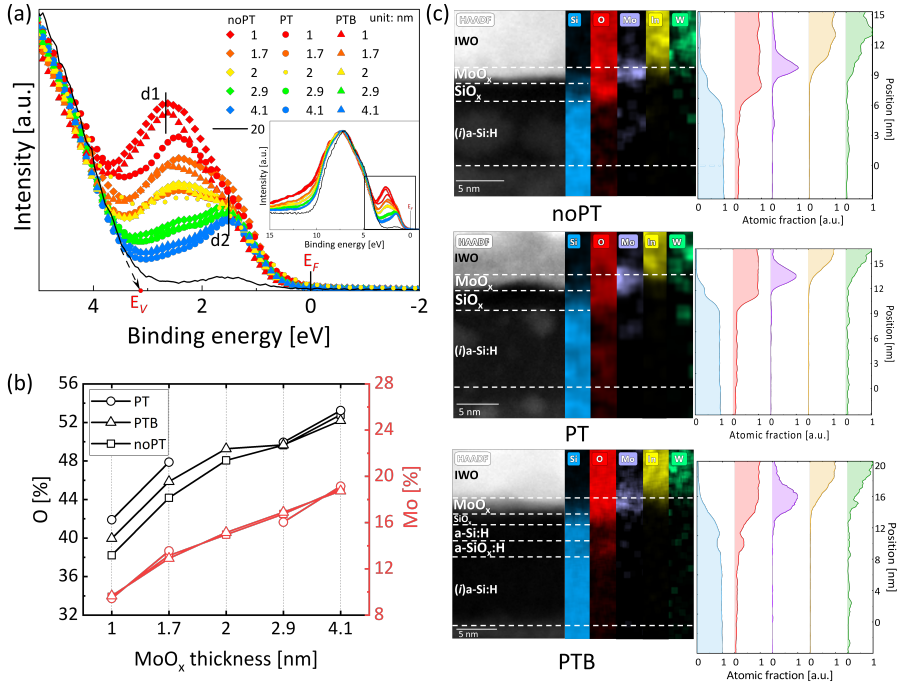

Figure 3.3: (a)Valence band spectra of as-deposited MoO_x surface for variable thicknesses and noPT, PTB and PT. d1 and d2 indicate the gap states caused by O vacancies (the inset zooms out these spectra in a wider binding energy range); (b) the Mo and O content as a function of MoO_x thickness under different treatment calculated from XPS spectra (see Supp.info Figure A.2); (c) EDX and atomic profile of noPT sample (top), PT sample (middle) and PTB sample (bottom).

interface resulting in 2.2-nm thick SiO_x interlayer. The MoO_x thickness mentioned later was calculated from the Mo and In atomic profiles, because these two atomic distributions have clear boundaries as shown in Figure 3.3c. The overlap area in the Mo and In atomic profile are ascribed to the intermixing layer [68] formed during IWO-sputtering process. In this sample, we observe the formation of ~2-nm thick MoO_x layer. In the sample with PT, we note instead the formation of 2-nm thick SiO_x interlayer and a ~2-nm thick MoO_x film. The sample with PTB exhibits the formation of a thinner SiO_x interlayer (1 nm) at (*i*)a-Si:H/MoO_x interface and ~2.2-nm thick MoO_x film. However, there is an additional 1.5-nm thick a-Si:H and 1.8-nm a-SiO_x:H layer above (*i*)a-Si:H formed during PTB. The atomic fraction of O, Si and Mo of such interlayers are shown in Figure 3.3c. As mentioned earlier, we note that Mo diffuses also inside IWO (W-rich) layer for all samples, for which the element profiles of Mo, O and In (see Figure 3.3c) reveal the formation of a transition interlayer at the MoO_x/IWO interface. We suppose the mixing layer is formed during the IWO deposition process due to the sputtering process. These observations are consistent with findings reported in ref [68]. Ultimately our elemental process indicates that the MoO_x layer is affected by two main interfaces - (*i*)a-Si:H/MoO_x and MoO_x/IWO - that concurrently affect the electronic properties of MoO_x.

3.3.4. Solar cells' performance

Finally, we evaluate the solar cell parameters using the nominal 1.7-nm thick MoO_x layer with different interface treatments (noPT, PT and PTB). The external parameters are reported in Figure 3.4a. We observe that V_{OC} and *FF* exhibit the highest (719 mV, 80.66%) and lowest (715 mV, 79.16%) for samples with PTB and noPT, respectively. This result is consistent with ρ_c values reported in Figure 3.4b and with findings in ref. [167]. In fact, we observe the lowest ρ_c value of 177 mΩ·cm^2 for sample with PTB. NoPT and PT result in ρ_c in the range of 600 to 1400 mΩ·cm^2. We can relate that a-Si:H and a-SiO_x:H interlayer formation during PTB process, together with higher oxygen content in MoO_x layer, leads to transport improvement in the contact stack with PTB. We infer that samples with PT MoO_x could exhibit higher WF than samples using PTB due to the higher oxygen content (see Figure 3.3b). However, we suspect that PTB samples result in the lowest ρ_c due to the best trade-off between WF and interfacial dipole [225]. Samples with noPT exhibit high ρ_c due to high oxygen reaction at (*i*)a-Si:H/MoO_x interface together with lower oxygen content in MoO_x (relatively low MoO_x WF) as discussed in the previous section.

We note that the trend is opposite for short circuit current (J_{SC}) as Figure 3.4a illustrates. The samples without any treatment (noPT) yield the highest J_{SC}). This is ascribed to the fact that interface modification (i.e. PT and PTB) leads to the growth of ~3-nm thick interlayer (see Section 3.3.3) which increases the parasitic absorption in samples with PT and PTB. Such interlayer causes J_{SC} losses of 0.2 - 0.4 mA/cm^2 compared to samples with noPT. Note that XPS and EDX measurements show that PTB does not result in boron incorporation. In general, η follows the trend of V_{OC} and *FF* with highest value of 23.83% for samples with PTB.

As PTB solar cells exhibit the highest efficiency in our study (Figure 3.4c), we evaluate the effect of MoO_x thickness for such treatment. Solar cell performance of devices fabricated with noPT for variable MoO_x thickness were investigated in the early development of this method. Related results reported in our previous work [225] were not encouraging. To do so, we variate the MoO_x layer from 1 to 4 nm. The results are reported in Figure 3.4c. V_{OC} of the devices increases as the thickness of MoO_x reaches 1.7 nm and remains constant at around 719 mV for samples with MoO_x thicker than 1.7 nm. *FF* exhibits a bell-shape trend with a maximum average value of around 81.5% for 2-nm thick MoO_x. This trend is consistent with theoretical findings in Section 3.1 and ρ_c measurements reported in Figure 3.4d.

As anticipated, increasing MoO_x thickness, J_{SC} slightly decreases from 40.2 to 39.8 mA/cm^2 due to parasitic absorption. Furthermore, the EQE of the best MoO_x cell compared to the the SHJ counterpart is shown in Figure 3.4e. We observe that the EQE spectrum exhibits an improvement in light response at wavelength range from 300 nm to 800 nm corresponding to a gain of 2.77 mA/cm^2. We observe that the η trend is dominated by the *FF*. Indeed, the best trade-off between optics and electrical behavior (J_{SC} vs FF^*V_{OC}) results in an optimal solar cell with 1.7 nm MoO_x. Figure 3.5 shows the certified *J-V* curve of our best performing solar cell.

3.4. Conclusion

In this work, we identified the fundamental mechanisms for tailoring properties of MoO_x and for its integration in high efficiency SHJ solar cells. Our simulation results revealed

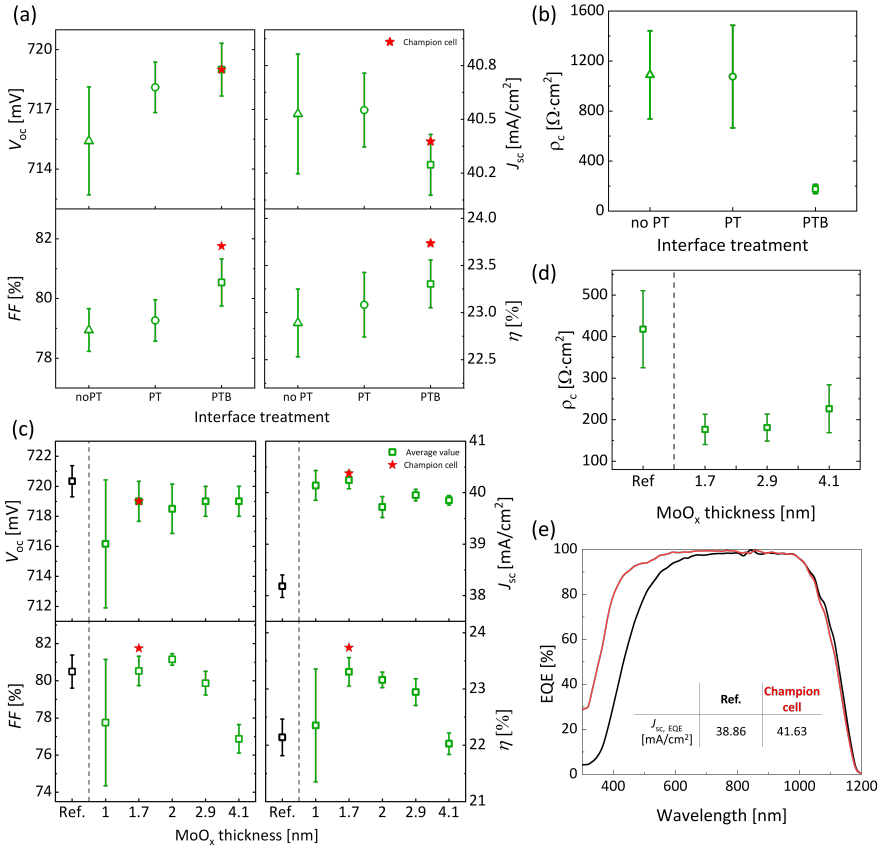

Figure 3.4: (a) The parameters extracted from *J-V* curve of solar cells with various interface treatments at 1.7-nm thick MoO_x (the error bar is calculated from 12 solar cells on 4 wafers for noPT, 9 solar cells on 3 wafers for PT and 18 solar cells on 6 wafers for PTB); (b) contact resistivity of different treatments applied before depositing 1.7-nm thick MoO_x; (c) The parameters extracted from *J-V* curve of solar cells with PTB and various MoO_x-thickness (the error bar is calculated from 6 solar cells on 2 wafers for Ref., 1 nm and 2 nm cases; from 3 solar cells on 1 wafer for 2.9 nm and 4.1 nm cases; from 18 solar cells on 6 wafers for 1.7 nm case); (d) contact resistivity of different MoO_x thickness with PTB, including a *p*-type layer as reference. (The empty symbols stand for the standard average value and the standard error bar is calculated from multiple samples; the red star symbol represents the external parameters of the champion cell). (E) EQE spectra of the reference SHJ solar cell and champion MoO_x solar cell.

that the oxygen content inside MoO_x strongly affects the WF and additionally leads to the formation of a strong dipole at the interface with silicon. Therefore, thickness dependent WF profile depends on the diffusion of oxygen from MoO_x through (*i*)a-Si:H. Then, by controlling the oxygen content in MoO_x, we calculated that optimal solar cells are possible for ~2-nm thick ultra-thin MoO_x films because of the trade-off between dipole and MoO_x WF. With this observation, we investigated the effect of PT and PTB on MoO_x film oxygen content. By evaluating XPS measurements, we observed that oxygen content in MoO_x

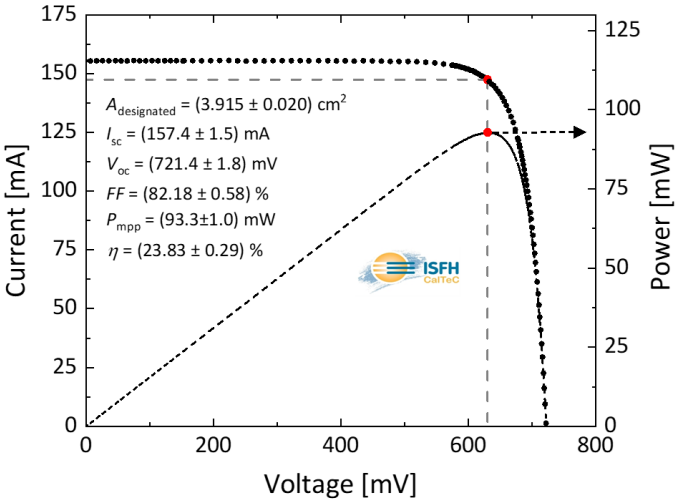

Figure 3.5: ISFH CalTeC certified *J*-*V* and *P*-*V* curves of our champion cell based on 1.7-nm thick MoO_x and PTB.

layers deposited after PT and PTB conditions is higher than that in MoO_x layers deposited in noPT condition. This finding suggests adjustable WF for PT and PTB samples as WF increases with oxygen content in MoO_x. HR-TEM and EDX images confirmed the formation of a SiO_x interlayer at (*i*)a-Si:H/MoO_x interface. We noted that samples with PT and PTB exhibited thinner SiO_x interlayer compared with samples with noPT, thus confirming that PT and PTB indeed reduce the reaction of the (*i*)a-Si:H/MoO_x interface with oxygen from MoO_x. We evaluated the transport of the contact stack in terms of ρ_c of samples with noPT, PT and PTB. Our measurements revealed a minimal ρ_c = 177 mΩ·cm^2 for a contact stack with PTB and 1.7 nm MoO_x. Then, we studied the impact of the interface treatment and MoO_x-thickness on the performance of MoO_x-based SHJ solar cells. Overall, we applied optimal PTB at (*i*)a-Si:H/MoO_x interface and realized a champion cell with 1.7-nm (2.2-nm measured by TEM) thick MoO_x as a hole transport layer. With 23.83% conversion efficiency and a *FF* equal to 82.18%, we push further the performance of TMO materials integrated in c-Si solar cell architectures. Furthermore, plasma processes applied here (PT and PTB) for reaching high performance solar cells are compatible with industry SHJ production lines.

4

Indium reduction in bifacial SHJ solar cells with MoO_x collector

This chapter was published in *Advanced Energy and Sustainability Research* * [50]

Abstract

Reduction of indium consumption in transparent conductive oxide (TCO) layers is crucial for scaling up silicon heterojunction (SHJ) solar cells. We designed and optimized SHJ solar cells using MoO_x hole collectors and ultra-thin TCO layers with optical simulations. First, bifacial SHJ solar cells with MoO_x as the hole transport layer (HTL) and three types of *n*-contacts were fabricated with 50-nm thick ITO on both sides. Bilayer (nc-Si:H/a-Si:H) and trilayer (nc-SiO_x:H/nc-Si:H/a-Si:H) n-contacts performed better than monolayer (a-Si:H) in bifacial SHJ cells. Next, using optical simulations, we optimized SHJ solar cells with tungsten-doped indium oxide (IWO) and MgF_2 layers on both sides. Devices with 10-nm thick IWO and bilayer *n*-contacts achieved certified efficiency of 21.66% and 20.66% from MoO_x and *n*-contact sides, respectively. When illuminated from the MoO_x side, the short-circuit current density and fill factor were above 40 mA/cm^2 and 77%, respectively. This results in over 90% TCO reduction compared to standard SHJ solar cells. For bifacial cells with 50-nm thick IWO layers, a champion device with bilayer n-contact achieved a certified efficiency of 23.25% and 22.75% from MoO_x and n-layer sides, respectively, with a bifaciality factor of 0.98. Using a *n*-type bilayer stack, the bifaciality factor is above 0.96 and can reach up to 0.99 with a *n*-type trilayer stack. This results in a TCO reduction of more than 67%.

*Cao, L., Zhao, Y., Procel Moya, P., Han, C., Kovačević, K., Özkol, E., Zeman, M., Mazzarella, L., and Isabella, O. (2024). Indium Reduction in Bifacial Silicon Heterojunction Solar Cells with MoO_x Hole Collector. Advanced Energy and Sustainability Research, 2400105.https://doi.org/10.1002/aesr.202400105

4.1. Introduction

Front/back-contacted (FBC) silicon heterojunction (SHJ) solar cells have achieved a remarkable conversion efficiency of 26.81% [55]. However, the use of critical raw materials such as indium, silver and bismuth represent a challenge to realize mass production of SHJ solar cells at the multi-terawatt scale [46]. Especially, the sustainable production capacity of SHJ solar cells is limited to only 37 GW due to the scarcity of indium supply [46]. Therefore, mitigating or minimizing the utilization of indium in SHJ solar cells is crucial to ensure their sustainability for mass production.

Conventionally, the front/rear thickness of transparent conductive oxide (TCO) layers in SHJ solar cells is between 75 nm and 150 nm, respectively [236]. A TCO layer provides both lateral and vertical transport for charge carriers and protects the underlying layers from metal contact. From an optical point of view, TCO ensures light in-coupling for its thickness-tuneable anti-reflective effect. Furthermore, TCO works as a barrier layer against copper diffusion when applying copper plating as the metallization method [45].

As reported in the literature, there are three main strategies to reduce In consumption. The most straightforward solution is to utilize In-free TCOs, such as aluminum-doped zinc oxide (AZO) [264–266]. However, more efforts are required to reduce the degradation of *FF* and to improve the stability of AZO films [267–269]. A second approach is to develop TCO-free SHJ solar cells [270, 271]. However, the passivation degrades during metallization process due to lack of a buffer layer. Besides, as the TCO layer contributes to charge transport, the carrier collection efficiency will decrease in absence of a TCO. Both passivation degradation and carrier collection require more research effort to fully optimize this structure [272]. Researchers have worked on minimizing the passivation loss induced by metallization process through the utilization of a rather thick doped silicon-based layer. However, this approach resulted in the significant parasitic absorption losses [270]. Instead of completely removing the TCO layers, a third solution is to reduce the thickness of TCO layers as compared to typically used TCO thicknesses [49]. Notably, simply reducing the thickness of the TCO layer, which also serves as the anti-reflection coating (ARC) and rear reflector in monofacial SHJ solar cells, will result in increased optical losses in SHJ solar cells. To maintain the good optical response of the solar cells, thinner-than-standard TCOs on the illuminated side are to be combined with an additional transparent layer (e.g., magnesium fluoride, MgF_2), forming a double-layer anti-reflection coating (DLARC). The use of DLARC would significantly reduce reflection losses and improve the current density of the solar cells [37, 48]. Moreover, by inserting a dielectric layer between the TCO and the metal electrode on the rear side, an efficient back reflector can be also formed [273]. This is beneficial when reducing the TCO thickness on the rear side of monofacial SHJ solar cells. In the case of TCO reduction in bifacial SHJ solar cells, use of DLARCs on both sides of the SHJ solar cells is essential to maintain good optical response of solar cells [37, 48, 274, 275].

Moreover, it was reported that TCO reduction can be more effectively realized in bifacial SHJ solar cells as compared to monofacial SHJ solar cells [48, 49], as the thickness of both front and rear TCO layers can be decreased to at least 50 nm. So, it will reduce the TCO consumption by 67%. Remarkably, bifacial solar cells could achieve higher annual energy yield compared to monofacial devices [230], benefiting from the property that light can be absorbed from both sides of the cells. Therefore, in order to achieve better-

performing bifacial solar cells, the optical response of the window layers on both sides of the solar cell need to be considered. To achieve both high transparency and conductivity simultaneously, materials such as transition metal oxides (TMO) could be one of the options [271]. For example, MoO_x exhibits higher transparency than silicon-based doped layers [102] and has proven to be an efficient hole transport layer (HTL) in monofacial SHJ solar cells [225]. Therefore, MoO_x can be used at the front side in bifacial SHJ cells. Besides, it is also important to minimize parasitic absorption losses originating from the rear sides of the cells. Silicon-based materials such as doped hydrogenated nanocrystalline silicon (nc-Si:H) and its alloyed version with oxygen (nc-SiO_x:H) are preferred as the electron transport layer (ETL) on the rear side of SHJ solar cells as compared to typically used (*n*)a-Si:H [188, 276–280].

Aiming at reducing indium consumption, we explore the possibility of lowering the thickness of indium based TCO layer while avoiding degradation in cell performance. First, we evaluate the performance of bifacial SHJ solar cells featuring various rear-side *n*-contact, namely, monolayer (a-Si:H), bilayer (nc-Si:H/a-Si:H), and trilayer (nc-SiO_x:H/nc-Si:H/a-Si:H), combined with MoO_x at the front side. Then, the optical and electrical properties of thin-film IWO deposited on glass substrates with varied thicknesses from 10 nm to 50 nm are assessed. Subsequently, optical simulations are carried out to investigate the optical potential of bifacial SHJ solar cells utilizing ultra-thin IWO films in combination with MgF_2 films to form DLARCs. Eventually, bifacial SHJ solar cells with ultra-thin IWO films are manufactured and analyzed.

4.2. Experiment

4.2.1. Solar cells with different *n*-type layers

The samples were prepared using 4-inch double-side-polished *n*-type float zone (FZ) wafers with <100> orientation. The resistivity and thickness of the wafers were 3 ± 2 Ω·cm and 280 ± 20 µm, respectively. The wafer texturing process was conducted in a TMAH solution with ALKA-TEX as an additive [240]. Next, the wafers were cleaned using wet-chemical cleaning and subsequent dipping in 0.55% hydrogen fluoride (HF) for 5 min [235]. Afterwards, the wafers were loaded into a multi-chamber plasma enhanced chemical vapor deposition (PECVD) equipment for the deposition of thin-film silicon layers. (*i*)a-Si:H layers were deposited on both sides of the wafers and three different types of electron transport layers (ETL) were deposited at the rear side: (i) 4-nm monolayer (*n*)a-Si:H, (ii) bilayer with 3 nm (*n*)nc-Si:H / 2 nm (*n*)a-Si:H [236], (iii) trilayer with 8nm (*n*)nc-SiO_x:H / 3 nm (*n*)nc-Si:H / 2 nm (*n*)a-Si:H in [58, 238]. Subsequently, (*i*)a-Si:H layer was deposited on the front side of the samples. An interface treatment, namely PTB[46], was introduced during the Plasma-Enhanced Chemical Vapor Deposition (PECVD) process. This treatment involved the utilization of a gas mixture containing SiH_4, H_2, CO_2, and B_2H_6, which was highly diluted with hydrogen (~170 sccm). PTB was applied prior to the thermal evaporation of MoO_x, more detailed information can be found in our previous work [225]. After that, optimized TCO layers were sputtered through a hard mask at front and rear side, respectively, defining six 2 × 2 cm^2 solar cells per wafer [239]. The front and rear metal electrode consists of simultaneously electroplated Cu fingers at room temperature on top of 200-nm thick thermally evaporated Ag seed layer [241]. The width

of the fingers was 15 µm and the pitch between two fingers was 915 µm. Finally, MgF_2 films were e-beam evaporated on both sides as additional anti-reflection coating layers.

4.2.2. Deposition of IWO films

Corning glasses were used as the substrate for the deposition of IWO films; and they were cleaned by isopropyl and acetone in a supersonic bath for 10 min each. IWO films were deposited on cleaned Corning glasses by RF magnetron sputtering technique (Polyteknic AS) at room temperature. Ar was used as the sputtering gas with a flow of 20 sccm (mixed with 0.25% O_2). The pressure of the deposition chamber was 4.0×10^{-3} mbar and the power density was around 0.8 W/cm^2. The target composition of IWO was 95 wt% In_2O_3 and 5 wt% WO_3. The base pressure of the chamber before deposition is below 1×10^{-7} mbar. The deposition rate was around 2 nm/min on flat surface. Since the surface of wafer-based substrates was textured, the deposition time is calculated by multiplying a geometrical factor of 1.7 based on the deposition time on the flat surface. To cure the passivation quality damaged by ion bombardment during the sputtering, a post-annealing treatment was performed in an oven with air atmosphere at 180 °C for 5 min. Carrier concentration, Hall mobility, and resistivity of the samples were obtained from Hall Effect measurements.

4.2.3. Characterizations

Effective minority carrier lifetime was measured at different steps of the fabrication flow chart by Sinton WCT-120 equipment. Current-voltage characteristics of solar cells were determined using an AAA-rated Wacom WXS-90S-L2 solar simulator under standard test conditions (STC). A specially designed chuck for bifacial solar cell measurement was in-house design and realized for bifacial solar cell measurements. In this chuck, a specialized substrate was utilized which displayed a reflectance of less than 3.5% across the wavelength range of 700-1200 nm. The substrate's reflectance and transmittance curves have been presented in previous work of our lab [241]. By mounting the wafer directly on this substrate during the *J-V* measurements, the influence of rear-side illumination on the front-side measurements was effectively mitigated, with the controlled amount remaining below 3 W/m^2 [275]. The *J-V* data was obtained separately from both sides of the SHJ devices. In this work, the bifaciality factor (φ) is defined as $\varphi = \eta_N / \eta_P$. η_N is the efficiency measured from the *N*-side and η_p is the efficiency measured from the *P*-side.

4.3. Results and discussion

4.3.1. The influence of different *n*-type layers on cell performance

We first investigated the performance of solar cells fabricated with three different *n*-contact depicted in Figure 4.1a, consisting of (i) a monolayer (a-Si:H), (ii) a bilayer (nc-Si:H/a-Si:H) or (iii) a trilayer (nc-SiO_x:H/nc-Si:H/a-Si:H). At this initial stage, we applied 50-nm thick ITO on both sides of bifacial FBC-SHJ solar cells. The external parameters are reported in Figure 4.1b. We measured the solar cells without and with an additional 100-nm thick MgF_2 to form a DLARC with ITO on both sides of the solar cells. The results obtained by illuminating the solar cells from MoO_x and n-contact are marked as *P*-side and *N*-side, respectively. The results are presented in Figure 4.1b and 4.1c.

As depicted in Figure 4.1b, prior to the application of MgF_2, the open-circuit voltage (V_{OC}) of the solar cells when illuminated from the *P*-side is quite similar. However, the data measured for illumination from the *N*-side are different due to different *n*-type layer stacks. Specifically, the bilayer structure provides better passivation effect compared to the other two *n*-contacts [236]. The short-circuit current densities (J_{SC}) measured from the *P*-side share similar values for bilayer and trilayer samples and slightly higher than the values measured from monolayer samples. The J_{SC} values measured from *N*-side are quite different, which the trilayer samples exhibiting the highest J_{SC}, followed by bilayer and monolayer samples. This is attributed to the nc-SiO_x:H layer displaying significantly lower parasitic absorption in comparison to nc-Si:H and a-Si:H layers [236, 280]. On the other hand, the *FF* values measured from bilayer samples achieved highest value, followed by monolayer and then trilayer samples. This may be attributed to the better electronic properties of the nc-Si:H layer compared to other two layers [236].

After applying the additional MgF_2 layers, similar trends on V_{OC} are found for all three *n*-contacts. Nevertheless, when solar cells were illuminated from the *N*-side, their *FF*s were slightly higher compared to those illuminated from *P*-side within each group. These results demonstrate that the carrier transport property of the *N*-side is better than the *P*-side.

To be more specific, as shown in Figure 4.1b, the bilayer *n*-type stack exhibits the highest *FF* among all *n*-contacts investigated, then followed by the monolayer (*n*)a-Si:H, and lastly, by the trilayer stack. This is mainly due to the rather thick (~ 10 nm) and the less favorable electrical properties of (*n*)nc-SiO_x:H [236, 237]. The *FF* is negligibly influenced by the deposition of MgF_2. There is a noticeable variation in J_{SC} when solar cells were illuminated from N and P sides within each group. Specifically, the J_{SC} is generally higher when the cells are illuminated from the P side compared to when illuminated from *N*-side. This can be explained by better transparency of MoO_x. When comparing cells with different n-contacts, we note that the trilayer-stack delivers the best light response of solar cells, which exhibits average gains of 0.8 and 1.2 mA/cm^2 as compared to bilayer-stack and monolayer (*n*)a-Si:H, respectively.

The φ of the devices is calculated and shown in Figure 4.1c. Solar cells with monolayer- and trilayer-stack exhibit the best bifaciality factor of 0.99, indicating the capability of realizing higher power generations as compared to monofacial cells. It is noticeable that the φ of few samples featuring monolayer are above 1 which suggest the efficiency measured from *N*-side is higher than the *P*-side. This could be attributed to fluctuations during fabrication and measurement process. While the φ of cells with bilayer-stack is around 0.96, which is mainly caused by higher *FF* for the *P*-side illumination and slightly lower J_{SC} for the *N*-side illumination as compared to the other two types of n-contact. The champion cell with bilayer-stack exhibits a conversion efficiency of 23.62% when measured from the *P* side (V_{OC} = 715 mV, J_{SC} = 40.98 mA/cm^2, *FF* = 80.6%) and 22.83% efficiency from the *N* side (V_{OC} = 714 mV, J_{SC} = 39.67 mA/cm^2, *FF* = 80.6%). According to our findings, bilayer and trilayer stacks exhibit higher conversion efficiency for the application in bifacial solar cells. Therefore, we will utilize these two n-contact in the following experiments.

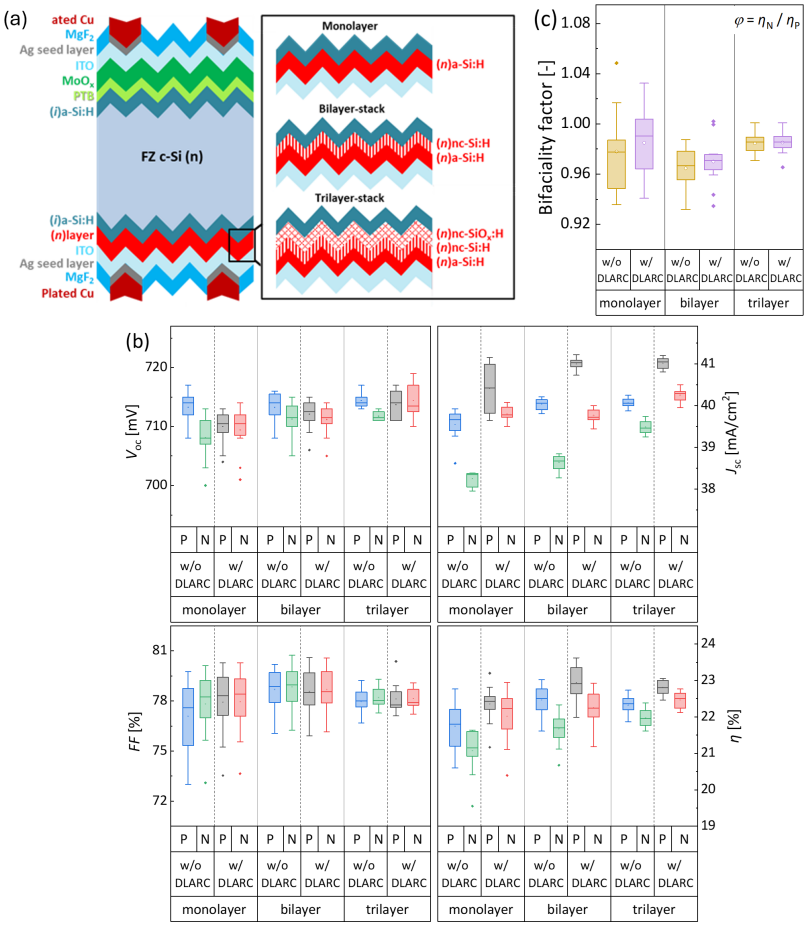

Figure 4.1: (a) Schematic illustration of bifacial SHJ solar cells with three types of *n*-layer stacks. (b) The external parameters of bifacial cells with different *n*-layer stacks, and (c) the bifaciality factors. All the cells are measured by illuminating either the MoO_x or the *n*-layer side indicated as *P* and *N*, respectively. 12 cells with 50-nm thick ITO on both sides are included in each box plot.

4.3.2. Optical and electrical properties of IWO

In comparison to ITO films, IWO films demonstrate better light response due to lower absorption in the wavelength range of interest [239]. As the TCO properties are influenced by the layer's thickness [281], to eventually implement ultra-thin TCO layers into solar cells, the opto-electrical properties of IWO with different thickness are evaluated. The carrier density (N_e), mobility (μ_e), and resistivity (ρ) of the IWO film exhibit variations as a function of thickness, as illustrated in Figure 2. The results show that, the N_e and μ_e increase and the ρ decreases as the IWO thickness increases.

The correlation between a decrease in ρ and an increase in thickness could be elucidated by the crystalline structure of the film. According to reported research, an increase in film thickness is associated with a growth in the grain size of the IWO, resulting in a

decline of electrical resistivity through more effective doping and a reduction in grain boundary scattering [282, 283]. Additionally, the enhancement in film crystallinity that occurs with increased thickness is believed to contribute to an increase in μ_e [282, 284, 285].

After the annealing process step, which was required to recover passivation after sputtering in our SHJ cell fabrication process, the mobility of IWO layers improved [286] while the N_e of these films showed slight decrements. For instance, the N_e of 50 nm thick IWO film decreased from 3.0×10^{20} cm^{-3} to 2.5×10^{20} cm^{-3}. The N_e decreases after annealing could be caused by oxygen incorporation [239]. On the other hand, the μ_e increased after annealing especially for 10 and 20-nm thick IWO samples. The μ_e of 10-nm thick IWO increases significantly from 29 to 34 $cm^2V^{-1}s^{-1}$ after annealing. This phenomenon could be explained by that thinner layer is more sensitive to annealing [287].The improvement may be more significant when annealing the thin IWO films. However, ρ is also increased after annealing. We notice that the ρ of 10-nm thick IWO sample increased from 34×10^{-4} Ω·cm to 62×10^{-4} Ω·cm. An increase in ρ and a decrease in N_e will lead to decreased carrier transport efficiency in the device, ultimately affecting *FF* values [284, 288].

Furthermore, the electrical properties of the IWO relate to the optical properties [289]. Figure 4.2d shows the complex refractive index (n) and the extinction coefficient (k) as a function of IWO thickness. Both as-deposited (solid lines) and thermally annealed (dashed lines) IWO films are plotted.

In terms of the n, the curves generally start at relatively high values for shorter wavelengths, followed by a decrease toward longer wavelengths. Such dispersion behavior is common in TCOs, reflecting both band-to-band transitions and free-carrier contributions [284, 290]. The samples exhibit generally similar n across the measured spectral range. Compared with the as-deposited samples, the annealed thicker films (> 20 nm) typically display a slightly increase in n, indicating reduced porosity and improved crystallinity by the annealing process [291].

The k is plotted on a logarithmic scale. It reveals the absorption characteristics of IWO films. At short wavelengths , k can be larger due to band-edge transitions or free-carrier effects, whereas at longer wavelengths it often drops to very low values (below 10^{-3}), signifying minimal absorption in the near-infrared range [289]. Film thickness also plays a role, with thicker layers generally showing a slightly higher k in the short-wavelength region, probably coming from the greater total volume of absorbing material [292]. Crucially, post-deposition annealing tends to reduce k at most wavelengths, reflecting a lower optical loss. This improvement in transparency is attributed to the passivation of defect states, improved crystallinity, and a reduction in free-carrier absorption [293].

4.3.3. Optical simulation results with ultra-thin IWO

To investigate the optical potential of our bifacial SHJ solar cells while reducing the thickness of In-based TCO layers, I performed optical simulations using GenPro4 [252]. The simulation results, shown in Figure 4.3, are based on the schematic structure of the bifacial SHJ solar cell in Figure 4.1a. To reduce the parasitic absorption losses induced by ITO films on both sides of solar cells, optimized IWO layers were used instead [48]. Besides, as already demonstrated in [48], bifacial SHJ solar cells with good electrical performance can be achieved with only 25-nm thick TCO layers when combined with

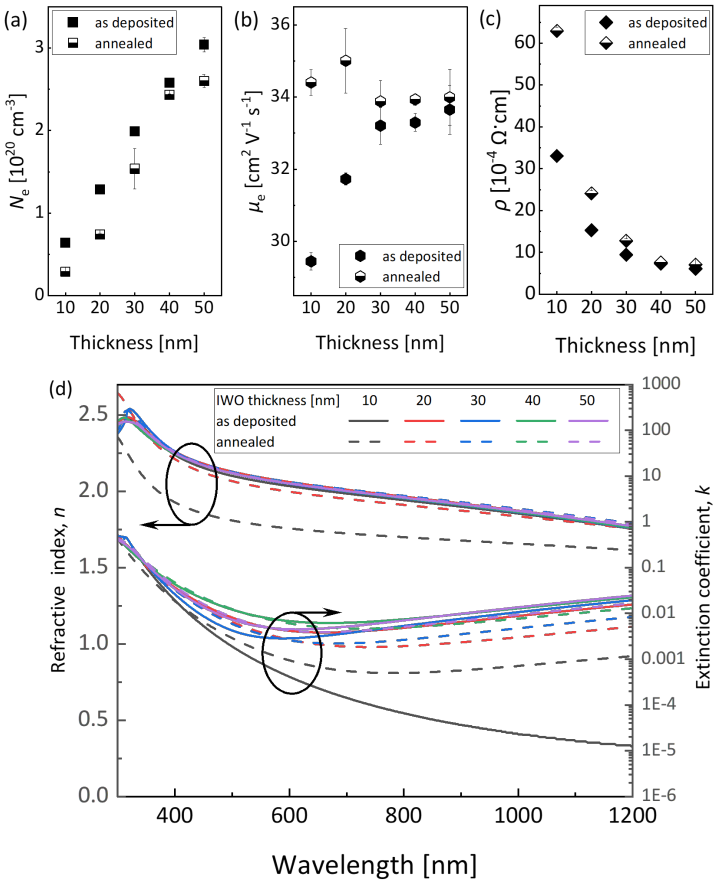

Figure 4.2: (a-c) Carrier density (N_e), mobility (μ_e) and resistivity (ρ) as a function of IWO thickness measured before and after annealing. (d) Complex refractive index of IWO layers with different thicknesses (left axis: refractive index; right axis: extinction coefficient).

around 100-nm thick SiO_x on both sides, forming double-layer anti-reflection coatings (DLARC). MgF_2 as an alternative DLARC with lower refractive index comparing to SiO_2, was applied in optical simulation. In the optical simulations, we varied IWO thickness from 10 nm to 50 nm on both sides of the device as well as the MgF_2 layer thickness. The incident light intensities at the P side and N side are 1000 W/cm^2 and 200 W/cm^2, respectively [294]. The implied photocurrent density of bifacial cells ($J_{\text{implied-bifi}}$) was calculated by summing up the implied photocurrent densities' (J_{implied}) contributions obtained from both sides.

To elucidate the increase of J_{implied} ($\Delta J_{\text{implied}}$) from monofacial to bifacial structures, we conducted simulations on implied photocurrent density of front side ($J_{\text{implied-front}}$) and implied photocurrent density of the bifacial solar cell with 1.0 Sun illumination at the front side and 0.2 Sun illumination at the rear side. Results of that simulation campaign are reported in Figures B.1-B.3. The white star in Figure 4.3 indicates the highest $J_{\text{implied-bifi}}$

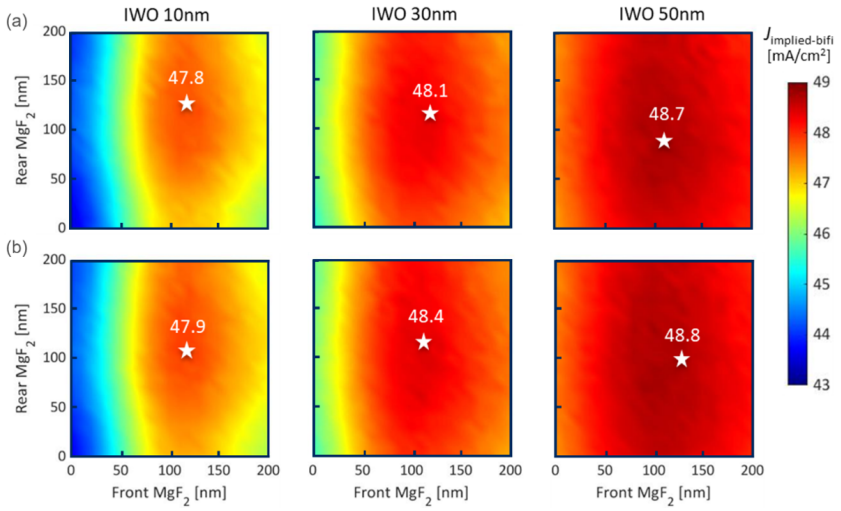

Figure 4.3: Optical simulation results of bifacial solar cells with (a) bilayer *n*-type stack and (b) trilayer *n*-type stack. The white star represents the optimal combination of MgF_2 thickness on the front and rear side in combination with fixed front/rear IWO thickness.

and the x and y axis regard the thickness of MgF_2 on the front and rear side, respectively.

As illustrated in Figure 4.3, the highest $J_{\text{implied-bifi}}$ increases with the increasing of IWO thickness for both bilayer and trilayer types of (*n*)-contacts. When using 10-nm thick IWO, MgF_2 layers of 110 nm (front) and 120 nm (rear) are needed to maximize the $J_{\text{implied-bifi}}$ of the bifacial solar cells, reaching a value of 47.8 mA/cm^2 as shown in Figure 4.3a and 4.3b. The lower maximum $J_{\text{implied-bifi}}$ of cells with 10-nm thick IWO as compared to those with 50-nm thick IWO is due to higher reflectance. Measured reflectance of bifacial solar cells is presented in Figure B.4. Based on simulation results, we fabricated solar cells with varying IWO front/rear thickness (10 nm through 50 nm) and correspondingly optimized MgF_2 layers on both sides.

It is noticeable that the thickness of MgF_2 layer on the front side dominates the current contribution to the bifacial device, so thickness of MgF_2 layer on front side should be carefully optimized. As shown in Figure 4.3, there is much more tolerance in the rear side MgF_2 and IWO use.

4.3.4. Ultra-thin IWO layers for bifacial silicon heterojunction solar cells

The external parameters of bifacial solar cells with bilayer *n*-type stack are reported in Figure 4.4a. The V_{OC} of the cells increases with the increase of IWO thickness. A similar trend is found also for J_{SC}, *FF* and η. The TCO in SHJ solar cells serves a dual purpose. It does not only function as anti-reflection coating for optical purpose but also facilitates lateral transport for carriers [147, 267]. IWO is a *n*-type material, so it might also provide field effect passivation in solar cells [295]. Consequently, increasing IWO thickness may potentially enhance V_{OC}, J_{SC}, *FF* and η. However, the *FF* measured when illuminating the device through the *N*-side is slightly higher than the values measured from the *P*-

side, demonstrating once more that the carrier transport property of the *N*-side is better than that of the *P*-side [239]. The higher J_{SC} measured from *P*-side can be attributed to better transparency of MoO_x [102]. It is worth noting that the J_{SC} varied with different IWO-thickness, consistently with optical simulation results. Thicker IWO provided better light response. Nevertheless, a decrease in J_{SC} was observed at 50-nm thick IWO samples. According to the external quantum efficiency (EQE) measurement as shown in Figure B.5, we assume this is due to the insufficient MgF_2 thickness on the rear side.

The external parameters of bifacial solar cells with trilayer *n*-type stack are plotted in Figure 4.4b. *FF* and η have the same trends as the case for bilayer stack samples. The resistivity and sheet resistance of IWO across various thicknesses are presented in Figure B.6, where a consistent trend with *FF* is observed. Consequently, the variations in *FF* across different IWO thicknesses can be attributed to changes in resistivity and sheet resistance. The lower V_{OC} values measured in this series are most probably caused by different passivation qualities of the cell precursors. The enhancement of V_{OC} in 50 nm case could be ascribed to the higher lifetime of the cell precursor as provided in Figure B.7. The passivation quality of trilayer samples is generally lower than that of the bilayer stack samples. This could be linked to a less conductive *n*-layer close to the c-Si/(*i*)a-Si:H interface due to the use of less conductive nc-SiO_x:H layer; therefore, field-effect passivation or the band bending is less efficient. The deposition condition of trilayer is more aggressive compared to that of bilayer and monolayer samples. As in the bilayer-stack case, here we also note a decrease of J_{SC} value for 30 and 50-nm thick IWO, due to the insufficient MgF_2 thickness.

When comparing the *N*-side-J_{SC} between the two *n*-contact, it was observed that the trilayer-stack had a better light response, showing an average gain of 0.3 mA/cm^2 as compared to cells with the bilayer-stack. This gain might be attributed to reduced reflected light as shown in Figure B.4. However, as previously mentioned, mainly due to the rather thick stack ($\sim$ 10 nm) and the less favorable electrical properties of (*n*)nc-SiO_x:H, the samples with trilayer-stack exhibit lower *FF* as compared to those with bilayer *n*-type stack.

The optical simulation and experimental results exhibited a strong correlation. The J_{SC} increased with thicker IWO layer. It was observed that even with a thickness of only 10 nm for IWO, a decent J_{SC} can be maintained. However, the *FF* of the device with 10-nm thick IWO was found to be below 78%, which can be attributed to the high contact resistivity as illustrated in Figure 4.2 (c) and as well as in reference [281].

The φ of the devices is shown in Figure 4.4c and 4.4d. Solar cells with trilayer *n*-type stack exhibit the best average bifaciality factor of 0.99, while the bifaciality factor of cells with bilayer *n*-type stack is around 0.96. This difference was mainly caused by a larger variation in J_{SC} when illuminated from *N*-side due to the better light response of trilayer stack comparing to bilayer stack. The champion cell with bilayer *n*-type stack exhibits 23.25% conversion efficiency when measured from the *P*-side (V_{OC} = 716 mV, J_{SC} = 39.74 mA/cm^2, *FF* = 81.7%) and 22.75% efficiency from the *N*-side (V_{OC} = 716 mV, J_{SC} = 38.87 mA/cm^2, *FF* = 81.9%). Figure 4.5 shows the independently certified efficiencies of our best performing solar cell.

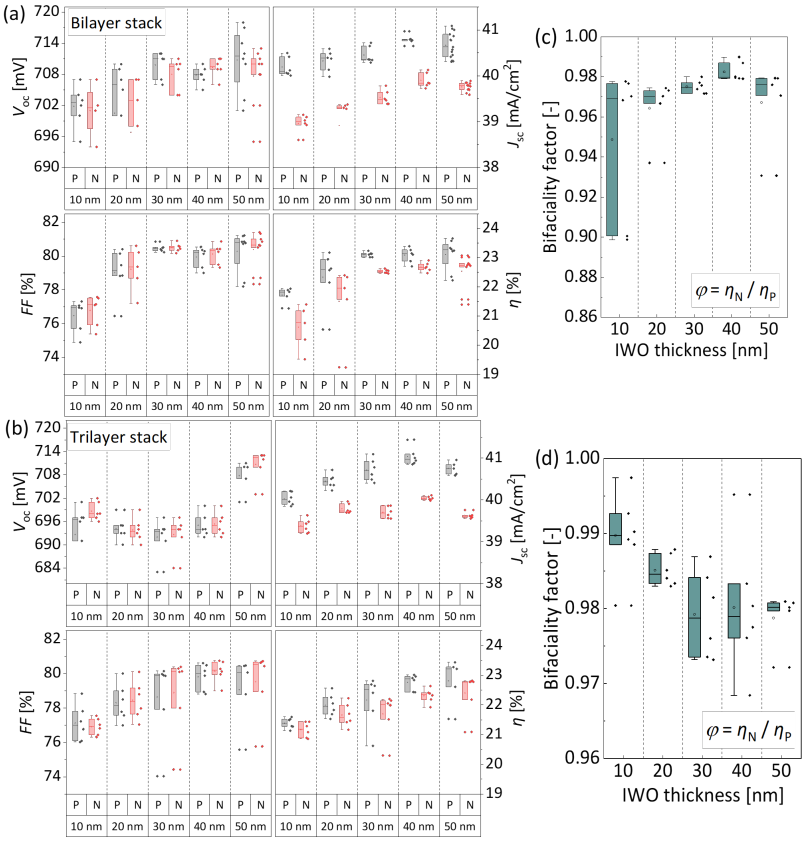

Figure 4.4: (a) cells exhibit bilayer *n*-contact and (b) cells exhibit trilayer *n*-contact are measured by illuminating either the MoO_x layer or the *n*-contact side corresponding to *P*-side and *N*-side, respectively (the gray and red bars indicate the data measured from the *P*-side and the *N*-side of the bifacial cells, respectively). The conversion efficiencies at *N*-side and *P*-side illuminations are used to calculate the bifaciality factor of bifacial cells with (c) bilayer or (d) trilayer *n*-contact.

4.4. Conclusion

This study aims to reduce TCO consumption by minimizing TCO thickness in bifacial solar cells while preserving high solar cell performance. Our study investigated the impact of different *n*-contacts and various thicknesses of IWO films on the performance of bifacial solar cells. We found that bilayer and trilayer stack exhibited higher efficiency compared to monolayer stack mainly due to better (i) electronic properties of bilayer stack and (ii) optical properties of trilayer stack. The optical simulation demonstrates that the integration of thinner IWO layers into bifacial solar cells combined with bilayer and trilayer stack yields a promising enhancement in light response. Even with only 10-nm thick IWO, the cells achieve J_{SC} over 40 mA/cm^2. Additionally, by symmetrically applying IWO and MgF_2 layers on both sides of the solar cells and reducing the thickness to 10 nm, we achieved certified conversion efficiencies of 21.66% and 20.66% when measured

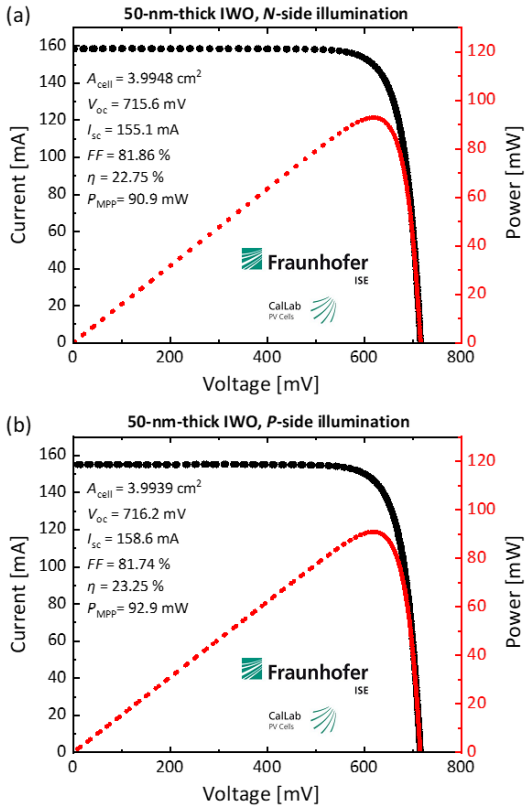

Figure 4.5: (a) and (b) certified power conversion efficiency for 50-nm thick IWO cells from *N* and *P* side, respectively.

from the MoO_x and n-contact side, respectively, with J_{SC} and *FF* values remaining above 40 mA/cm^2 and 77%. In this way, a reduction of 90% in the usage of IWO compared to monofacial SHJ solar cells was demonstrated. The certified results are shown in Figure B.8. For 50-nm thick IWO samples, the champion device within a bilayer-stack achieves certified conversion efficiencies of 23.25% and 22.75% when characterized from the MoO_x side and the *n*-layer side, respectively, with a bifaciality factor of 0.98. In general, a bilayer stack can result in a bifaciality factor above 0.96, which can be further enhanced to 0.99 by switching to a trilayer stack. These findings demonstrate the potential of bilayer and trilayer stack with IWO films as promising candidates for high-performance bifacial solar cells sporting more than 90% reduction in usage of TCO.

5

Universal interface engineering method for applying TMO in SHJ solar cell

This chapter was published in *Solar Energy Materials and Solar Cells* * [103]

Abstract

Transition metal oxide (TMO) thin films exhibit large bandgap and hold great potential for enhancing the performance of silicon heterojunction (SHJ) solar cells by increasing the short-circuit current density significantly. On the other hand, achieving precise control over the electrical properties of TMO layers is crucial for optimizing their function as efficient carrier-selective layer. This study demonstrates a general and feasible approach for manipulating the quality of several TMO films, aimed at enhancing their applicability in silicon heterojunction (SHJ) solar cells. The core of our method involves precise engineering of the interface between the TMO film and the underlying hydrogenated intrinsic amorphous silicon passivation layer by managing the reaction of the TMO on the surface. X-ray photoelectron spectroscopy spectra demonstrate that our methods can modify the oxygen content in TMO films, thereby adjusting their electronic properties. By applying this method, we have successfully fabricated WO_x-based SHJ solar cells with 23.30% conversion efficiency and V_2O_x-based SHJ solar cells with 22.04% conversion efficiency, while keeping *n*-type silicon-based electron-transport layer at the rear side. This research paves the way for extending such interface engineering methods to other TMO materials used as hole-transport layers in SHJ solar cells.

*Cao, L., Procel, P., Zhao, Y., Yan, J., Özkol, E., Kovačević, K., Zeman, M., Mazzarella, L. and Isabella, O. (2024). Universal method for applying transition metal oxides in silicon heterojunction solar cell. Solar Energy Materials and Solar Cells, 278 (2024): 113170. https://doi.org/10.1016/j.solmat.2024.113170.

5.1. Introduction

The photovoltaic industry is predominantly powered by crystalline silicon-based solar cells, with silicon heterojunction (SHJ) solar cells achieving world-record conversion efficiency [55]. In the quest for even higher efficiency and more cost-effective production, researchers are exploring novel materials whose optical and electrical properties are comparable or superior to the traditional boron- and phosphorus-doped silicon-based thin films [61]. Such materials, also known as dopant-free materials, include organic films [296, 297], metal alkali [73, 298, 299] and transition metal oxides (TMOs) [98, 102, 300–305]. The dopant-free concept is to state that there is no intentional doping in the materials. Dopant-free materials have been successfully integrated into silicon solar cells and have shown promising results. The primary benefit of using dopant-free materials is their low parasitic absorptance which ascribe to their wide band gap [230]. Additionally, their deposition rate is faster than that of *p*-type Si layers [59] and SHJ solar cells can work efficiently with ultrathin TMO materials, unlike *p*-type Si layers that require much thicker films [102]. In recent developments, silicon solar cells featuring dopant-free materials as carrier-selective layer have achieved efficiencies beyond 23% [64, 66, 92]. Meanwhile mainstream front/back-contacted (FBC) SHJ solar cells are based on the rear junction (RJ) structure, implying the deployment of the electron-transport layer (ETL) on the front side [37, 40] and *n*-type bulk c-Si wafer. However, to profit from the enhanced optical performance of TMO materials, a TMO-based hole-transport layer (HTL) is used at the front side of (monofacial) SHJ solar cells, known as the front junction (FJ) structure. We obtain a notable achievement in J_{SC} (40.2 mA/cm^2) resulting in a 23.83% efficiency by integrating an ultra-thin MoO_x as HTL in FJ-SHJ solar cells [102]. Further, substituting traditional Si-based carrier-transport layers with MoO_x for holes and LiF for electrons yielded 21.4% efficiency in FBC architecture [100], which was further increased to 23.61% when integrated into an interdigitated back contact (IBC) architecture [306]. Recently, 22.8% efficiency has been achieved for an FBC RJ-SHJ cell featuring MgO_x/ZnO:Al and V_2O_x as ETL and HTL, respectively [92].

However, the significant potential for improving further cell performance remains unexplored. Simulation results indicate that under optimized conditions, a SHJ solar cell featuring doped silicon-based thin films as charge-transport layers can achieve a conversion efficiency well above 27% [307]. Also using TMOs as charge-transport layers could increase this efficiency to 26.96% [212] or even more than 27% considering the deployment of high resistivity wafers [307]. This advantage is primarily attributed to the wider bandgap of TMO materials, which facilitates an increased J_{SC}. Nonetheless, in experimental scenarios, the peak efficiency achieved is still limited to 23.83% [102]. The thermolytic instability of TMOs presents a significant limitation [105, 120]. Although some tested materials, such as TiN_x, exhibit chemical stability [97], most dopant-free materials tend to be unstable and are adversely affected by neighboring materials [166, 186]. Particularly, in SHJ solar cells, the critical issue involves the reaction between the TMO and the Si-based layers underneath, forming a thin SiO_x film [68, 140, 224, 232]. This interaction results into (i) an additional dielectric barrier for charges to cross and (ii) an uncontrolled decrease of the TMO work function, consequently impairing the electronic performance of the device [120, 164, 167].

Some groups reported on approaches to alleviate the interface reaction of TMOs

which results in higher conversion efficiency. For instance, the use of a pre-annealing step can be applied to reduce the hydrogen content from the intrinsic passivation layer, alleviating the reaction between MoO_x and the passivation layer [123]. Notably, inserting a less reactive layer is another solution. Li *et al.* show that the efficiency can be improved by inserting a CrO_x buffer layer to protect MoO_x [308]. Tong *et al.* apply a pre-growth SiO_x thin film to prevent the reaction between MoO_x and the substrate [167]. Multilayer structure including $Al_yTiO_x/Ti_yZnO_x/TiO_x/ZnO$ builds up resilience against moisture and therefore improves the stability of TiO_x-based electron-selective contact [309]. Other works apply thicker TMO (V_2O_x and WO_x) films to realize an appropriate high work function, but as a downside effect the resistivity of the TMO films increased significantly resulting in poorer electronic performance of the device [60, 310, 311]. Finally, in our previous work we proposed a plasma treatment with or without boron (PTB or PT) before the deposition of MoO_x. These treatments have been proven to not be harsh against (*i*)a-Si:H [225]. The boron atoms may act as a catalyst to form a favourable interface layer improving the electronic property of devices. These methods improve the efficiency significantly in both monofacial [102, 225] and bifacial SHJ solar cells [50].

This contribution aims at showing the applicability of our plasma treatment method to other TMO materials, namely WO_x and V_2O_x, to act as HTLs in SHJ solar cells. Initially, we measure the oxygen content of the TMO films under different interface engineering methods (noPT, PT and PTB). Subsequently, we study the impact of those methods on the performance of SHJ solar cells as function of WO_x and V_2O_x thicknesses. We ultimately showcase high-efficiency FJ-SHJ solar cells (23.30% and 22.04%) integrating 2-nm thick WO_x and 3-nm thick V_2O_x films, respectively, and *n*-type Si-based ETL.

5.2. Experimental methods

Figure 5.1 presents the structure of TMO-based FJ-SHJ solar cells. These samples were fabricated using <100> *n*-type, double-side polished, 4-inch float-zone (FZ) wafers. The wafers exhibited a thickness of 280 ± 20 µm and a resistivity of 3 ± 2 Ω·cm. For texturing, the wafers were processed in a tetramethylammonium hydroxide (TMAH) solution, with ALKA-TEX serving as an additive. The cleaning process entailed a wet chemical treatment, followed by immersion in a 0.55% hydrogen fluoride (HF) solution for 5 minutes. Subsequently, the wafers were placed into a plasma-enhanced chemical vapor deposition (PECVD) system for the deposition of thin-film layers. The (*i*)a-Si:H/(*n*)a-Si:H stack at the rear side was kept constant across all solar cells involved in this study [236, 237]. We used 7-nm thick and 5-nm thick (*i*)a-Si:H on the front and rear side, respectively. The (*n*)a-Si:H on the rear side was 4-nm thick. Subsequently, the deposition of the (*i*)a-Si:H and the application of different plasma treatment methods were performed on the front side. These methods were processed in the PECVD chamber. Three methods were tested namely, noPT (no treatment), PT (plasma treatment) and PTB (plasma treatment with boron), which used a gas mixture comprising SiH_4, H_2, CO_2, and B_2H_6, as provided in Table C.1. For detailed information on the interface engineering process, readers are referred to our previous work [102, 225]. Then, TMO thin films (WO_x and V_2O_x) were thermally evaporated under a vacuum pressure of 5×10^{-6} mbar with thicknesses of 1, 2, 3, 4, and 5 nm. The deposition rate of both TMOs was 0.1 nm/s. The substrate rotated at the speed of 10 rpm. For comparative analysis, a reference FJ-SHJ solar cell featuring a *p*-type

Si layer at the front side was also included; more experimental details about that can be found elsewhere [58]. Following the TMO deposition, layers of optimized tungsten-doped indium oxide (IWO) were sputtered onto both the front and rear sides, with thicknesses of 50 nm and 150 nm, respectively [239]. A hard mask was employed to define six 2×2 cm^2 solar cells on each wafer during the IWO deposition process. The samples were annealed at 180 °C for 5 min to recover from the sputtering damage. Following this step, a 100-nm thick layer of silver was sputtered onto the front side, which was then followed by copper plating to establish the metallic contact grid [240, 241]. The fingers were 15-µm wide with a pitch of 915 µm. 500 nm of silver was sputtered as the rear metal electrode. Subsequently, the front side was coated with a 110-nm thick layer of MgF_2, serving - together with the front IWO - as a double antireflection coating. The specified thicknesses were derived using a nominal calculation, modified by a geometrical factor of 1.7 to consider the lower deposition rate on textured surface [242].

The effective minority carrier lifetime was measured after each step of the fabrication process using a Sinton WCT-120. To evaluate the current-voltage (J-V) performance under standard test conditions an AAA rated Wacom WXS-90S-L2 solar simulator was utilized. Additionally, in-house external quantum efficiency (EQE) equipment was used to measure $J_{SC,EQE}$. The absorptance spectra were measured on TMO layers deposited on Corning glass using a PerkinElmer Lambda 1050 system. The sketch of the samples for absorbance measurement is shown in Figure C.1. Spectral response analyses were conducted on dedicated cells on the same wafer as other solar cells but without the front metal grid. For the compositional analysis of the TMO layers, we employed a ThermoFisher Kα X-ray photoelectron spectrometer (XPS) [244, 312], utilizing an Al Kα X-ray source (1486.68 eV) within a chamber maintaining a base pressure of 2×10^{-9} mbar. These measurements were executed at room temperature following the attainment of a high vacuum. Notably, the XPS sample prepared with identical processes depicted in Figure C.2, using 280 ± 20 µm flat <111> n-type float-zone (FZ) wafers to replicate the surface orientation of the pyramid facets observed in solar cells, with deposition times adjusted to align the thicknesses with those of textured samples.

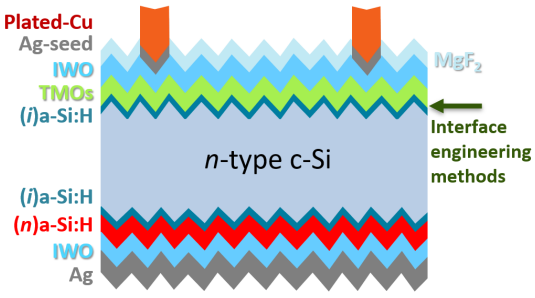

Figure 5.1: Cross-sectional sketch of a TMO-based FJ-SHJ solar cell.

5.3. Result and discussion

5.3.1. Control the oxygen content of WO_x and V_2O_x

TMOs exhibit similar properties, particularly where oxygen content influences their work function [166]. Drawing from observations in prior research [69, 80, 102, 120, 225, 313, 314], we speculate that the influence observed in other TMO materials, such as MoO_x, would similarly affect WO_x and V_2O_x. To demonstrate our speculation, we conduct XPS analyses to explore the oxygen vacancies in these films. The high-resolution spectra and the full XPS survey spectra of W and V are reported in Figure C.3 and C.4, respectively. Additionally, the boron atoms have not been detected through XPS high resolution scan as shown in Figure C.5. For our experiments, we use films with thicknesses of 2 nm for WO_x and 3 nm for V_2O_x. These thickness values were chosen based on our previous study, where we achieved a champion device with 2 nm MoO_x [102]. The corresponding valence band spectra are plotted in Figure 5.2. The shoulder peaks noticeable between 1 eV and 2 eV in the valence band spectra of WO_x and V_2O_x indicate the presence of defects in the films. The observed defects stem from the TMOs' instability, leading to interface reactions between (*i*)a-Si:H and the TMOs, which result in the formation of a thin SiO_x film [102]. This process extracts oxygen from TMO molecules, creating oxygen vacancies in the material and thereby changing their work function [225].

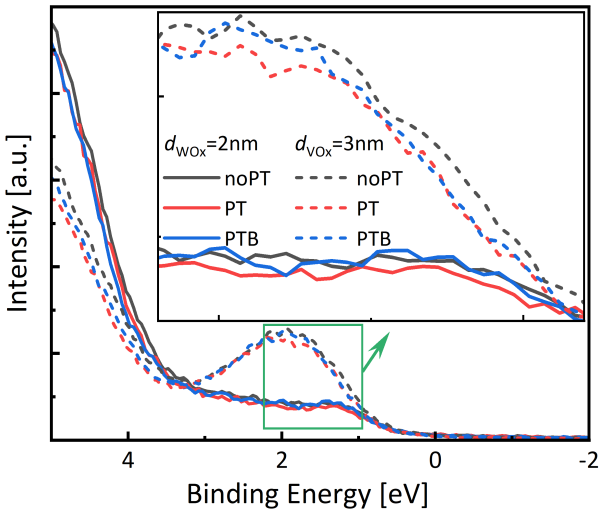

Figure 5.2: Valence band spectra of as-deposited 2-nm thick WO_x and 3-nm thick V_2O_x films deposited after noPT, PTB and PT methods. The inset shows a zoomed view of the spectra between 1 eV and 2 eV binding energy.

Valence band spectra as provided in Figure 5.2 reveal that V_2O_x-films exhibit higher peak heights compared to WO_x, suggesting that V_2O_x contains a larger number of defects, i.e. oxygen vacancies. This phenomenon can be attributed to the fact that the binding energy of the W-O bond (> 5.0 eV) [315] exceeds that of the V-O bond (~ 4.3 eV) [316]. Consequently, the V-O bond is weaker resulting in easier oxygen reactions with the substrate. Defects within TMO films present a dual-edged sword. On the one hand, these

defects significantly impact the electronic properties of the device. On the other hand, these vacancies endow the films with semiconductor properties, specifically facilitating carrier-selective layer [317, 318]. Nonetheless, an overabundance of oxygen vacancies may impair carrier transport efficiency [314]. Therefore, it is crucial to identify a TMO material that establishes a balance between the quantity of oxygen vacancies and its capacity for selective transport.

To elaborate further, within each category of TMOs, the distinctions in oxygen vacancies may initially appear subtle as shown in Figure 5.2. However, upon closer examination at an enlarged scale in Figure 5.2, it becomes evident that the PT method results in fewer oxygen vacancies within the films followed by PTB and noPT cases. To substantiate these observations, we report the oxygen content within these films extracted from the XPS survey spectra. The tungsten, vanadium and oxygen content of the films expressed in percentage are presented in Figure 5.3a and 5.3b, offering quantitative insights into the variations of oxygen content across different methods. We observe that interface engineering methods significantly affect the oxygen ratio within the films. Specifically, for both WO_x and V_2O_x films, the PT samples exhibit the highest oxygen concentrations. The presence of increased oxygen concentrations in the films correlates with fewer oxygen vacancies, aligning with the insights obtained from the valence band spectra analysis discussed above in Figure 5.2.

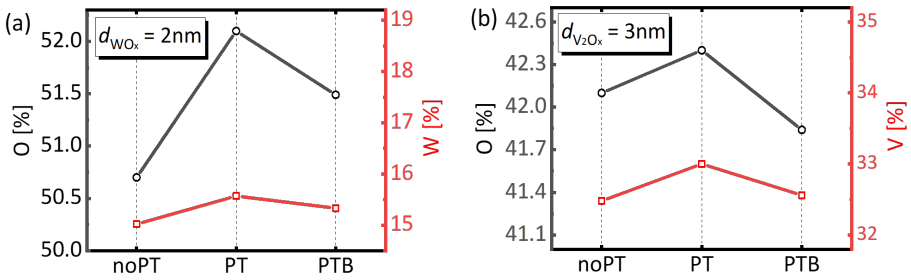

Figure 5.3: (a) W and O content, (b) V and O content under different interface engineering methods calculated from XPS spectra (see Figure C.3 and C.4).

5.3.2. Performance of WO_x-based SHJ solar cells

The efficiency of carriers transport within TMO materials is critically dependent on their work function [319], which is influenced by the internal oxygen content [120]. Moreover, the thickness of the film plays a crucial role in determining this oxygen content [102, 320, 321]. To understand these dynamics, we have examined the effects of film thickness and interface engineering methods on solar cell performance. Figure 5.4 shows the external parameters derived from the J-V curve of solar cells with variable WO_x thicknesses and noPT, PT and PTB methods.

For the devices with noPT as shown in Figure 5.4a-d, we observe that V_{OC} drops with thicker WO_x films. It is important to mention that the 2-nm samples exhibited a significant decline in performance, which can be attributed to the reduced minority carrier lifetime (τ) of the cell precursor as shown in Figure C.6. The τ measured after the deposition of

WO_x dropped more than half of the τ measured after the PECVD process. The drop may be attributed to the reaction between WO_x and the passivation layer deposited by PECVD. The higher V_{OC} measured for the 1-nm thick WO_x might be explained by the higher initial passivation quality (higher τ, see Figure C.6) for this specific precursor. For the fill factor (*FF*) we observe a linear increase from 65% up to 78% for a WO_x thickness from 1 to 4 nm. For 5-nm thick WO_x the FF drops to 70%. This trend suggests a critical balance between WO_x-thickness and *FF*, identifying 4 nm as the optimal thickness. The J_{SC} decreases as the WO_x thickness increases. The absorbance data, shown in Figure C.7a, indicate that WO_x layers absorb short-wavelength light more effectively, with increased absorptance in thicker layers. For the 5-nm thick sample, the rise in J_{SC} might be attributed to optimal combination of antireflection coating. The conversion efficiency (η) is mostly dominated by the *FF* trend with the highest η of 21.29% measured for 4-nm thick WO_x film.

For the solar cells fabricated with PT method, we observe an opposite trend with respect to the V_{OC} as provided in Figure 5.4e. V_{OC} increases with thicker WO_x films and arrives at the optimal point at 4 nm with a subsequent decline for 5-nm thick WO_x. During the PT process, thin layers of (*i*)nc-Si:H and (*i*)nc-SiO_x:H are deposited under rather aggressive PECVD conditions, which may degrade passivation quality [58, 102]. Consequently, V_{OC} is lower in the case of 1-nm thick WO_x for PT compared to noPT. With increasing WO_x thickness, there is an enhancement in the work function of WO_x, which contributes to better carrier selectivity at the interface between c-Si and (*i*)a-Si:H [102, 322]. However, the decrease in V_{OC} for samples featuring WO_x thicker than 4 nm can be ascribed to a dipole formation at (*i*)a-Si:H/WO_x, which penalizes V_{OC} and *FF*, similarly to what was observed on samples using MoO_x [102]. Indeed, V_{OC} and *FF* exhibit similar trends as depicted in Figure 5.4e and 5.4f, peaking for an optimal 4-nm thick WO_x layer. This trend, observed also for the noPT case, indicates that the film's work function gets higher for thicker WO_x layers. However, further thickening the WO_x layer to 5 nm caused a decrease in *FF*, highlighting the need to balance the work function and the contact resistivity [66, 102]. Similarly to what was observed for noPT, in Figure 5.4g, the J_{SC} decreases with the increase of WO_x thickness. For the 5-nm thick sample, the observed rise in J_{SC} could be attributed to the optimal combination of antireflection coatings. The η trend aligns with those of V_{OC} and *FF*, with the highest conversion η of 22.27% realized for a 4-nm thick WO_x layer.

Finally, we discuss the impact of PTB, shown in Figure 5.4i-l. V_{OC} remains generally stable but is slightly higher at a thickness of 2 nm. From lowest to higher thickness value, the *FF* slightly increases, reaches the highest value at 3 nm, and decreases with further increased thickness of WO_x. The champion *FF* is over 80%. Compared to noPT and PT cases, the *FF* is improved significantly and shows less dependence on the thickness of WO_x. Similarly to the previous cases, J_{SC} decreases for thicker layers. The optimal η of 23.30% is observed at 2 nm. The trend of η suggests that the working windows of the thickness of WO_x with PTB is wider than the other two methods.

We can conclude that, across different conditions, V_{OC} performance differs depending on the interface engineering method used. The *FF* generally rises for thicker layers before decreasing for the thicker film tested demonstrating a trade-off between work function and contact resistivity. Interestingly the variations of V_{OC} and *FF* are much less impacted by the WO_x thickness for the samples with PTB. This could be due to

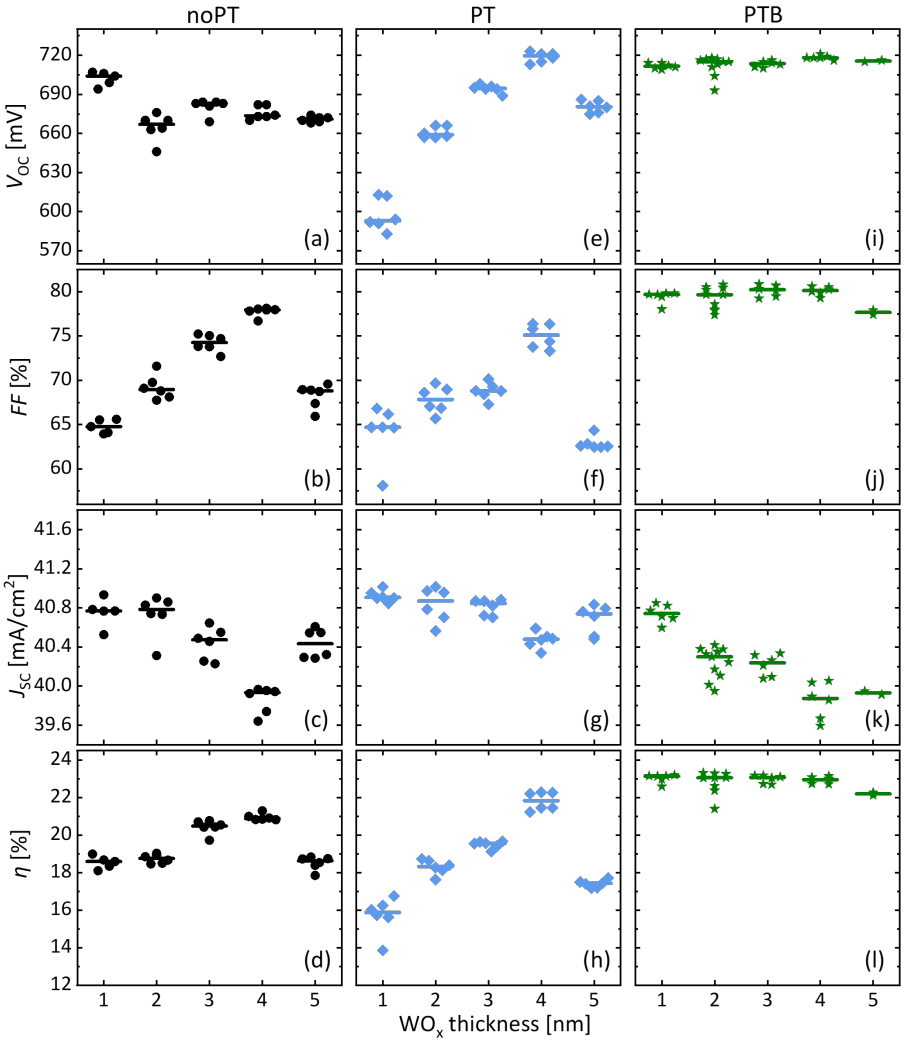

Figure 5.4: The parameters extracted from *J-V* curve of solar cells with different interface engineering methods and WO_x thickness. (a-d) represent the noPT method with black circles; (e-h) represent the PT method with blue diamonds; (i-l) represent the PTB method with green stars. The horizontal lines indicate average values.

the interface becoming less reactive with WO_x after being modified by the PTB method. Generally, J_{SC} decreased as the WO_x film thickness increased because of parasitic absorptance. Still, η follows the trend of *FF*. With PTB and 2-nm thick WO_x, we achieve a champion cell with a conversion efficiency of 23.30%. Similarly to our previous work [102], it is worth noting that no boron atom is detected through XPS measurement for PTB samples. The thinner optimal thickness of WO_x with PTB comes from the optimal interface engineering and achieves a good balance between work function and defects of

the WO_x film. We also present the external quantum efficiency (EQE) and *J-V* curves of the champion WO_x-based and MoO_x-based FJ-SHJ devices [102] in Figure 5.5. Additionally, Figure 5.5 showcases the champion RJ-SHJ solar cell with doped layers from our lab [31]. Remarkably, there is a gain in J_{SC} (indicated by the green area in Figure 5.5a at short wavelengths when using TMOs, attributed to reduced parasitic absorptance on the front side as compared to SHJ solar cells with doped layers.

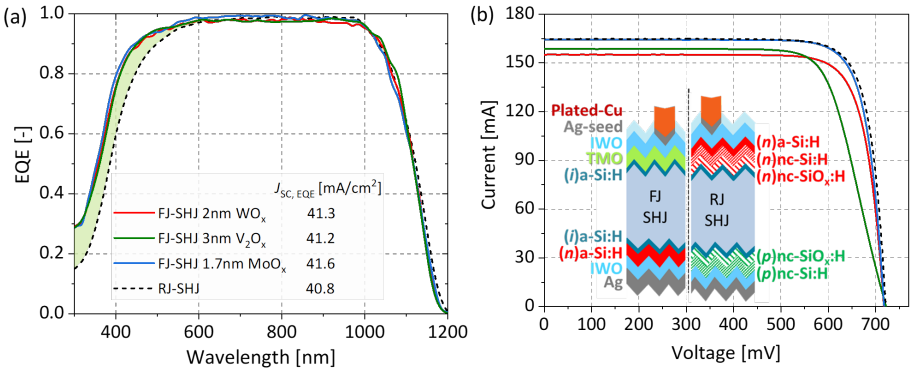

Figure 5.5: (a) EQE and (b) *J-V* curves of champion WOx-based (red), V_2O_x-based (green), MoO_x-based (blue) FJ-SHJ solar cell and RJ-SHJ solar cell with doped layers (black). The green shaded area in (a) represents the photocurrent density gain when switching solar cell structure from RJ-SHJ endowed with silicon transport layers to FJ-SHJ endowed with TMO as HTL. In (b) the detailed layer structure of RJ-SHJ solar cell with doped layers is depicted.

5.3.3. Performance of V_2O_x-based SHJ solar cells

We now examine the impact of V_2O_x-thickness and interface engineering methods on the performance of solar cells, whose parameters, extracted from *J-V* measurements, are plotted in Figure 5.6.

As provided in Figure 5.6a-d, a gradual decrease in V_{OC} with V_2O_x thickness is observed in noPT condition. As previously discussed, TMOs will react with the substrate which is (*i*)a-Si:H in this case, forming a SiO_x layer. This reaction degrades the passivation quality provided by the (*i*)a-Si:H layer. As we observed in WO_x samples with noPT method, we suppose the reaction is related to the thickness of V_2O_x as well. The thicker layer may cause a more significant reaction resulting in lower V_{OC}. The higher V_{OC} at 4 nm case could be attributed to the high lifetime of the precursor as shown in Figure C.8. J_{SC} shows a decline with increased V_2O_x thickness. Figure C.7b provides the absorptance spectra for different thicknesses of V_2O_x. The absorptance of V_2O_x films increases as the film thickness increases. The increase of J_{SC} at 5 nm for noPT samples might be caused by the optimized combination of antireflection coating. The *FF* decreases with V_2O_x thickness, which could be due to increased sheet resistance as the V_2O_x layer gets thicker. η increased slightly and peaked at 4 nm before decreasing at 5 nm.

Like PT-treated WO_x-based SHJ devices, the V_{OC} of V_2O_x samples in Figure 5.6e shows a slight increase with V_2O_x thickness, except for the 2-nm case, peaking at 4 nm and then decreasing at 5 nm. The decrease at 5 nm may be ascribed to thicker V_2O_x film

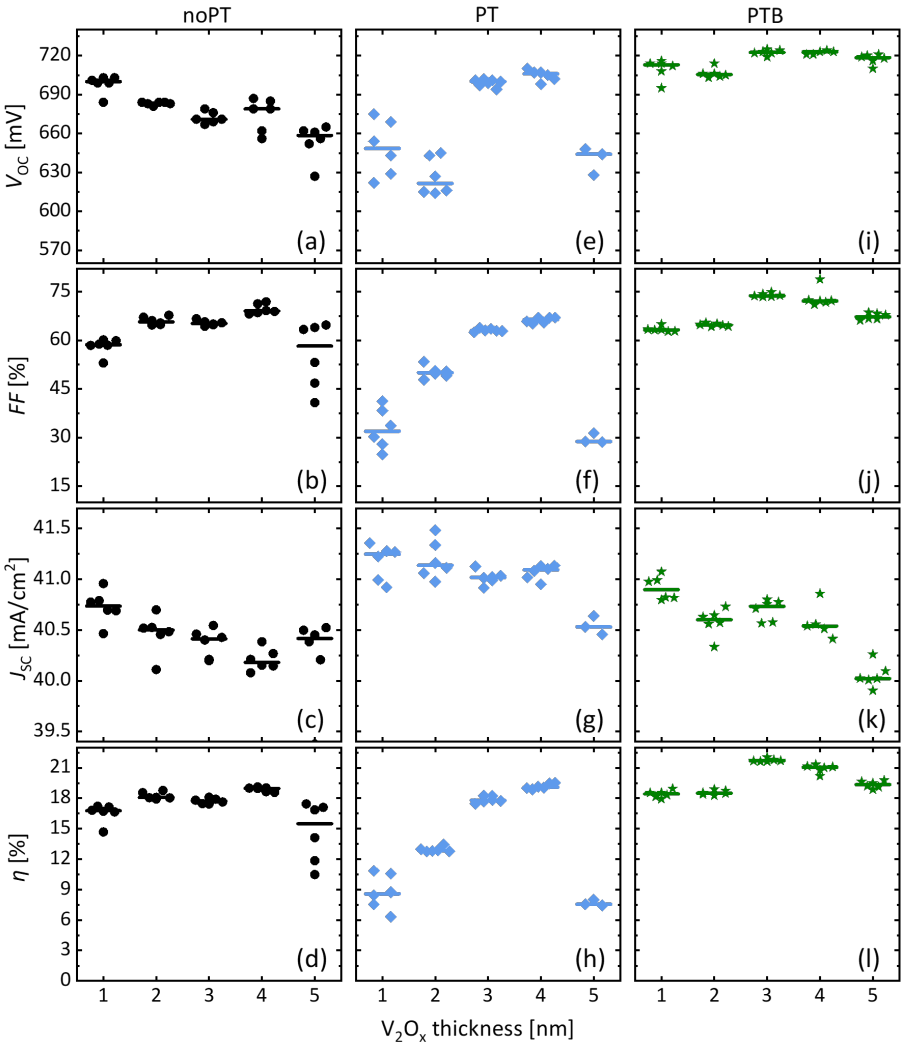

Figure 5.6: The parameters extracted from *J-V* curve of solar cells with different interface engineering methods and V_2O_x thickness. (a-d) represent the noPT method with black circles; (e-h) represent the PT method with blue diamonds; (i-l) represent the PTB method with green stars. The short lines indicate average values.

blocking the carrier transport. In Figure 5.6f, *FF* shows a peak at 4 nm. This phenomenon can be attributed to the same reasoning as in the WO_x case, representing the balance between carrier selectivity and contact resistivity [66, 102]. Additionally, the increase in layer thickness leads to a decrease in J_{SC} due to parasitic absorptance as shown in Figure 5.6g. PT samples show η peak at 4 nm thickness, pointing to an optimal thickness for device performance.

The data of devices manufactured with the PTB method are presented in Figure 5.6i-l.

V_{OC} shows a slight increase with increasing V_2O_x thickness. The interlayer deposited during PTB maintains a good balance between passivation degradation caused by interface reaction and the passivation effect introduced by V_2O_x. J_{SC} decreases with thicker layers. PTB samples achieve their peak *FF* at 3 nm, demonstrating improved control of interface reactions and the electronic properties of the V_2O_x layer. η follows a similar trend to *FF*. The champion cell with η of 22.04%, was obtained for a V_2O_x thickness of 3 nm.

The general trends observed in the parameters of V_2O_x-based cells resemble those of WO_x-based cells, as discussed in Section 3.2. This similarity suggests that the applied methods to different TMOs yield comparable results. At the device level, *FF* is identified as the predominant factor affecting solar cell performance. PTB samples exhibit the highest *FF* at thinner TMO-thickness compared to PT and noPT methods, leading to the champion devices being achieved using the PTB method for both WO_x and V_2O_x cases. Specifically, the η of V_2O_x-based SHJ solar cells is generally lower than that of WO_x-based cells, primarily due to material properties [171, 312]. The weaker V-O bond contributes to more severe interface reactions between V_2O_x and substrate [315, 316]. The reaction generates more defects at the interface which harm the carrier transport. This aligns with our findings from the valence band spectra analysis as provided in Figure 5.2. Additionally, we provide the EQE of the champion V_2O_x-based SHJ solar cells and the SHJ solar cell with doped layers in Figure 5.5. At short wavelengths, a notable J_{SC} gain is observed. This gain (shown by the green shaded area in Figure 5.5a) is achieved with V_2O_x, attributed to reduced parasitic absorptance on the front side compared to SHJ solar cells with doped layers.

5.4. Conclusion

In this work, we utilized different interface engineering methods (noPT, PT and PTB) to alleviate the interface reaction of TMO with the substrate. We investigated the effect of different methods by estimating the TMOs' oxygen content. From XPS survey spectra, we observed that oxygen content in TMO layers deposited after PT is higher than that in TMO layers deposited with PTB and noPT methods. The findings aligned with our previous results and proved the PTB method able to control and create a suitable deposition condition for TMOs, ensuring their suitable work function and oxygen content inside the films. With this observation, further experiments are applied to investigate the impact of TMO-thickness on cell performance regarding different methods. Overall, we applied different methods (noPT, PT and PTB) at the (*i*)a-Si:H/WO_x interface and realized a champion cell with PTB and 2-nm thick WO_x HTL. With 23.30% conversion efficiency and *FF* equal to 80.80%, we push further the performance of WO_x-based SHJ solar cells. Similarly, we modified the (*i*)a-Si:H/V_2O_x interface with the same methods and realized a champion cell with PTB and 3-nm thick V_2O_x HTL, exhibiting 22.04% conversion efficiency and *FF* equal to 74.88%. The champion devices achieved in this work and our previous work are presented in Table 5.1. Our TMO-based FJ-SHJ solar cells' results reveal that the PTB is a method that creates an optimal surface condition for the deposition of TMOs and achieves a desirable equilibrium between the quantity of defects and carrier transport of the film, leading to the enhanced performance of TMO-based SHJ solar cells. We may conclude that PTB has the potential to be extended to other TMO materials serving as HTLs in SHJ solar cells, suggesting a broader applicability of this method in enhancing

device performance. Furthermore, the PTB method is compatible with industrial SHJ production lines.

Table 5.1: TMO-based champion SHJ solar cells

TMO	V_{OC} [mV]	J_{SC} [mA/cm^2]	*FF* [%]	η [%]
MoO_x	721	40.2	82.2	23.83
WO_x	718	40.2	80.8	23.30
V_2O_x	722	40.7	74.9	22.04

6

Conclusions and outlook

6.1. Conclusions

This thesis focuses on integrating TMOs HTL into FJ-SHJ solar cells and developing a universal interface engineering method to replace the traditional doped *p*-type silicon based films to minimize parasitic losses and enhance device performance. Additionally, the application of HTL-TMOs in bifacial SHJ devices presents an opportunity to reduce the consumption of indium-based TCO materials. The main conclusions are summarized as follows.

In Chapter 2, we discussed the working principle of TMOs in SHJ solar cells. The low or high work function of TMOs induces band bending at TMOs/c-Si interface to ensure the carrier selective contact. Then, we introduced the studied TMOs working as ETL and HTL materials. Afterwards, the opto-electrical properties of TMO materials are introduced. We discussed the challenges of applying TMOs in SHJ solar cells, such as the thermodynamic instability of TMOs resulting in interface reaction once they contact with a substrate, for instance c-Si. The thin SiO_x which is formed after the interface reaction will limit the device performance. Several attempts have been tested to alleviate the interface reaction. At the same time, diverse deposition technologies have been tested to develop TMO thin-films. The architecture of SHJ solar cells integrated TMOs is introduced. To fully exploit the optical advantage of HTL-TMOs, the SHJ solar cells may better designed with FJ architecture.

In Chapter 3, we highlight the world record conversion efficiency achieved by MoO_x based SHJ solar cells. The breakthrough resulted from the strategic optimization of the interface between the MoO_x layer and the (*i*)a-Si:H passivation layer. This study highlights the importance of controlling the electrical properties of the MoO_x layer to enhance its performance as a hole collector. This study identifies the dipole layer at the MoO_x/(*i*)a-Si:H interface with the help of *ab initio* modeling and proposes a method to minimize it. This optimizes the work function variation of MoO_x as thin-film grows, which is critical for high performance hole transport. An experimental method based on plasma treatment, is used to control the oxygen content in the MoO_x layer, which is essential

to maintain its optimal electrical performance. Such process acts as a barrier to oxygen diffusion, resulting in a high-quality, ultra-thin MoO_x layer, which significantly increases the efficiency of solar cells. These findings not only show significant improvements in conversion efficiency, but also highlight the compatibility of these advanced processes with industrial SHJ production lines to facilitate future improvements in photovoltaic technology.

In Chapter 4, the study on indium reduction in bifacial silicon heterojunction (SHJ) solar cells with MoO_x hole collectors reveals several critical findings for optimizing solar cell performance while minimizing the use of indium in TCO layers. Initially, bifacial SHJ cells with different *n*-contact layers — monolayer ((*n*)a-Si:H), bilayer ((*n*)nc-Si:H/(*n*)a-Si:H), and trilayer ((*n*)nc-SiO_x:H/(*n*)nc-Si :H/a-Si:H) — were tested, showing that bilayer and trilayer configurations outperform monolayer in terms of both electronic and optical properties. The optical simulations guided the development of solar cells featuring ultra-thin IWO layers, which, when paired with MgF_2 to form a DLARC, demonstrated significant reductions in TCO usage. Remarkably, solar cells with 10-nm thick IWO layers achieved J_{SC} exceeding 40 mA/cm^2 and $FF > 77\%$, representing a 90% reduction in TCO compared to conventional cells. The bifacial cells with bilayer *n*-contacts reached conversion efficiencies of 23.25% and 22.75% from the MoO_x and *n*-contact sides, respectively, with a bifaciality factor of 0.98, further enhancing the performance by using trilayer stacks. These advancements highlight the potential of bilayer and trilayer stacks with IWO films to significantly reduce indium consumption while maintaining high-efficiency solar cell performance.

In Chapter 5, a universal and effective method to improve the performance of SHJ solar cells by using TMO as the hole transport layer. This study demonstrates a precise interface engineering method for modifying the TMO/(*i*)a-Si:H interface to better control the electrical properties of the TMO layer. By applying this method, we adjusted the oxygen content which was measured by XPS in the TMO film to optimize its electronic properties. The oxygen content is critical for its function as a highly efficient hole transport layer. With this method, we succeeded in manufacturing SHJ solar cells with a conversion efficiency of 23.30%, using WO_x. When using V_2O_x, the conversion efficiency is 22.04%. The results shows the effectiveness of the interface engineering method. More importantly, the method has the potential to be applied on other TMO materials and improve the performance of TMO-based devices.

6.2. Outlook

Throughout the writing of this thesis, many ideas arose. The following suggestions could guide the future development in this research area:

1. Fully TMO-based SHJ solar cells

(i). Same TMO material as HTL and ETL integrated in SHJ solar cells

As we have already discussed in Chapter 3 and Chapter 5, TMO materials exhibit similar properties. TMOs tend to react with the materials they contact [166]. This reaction changes the electronic properties of TMOs, with the most significant issue being the degradation of their work function. We normally regard this issue as a limitation of TMOs in SHJ devices. TMOs can be used as HTLs because of their high work function. Thus, any uncertainty in the work function drop can harm solar cell performance by decreasing the

FF, and previous research has focused on finding suitable ways to alleviate the interface reaction between TMOs and Si-based substrates (either bulk or thin films). However, reconsidering the situation, we might see it differently. HTL materials require TMOs with a high work function, whereas ETLs require TMOs with a low work function as discussed in Chapter 2 Section 2.2. If we can control the work function of TMO materials, it may be possible to fabricate SHJ solar cells using the same TMOs as both ETL and HTL. The device structure is shown in Figure 6.1a.

Matsui *et al.* reported that ALD-TiO_x films have the potential to function as both ETL and HTL [323]. Their findings show that these layers can be tailored to be either electron or hole selective based on deposition conditions. Different precursors were used for ETL-TiO_x and HTL-TiO_x films. The post-deposition treatments and the work function of the metal electrode might also influence the electronic property of TiO_x film. The study indicates that carrier selectivity is associated with the induced band bending in the c-Si absorber, driven by the effective work function difference at the Si/TiO_x interface and the negative fixed charge within the TiO_x layer [324]. Therefore, if we can find a suitable treatment to adjust the work function of MoO_x or WO_x [325], it will be possible to fabricate SHJ devices using the same TMO. Another option is to choose a TMO material with a medium work function (lower than WO_x but higher than TiO_x) making the adjustment of the work function easier to achieve.

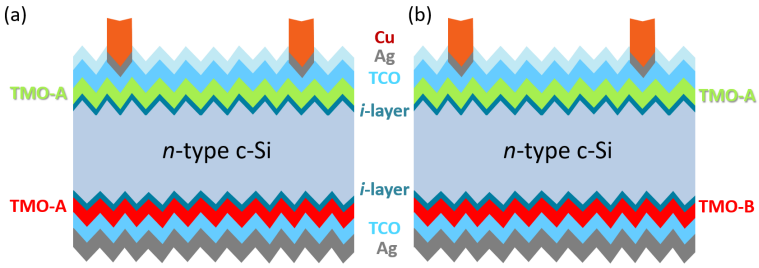

Figure 6.1: Cross-sectional sketches of fully TMO-based FJ-SHJ solar cells: (a) same TMO materials as HTL and ETL; (b) different TMO material as HTL and ETL.

(ii). Different TMO material as HTL and ETL integrated in SHJ solar cells

Double-side dopant-free materials integrated in SHJ solar cells have been studied. The sketch of SHJ solar cells within dopant-free materials is presented in Figure 6.1B. Impressive conversion efficiency above 23% has been achieved by applying HTL- and ETL-TMO in a novel architecture silicon solar cells [64]. The findings indicate that the potential of TMO materials achieving high efficient solar cells. with the optimized interface engineering method, we may able to further improve the conversion efficiency. Due to the applicability of the method, it is possible to realize large-scale, low-cost solar cell industrial production.

2. Towards TCO-free structure TMO based SHJ solar cells

TCO-free SHJ solar cells is a ideal configuration aim to reduce the indium based TCO and realize sustainable, high-efficiency and cost-effective PV technology [46]. Recent studies have demonstrated the potential for realizing high-efficiency SHJ solar cells without the use of TCO layers.

Researchers have explored alternative materials and treatments to replace TCOs in monofacial SHJ solar cells. Research has shown that over 22% efficiency can be achieved by employing lateral conduction in crystalline silicon absorbers and ozone treatments at the amorphous silicon/metal interface. This method improved passivation, suppressed metal diffusion, and lowered contact resistivity [270]. An investigation into aluminum-doped zinc oxide (AZO) as a front electrode resulted in an efficiency of 23.6% with low contact resistivity. The study demonstrates the potential of indium-free alternatives for achieving high efficiency in SHJ cells [264]. Another study introduced a TCO-free and dopant-free asymmetric structure using alkali fluoride/aluminum electron-selective contacts and TMO/silver hole-selective contacts. This combination decreased charge carrier recombination and achieved a power conversion efficiency of 22.9% [271].

We have achieved promising result based on bifacial SHJ solar cells with reduced TCO thickness. In our group, using tin-, fluorine-, and tungsten-doped indium oxide with optimal thickness, we have achieved efficiencies above 22%. These innovations demonstrate significant potential for reducing material consumption while maintaining high efficiency [48]. As demonstrated in Chapter 4, it is possible to achieve over 22% efficiency with 10-nm thick IWO on both sides of bifacial SHJ solar cells. In this scenario, we still use a phosphorus-doped silicon-based *n*-contact layer [50]. If we replace the traditional *n*-layer with ETL-TMO materials, it is possible to achieve highly efficient, TCO-free bifacial SHJ solar cells using HTL-TMO and ETL-TMO.

3. TMO materials in tandem SHJ

TMOs as promising carrier transport layers have been studied for high-efficiency and stable perovskite solar cells (PSCs). Their tunable electronic properties have attracted researchers to investigate their applicability. Several TMO materials have been successfully applied in PSCs and improved the conversion efficiency and long-term stability.

V_2O_x has proven to be an effective *p*-type contact material that enables high-quality perovskite films with significant efficiency. Its high transmittance and potential to achieve high efficiency make it worth to apply the PSC architecture [326]. NiO_x is another TMO that has been successfully used as an HTL to improve the efficiency and stability of PSCs. Devices containing the NiO_x layer have demonstrated significant resistance to degradation, which is critical for long-term performance [327]. A simple solution-based method has been developed to fabricate indium-doped TiO_x ETL. Indium doping enhances conductivity and band arrangement at the ETL/perovskite interface, resulting in a steady-state efficiency of up to 19.3% for PSCs. In addition, the steady-state efficiency of the four-terminal perovskite-silicon tandem cell reaches 24.5%. [328]. The integration of TMO materials in PSCs significantly improves their efficiency and stability.

SHJ-based two terminal (2-T) perovskite tandem solar cell is an advanced architecture as high-efficiency solar cell [329]. The combination of perovskite materials exhibit excellent opto-electronic properties with the well-established silicon technology, these tandem devices are able to exceed the efficiency limits of traditional single-junction silicon solar cells [330]. This simplified architecture provides a low-cost, high-performance device for next-generation photovoltaics.

In 2-T structure, there is a layer as recombination layer between perovskite and SHJ. The recombination layer in SHJ/perovskite tandem solar cells is important for efficient charge carrier transfer and device performance [331]. Recent research has proved that

several materials and approaches could significantly enhance the efficiency and stability of tandem devices [332].

ITO is popular for recombination layers due to its high transparency and low resistivity [333]. Nanocrystalline silicon film applied as recombination junctions enhances light management and electrical performance in SHJ/perovskite tandem cells. It has achieved a V_{OC} of over 1.8 V and a PCE of 21.4% [334]. Organic recombination layers has achieved a V_{OC} of 1.96 V and an efficiency of 25.9%. The results indicate its potential to enhance performance of tandem solar cells [335]. Molecular-level interface engineering has also shown great potential in optimizing recombination layers. A hybrid hole transport layer combining NiO_x with 2PACz molecules helped uniform deposition and minimized shunt losses. This innovation led to a certified efficiency of 28.84% in fully textured SHJ/perovskite tandem cells[336].

Several works have been published where the same TMO material is proposed as both an ETL and an HTL. WO_x is commonly used as an ETL in perovskite solar cells due to its high electron mobility and conductivity, which enhance electron extraction while blocking holes [325, 337, 338]. Conversely, in silicon solar cells, WO_x is typically used as an HTL because of its high WF [159, 300]. TiO_x is another material commonly employed as an ETL in silicon and perovskite solar cells [150, 328, 339]. By modifying its properties, TiO_x can also serve as an HTL in SHJ solar cells [323, 340]. High WF HTLs like MoO_x, V_2O_x, and WO_x can form RJ in SHJ solar cells by enabling B2B or TAT tunneling at the c-Si/HTL or (*i*)a-Si:H/HTL interface. These materials naturally create RJ when deposited on c-Si or (*i*)a-Si:H. Meanwhile, they provide efficient charge recombination [341]. Additionally, the ETL of the top cell can be directly deposited on them. For instance, in organic tandem device, the ETL of the top cell can directly deposit on MoO_x. In this case, the RJ is formed at the ETL/HTL interface [342].

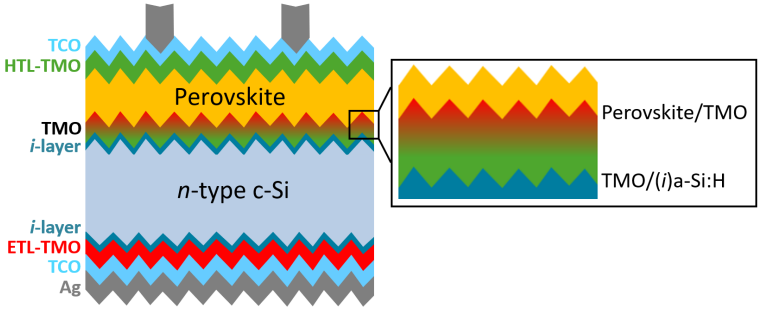

Figure 6.2: Cross-sectional sketch of 2-T SHJ/perovskite tandem solar cell.

Based on these observations, TMO materials have the potential to work as both ETL and HTL with suitable interface engineering methods. In a 2-T SHJ/perovskite tandem device, we can modify the perovskite/TMO interface to use TMO as the ETL in the top cell. Similarly, the TMO/(*i*)a-Si:H interface can be engineered to use TMO as the HTL in the bottom cell. The sketch of the novel tandem device is presented in Figure 6.2. In this way, TMO also serves as the recombination layer in the tandem structure. This approach simplifies the tandem cell structure and reduces the number of interfaces.

This simplification may potentially ease the fabrication process and improve conversion efficiency.

4. Further improvement in interface engineering method

Our research demonstrates how carefully engineered interfaces can boost the performance of TMO layers in SHJ solar cells. By depositing a 4–5 nm film stack during interface engineering methods, we achieved notable improvements in charge transport and reduced recombination, which increased overall device efficiency. While these outcomes are encouraging, there may be still room to refine the deposition process and to gain a more comprehensive understanding of material interactions at such thin boundaries. Future work may concentrate on enhancing layer-by-layer growth, exploring new TMO compositions, and employing in-situ characterization methods to push the limits of interface control.

One promising direction involves the use of artificial intelligent and machine learning techniques to understand the dynamic of interface condition and search for optimal deposition conditions. By examining small changes in growth parameters and integrating feedback rapidly, researchers can more quickly improve film quality without relying on repeated trial-and-error. Methods like ALD will be critical in achieving precise, atom-by-atom control of film thickness and surface uniformity. Additionally, advanced characterization tools such as in-situ X-ray photoelectron spectroscopy can capture dynamic shifts at the interface, revealing how aspects like atomic ration and defects throughout the growth process.

Beyond this work, interfaces are critical in any system where different materials come into contact, whether to form a functional device or to catalyze chemical reactions. This significance extends far beyond solar cells into various fields of material science, electronics, and energy. Precisely engineered interfaces can improve charge transport, minimize recombination losses, and enhance the overall system efficiency. For instance, in catalysis, interface engineering can create reactive sites that drive chemical transformations, while in electronics, it can improve device reliability and performance.

A

23.83% Efficiency SHJ Solar Cells with Ultra-Thin MoO_x Layer

This appendix provides supporting information of Chapter 3, which was included in the publication of *Progress in Photovoltaics: research and applications* * [102]

A.1. Contact resistance structures

To investigate the effect of different interface conditions on the electrical properties of the devices, we fabricated three symmetric samples with noPT, PT and PTB as interface treatments. The sketches of these samples are shown in Figure A.1. Each sample contained six 2×2 cm^2 devices for contact resistance analysis.

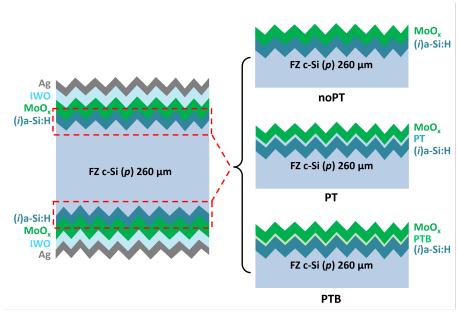

Figure A.1: The schematic structure of contact resistance sample (left) and the different hole collector stacks evaluated in this work (right).

*Cao, L., Procel, P., Alcañiz, A., Yan, J., Tichelaar, F., Özkol, E., Zhao, Y., Can, H., Yang, G., Yao, Z., Zeman, M., Santbergen, R., Mazzarella, L. and Isabella, O. (2023). Achieving 23.83% conversion efficiency in silicon heterojunction solar cell with ultra-thin MoO_x hole collector layer via tailoring (*i*)a-Si:H/MoO_x interface. Progress in Photovoltaics: research and applications, 31(12), 1245-1254. https://doi.org/10.1002/pip.3638

A

A.2. Simulation results

Table A.1 summarizes the calculated values of dipole moment in Debyes as a function of oxygen stoichiometry (x) of MoO_x. We note in Table A.1 that the magnitude of such dipole decreases for lower oxygen content in MoO_x.

Table A.1: Dipole magnitude as a function of MoO_x stoichiometry

Stoichiometry [x]	3.00	2.96	2.94	2.92	2.88
Dipole [D]	16.6	15.5	13.7	11.9	8.9

The simulated *FF*, J_{SC} and V_{OC} trends as function of the MoO_x thickness reported in Figure A.2.

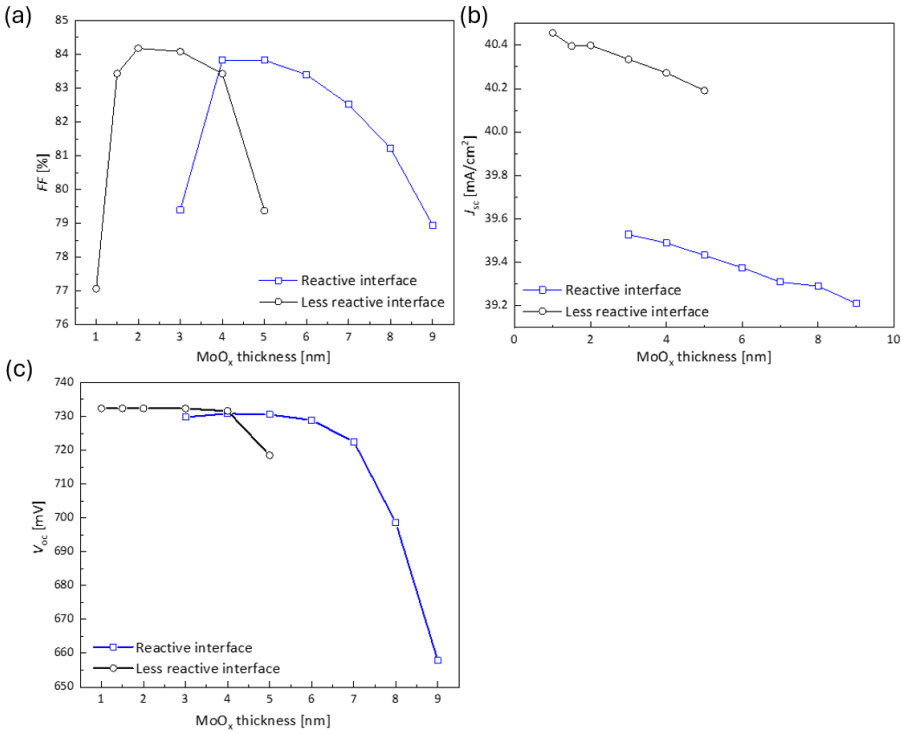

Figure A.2: Simulated *FF* (a), J_{SC} (b) and V_{OC} (c) of SHJ with MoO_x hole collector using *WF* profiles related to Figure 3.2c.

A.3. XPS Mo core-level spectra

Figure A.3 shows the Mo core level spectra for various MoO_x films with different thickness and under noPT, PT and PTB interface treatments. The +6 and +5 peaks were analysed according to the setting in Avantage software from ThermoFisher Scientific. As MoO_x thickness increases, the Mo^{+5} peaks decrease. The decrease of Mo^{+5} demonstrates that MoO_x is closer to stoichiometric state with increased thickness [166]. This trend was

the same for the results in all three interface treatments. Specially, Figure A.4 and Table A.2 provide O and Mo raw data of three conditions for 1-nm thick and 1.7-nm thick MoO_x.

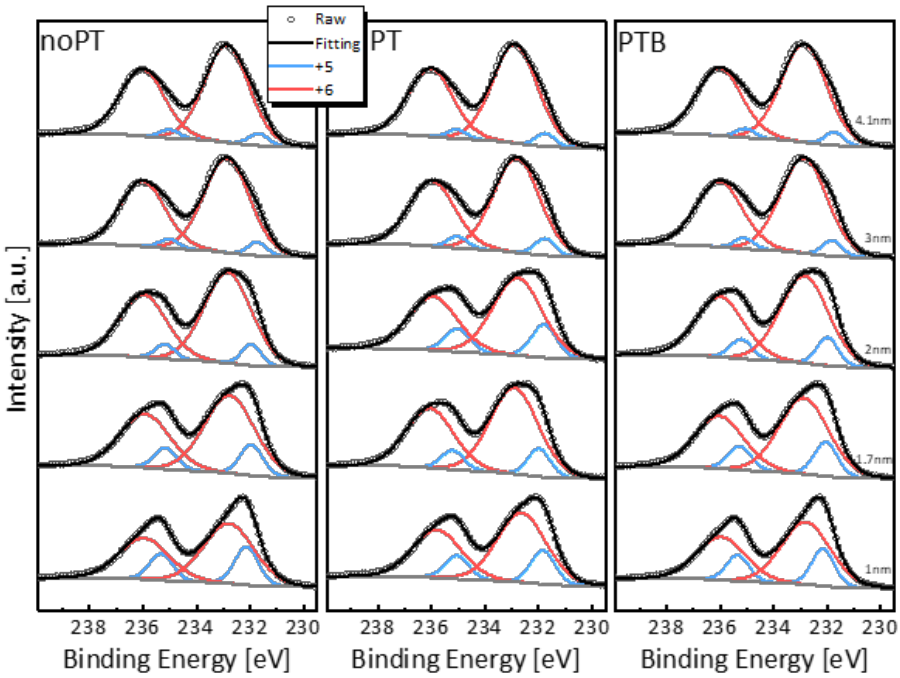

Figure A.3: Mo core-level spectra of noPT (left) PT (middle) and PTB (right) samples as function of MoO_x layer thickness.

Table A.2: Dipole magnitude as a function of MoO_x stoichiometry

1nm MoO_x	O 1s Peak BE [eV]	Atomic concentration [%]	Mo 2p Peak BE [eV]	Atomic concentration [%]
noPT	531.84	38.21	233.34	9.59
PT	531.43	41.9	233.28	9.44
PTB	531.91	39.96	233.34	9.66

1.7nm MoO_x	O 1s Peak BE [eV]	Atomic concentration [%]	Mo 2p Peak BE [eV]	Atomic concentration [%]
noPT	531.32	44.17	233.35	13.15
PT	531.41	47.88	233.39	13.55
PTB	531.44	45.86	233.36	12.91

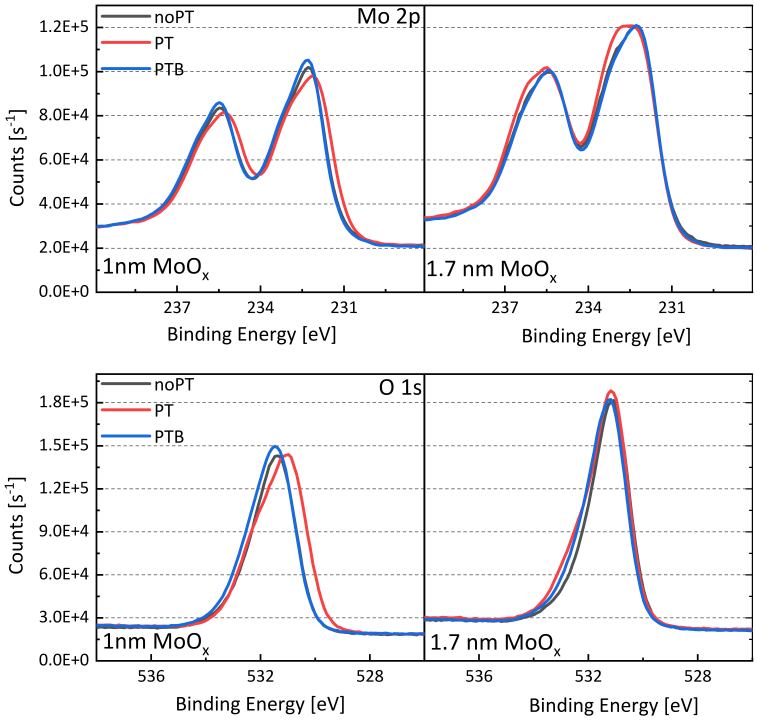

Figure A.4: Mo core-level spectra (top) and O core-level spectra (bottom) of noPT, PT and PTB samples.

A.4. Cross-sectional TEM images of the hole selective contact stacks

Figure A.5 reports the cross-sectional TEM images of (*i*)a-Si:H/MoO_x-based hole selective contacts prepared with noPT, PT and PTB interface treatment. It is noticeable that we obtained different interface features as function of the specific plasma treatment. The c-Si/(*i*)a-Si:H interface is prominent between the crystal line and the amorphous components in all three figures. The zero point of atomic profile as shown in Figure 3.3C was set at these interfaces. Combining Figure A.5 with Figure A.6, we could analyse components and thickness the layer. As for noPT sample, multilayers with different contrast could be distinguished clearly as shown in Figure A.3. The SiO_x layer was around 2 nm and Mo(In)O layer was 2.2 nm. The PT sample exhibit 2-nm thick SiO_x and 2.4-nm thick Mo(In)O layer. The PTB sample contained several layers between (*i*)a-Si:H and V_2O_x.

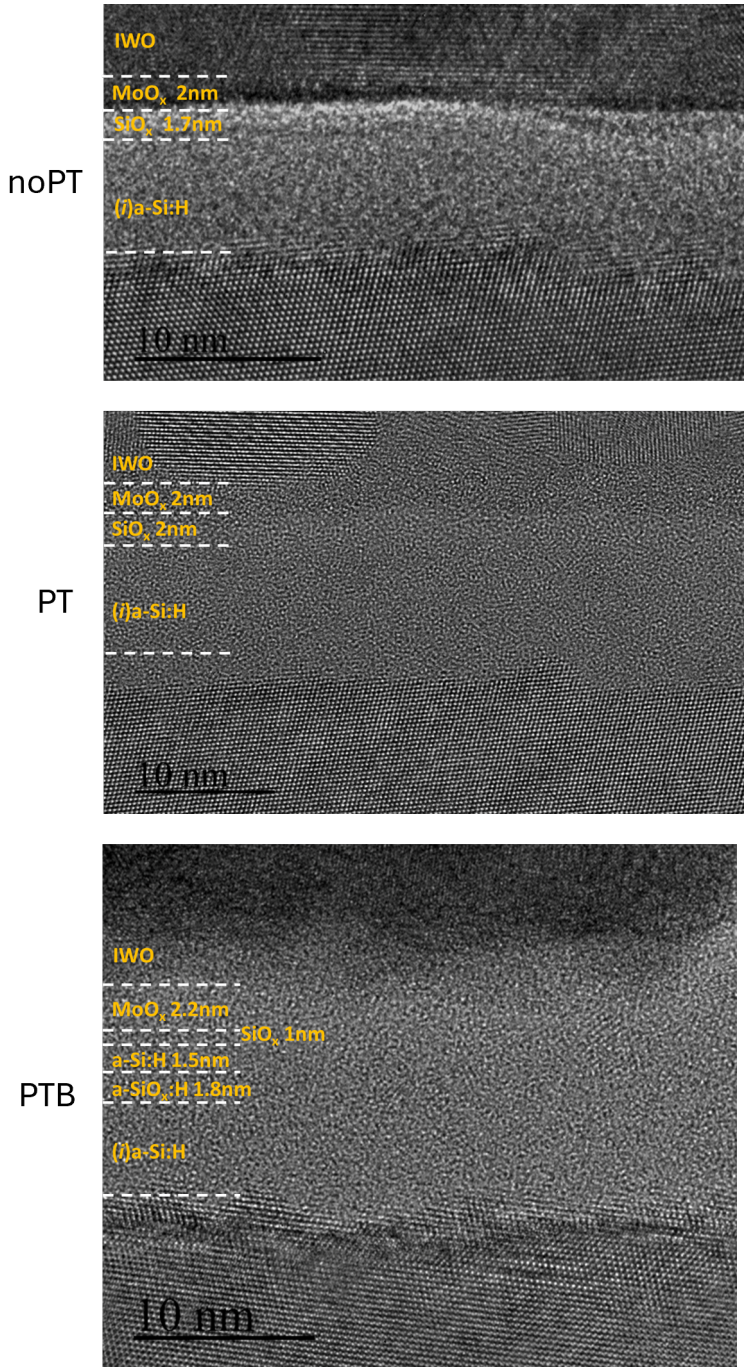

Figure A.5: HR-TEM of noPT (top); PT (middle); PTB (bottom) samples. The interface between the c-Si bulk and the (*i*)a-Si:H layer is used as origin (= 0 nm) of the depth profiling in our element composition analysis.

A.5. EDX profiles

Figure A.6 comprises the full size images reported in Figure 3.3C.

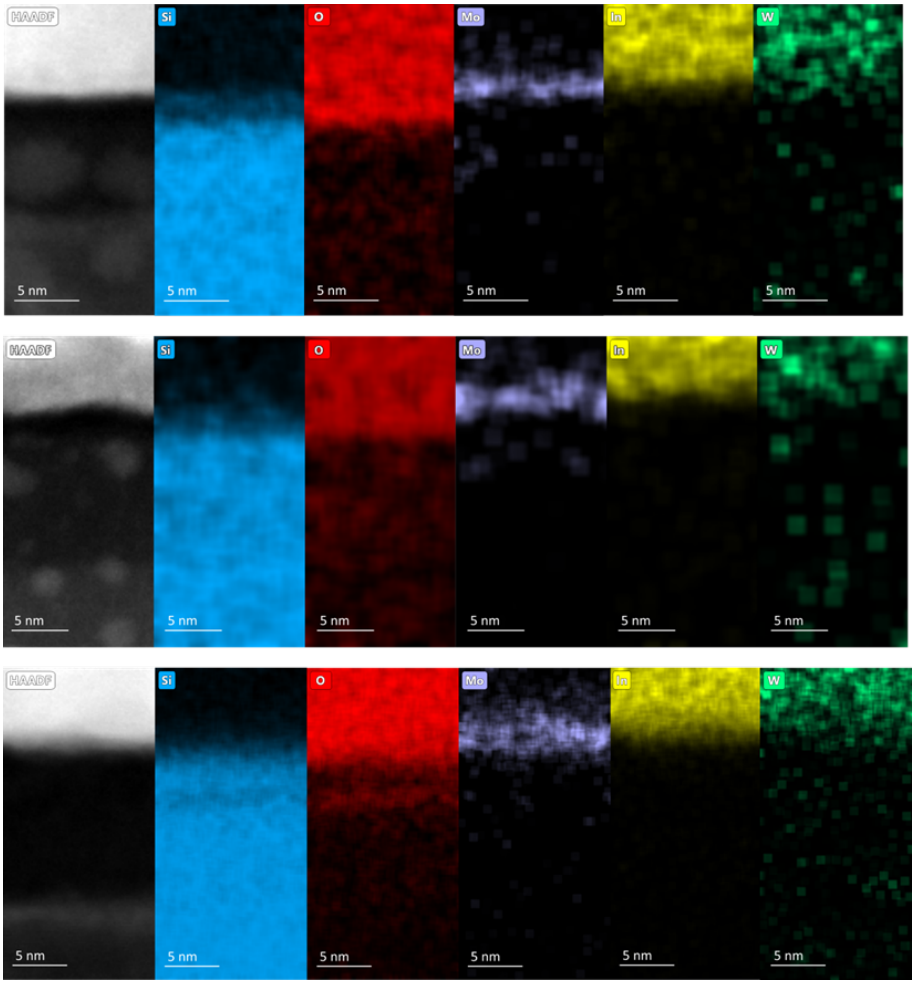

Figure A.6: EDX images of noPT (top); PT (middle); PTB (bottom) samples.

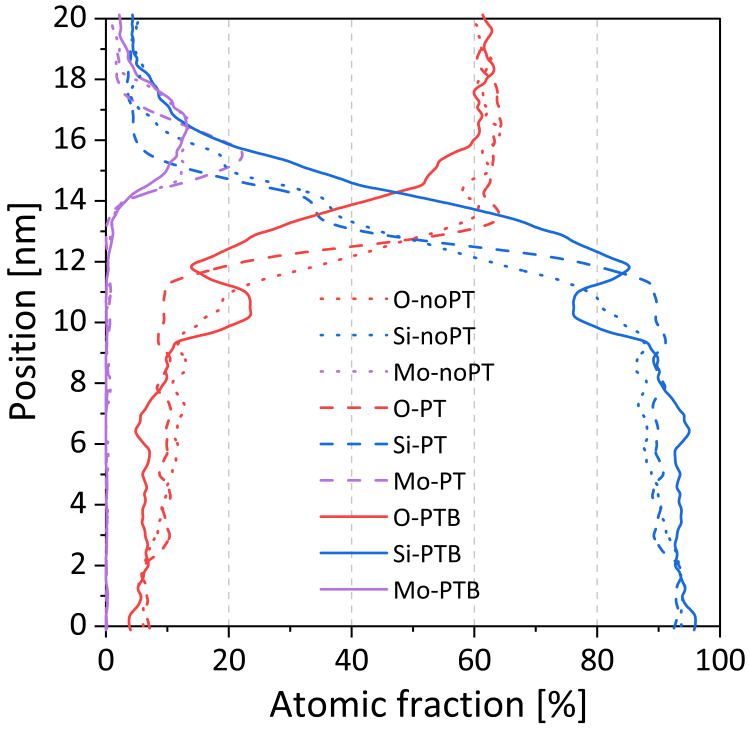

Figure A.7: O, Si and Mo atomic fraction profile for noPT, PT and PTB samples.

A.6. XPS survey spectra

The XPS survey spectra as shown in Figure A.8 illustrate that boron peak was not detected for all three samples with different interface conditions (i.e. noPT, PT and PTB) in case of 1.7-nm thick MoO_x.

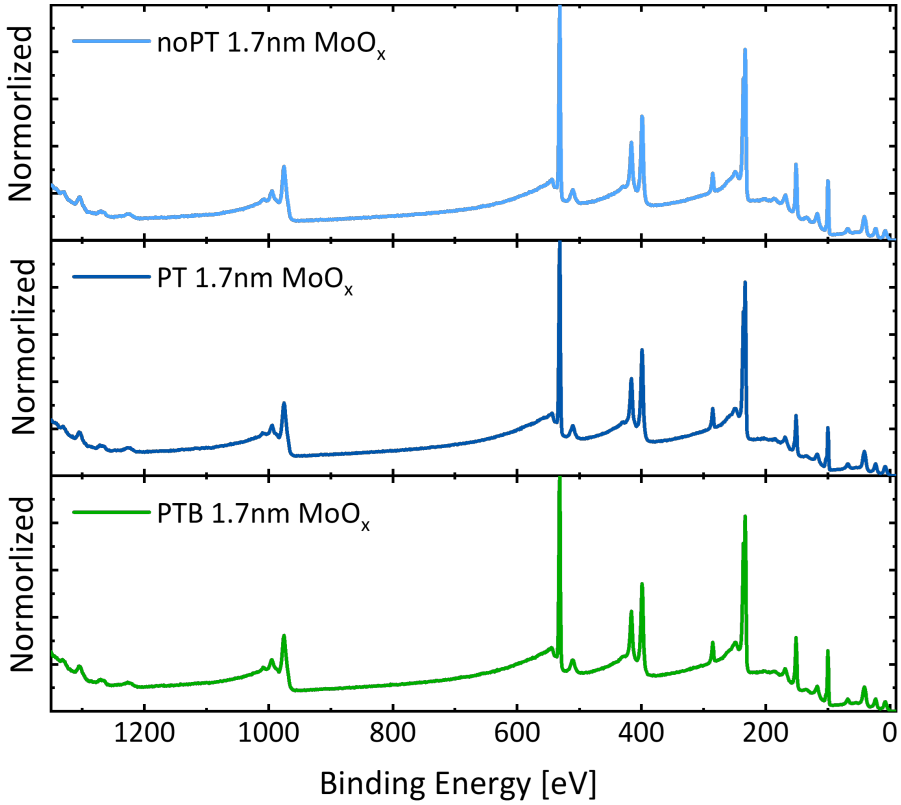

Figure A.8: EDX images of noPT (top); PT (middle); PTB (bottom) samples.

B

Indium reduction in bifacial SHJ solar cells with MoO_x collector

This appendix provides supporting information of Chapter 4, which was included in the publication of *Advanced Energy and Sustainability Research* * [50]

B.1. Simulated Jimplied gain in transition from monofacial to bifacial cell structure

The following equation illustrates the calculation of $J_{\text{implied-bifi}}$, which is formulated according to the standard [294]:

$$J_{\text{implied-bifi}} = J_{\text{implied-front}} + 0.2 \times J_{\text{implied-rear}} \tag{B.1}$$

In the equation, there are three components. $J_{\text{implied-bifi}}$ represents the photocurrent density generated by a bifacial SHJ device as shown in Figure B.1a. Figure B.1b and B.1c represent the $J_{\text{implied-bifi}}$ generated by bifacial solar cells endowed with bilayer or trilayer structure, respectively, and illuminated with 1.0 Sun illumination at the front side and 0.2 Sun illumination at the rear side. $J_{\text{implied-front}}$ refers to the photocurrent density generated from incident light on the front side of the cell. In this case simulation, the cell is illuminated only from the front side, as shown in Figure B.2a. Figure B.2b and B.2c represent the $J_{\text{implied-front}}$ generated by solar cells endowed with bilayer or trilayer structure, respectively.

$$\Delta J_{\text{implied}} = J_{\text{implied-bifi}} - J_{\text{implied-front}} = 0.2 \times J_{\text{implied-rear}} \tag{B.2}$$

$\Delta J_{\text{implied}}$ can be seen as the gain in transitioning from monofacial to bifacial structure. In Figure B.3A and B.3B we report the simulated $\Delta J_{\text{implied}}$ of bifacial SHJ solar cells with 50-nm thick IWO on both sides and bilayer or trilayer n-contact, respectively.

*Cao, L., Zhao, Y., Procel Moya, P., Han, C., Kovačević, K., Özkol, E., Zeman, M., Mazzarella, L., and Isabella, O. (2024). Indium Reduction in Bifacial Silicon Heterojunction Solar Cells with MoO_x Hole Collector. Advanced Energy and Sustainability Research, 2400105.https://doi.org/10.1002/aesr.202400105

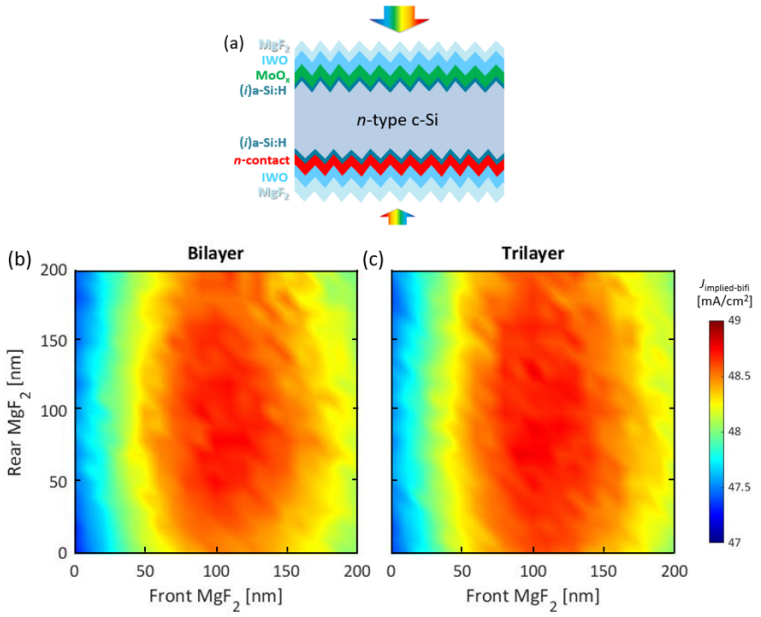

Figure B.1: (a) Sketch of the bifacial solar cell used for simulating $J_{\text{implied-bifi}}$ with 1.0 Sun illuminated from the front side and 0.2 Sun illuminated from rear side; simulated $J_{\text{implied-bifi}}$ of bifacial SHJ solar cells with 50-nm thick IWO on both sides and (b) bilayer or (c) trilayer *n*-contact.

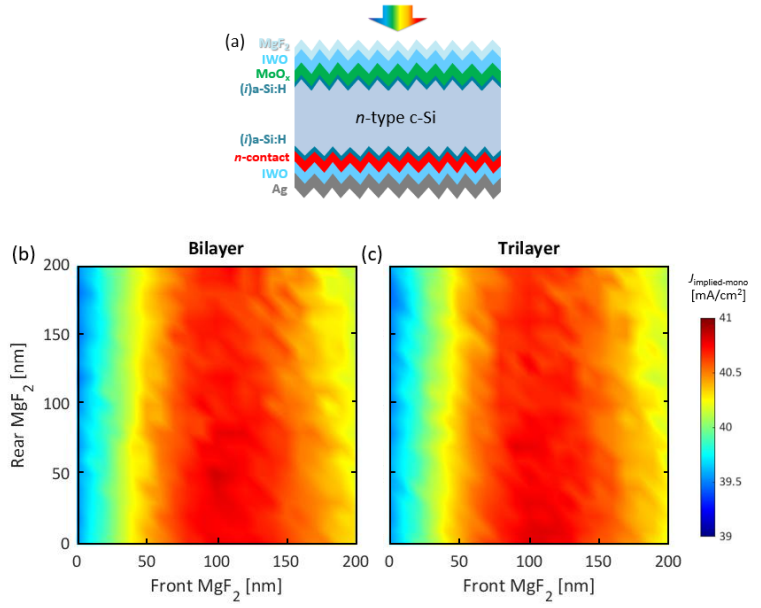

Figure B.2: (a) Sketch of the solar cell used for simulating $J_{\text{implied-front}}$ with 1.0 Sun illuminated from the front side; simulated $J_{\text{implied-front}}$ of monofacial SHJ solar cells with 50-nm thick IWO on both sides and (b) bilayer or (c) trilayer *n*-contact.

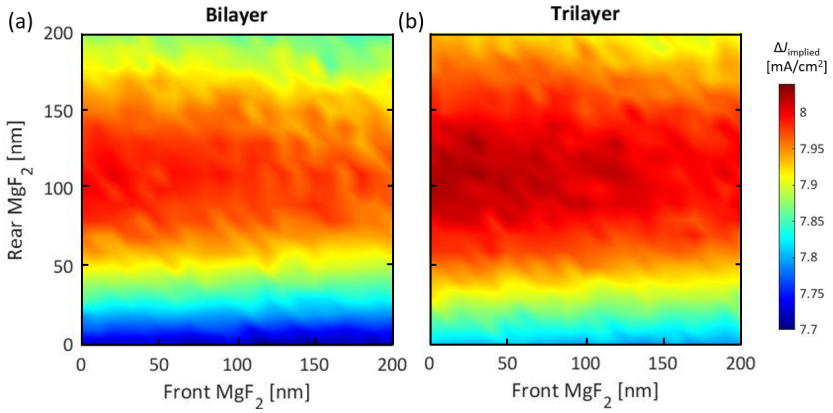

Figure B.3: Simulated $\Delta J_{\text{implied}}$ of bifacial SHJ solar cells with 50-nm thick IWO on both sides (see sketch in Figure B.1A) and (a) bilayer or (b) trilayer *n*-contact.

B.2. Reflectance of bifacial cells

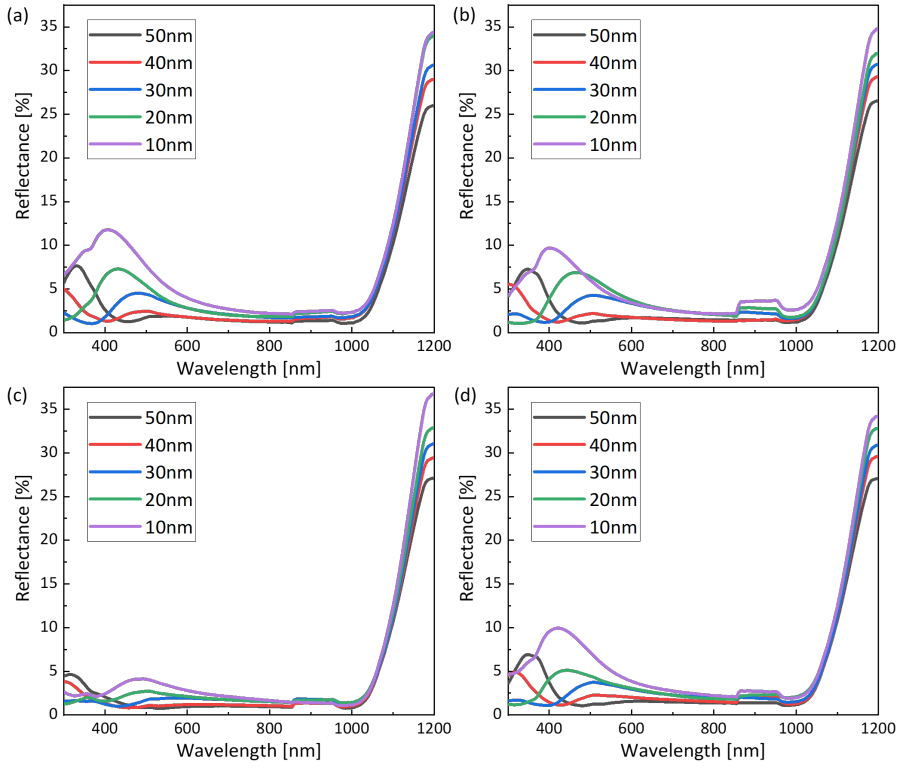

Figure B.4: Reflectance of bifacial solar cells with bilayer *n*-type stack measured from (a) *N*-side and (b) *P*-side regarding different thickness of IWO; Reflectance of bifacial solar cells with trilayer *n*-type stack measured from (c) *N*-side and (d) *P*-side regarding different thickness of IWO.

B.3. EQE of bifacial cells

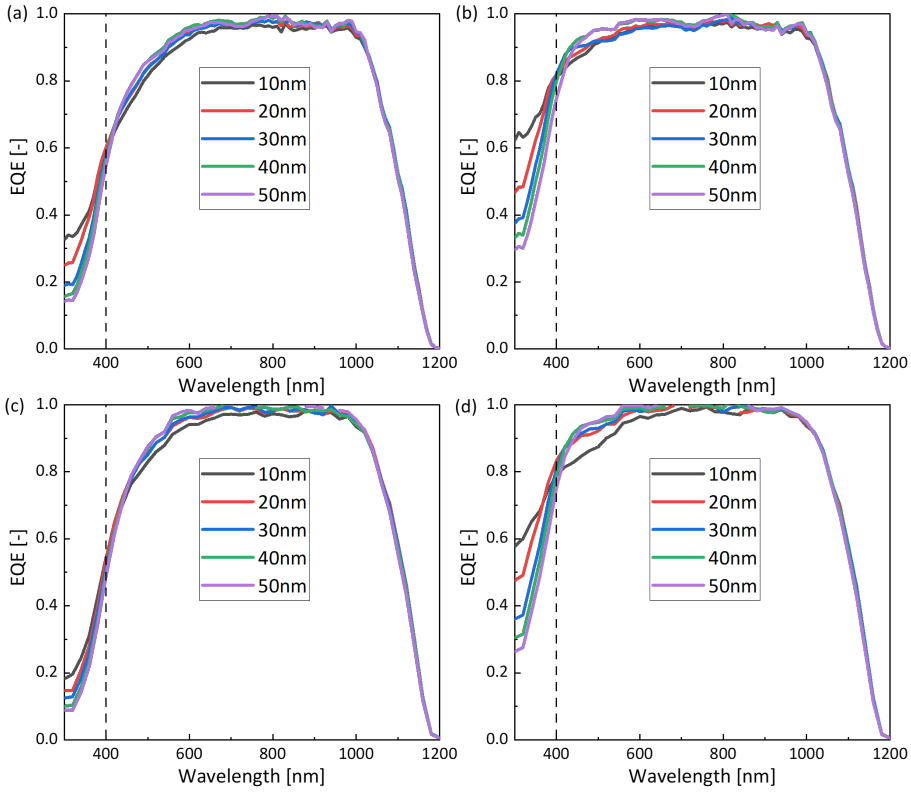

Figure B.5: External quantum efficiency (EQE) of bifacial solar cells with bilayer *n*-type stack measured from (a) *N*-side and (b) *P*-side regarding different thickness of IWO; reflectance of bifacial solar cells with trilayer *n*-type stack measured from (c) *N*-side and (d) *P*-side regarding different thickness of IWO.

B.4. Resistivity and sheet resistance of TCO layers

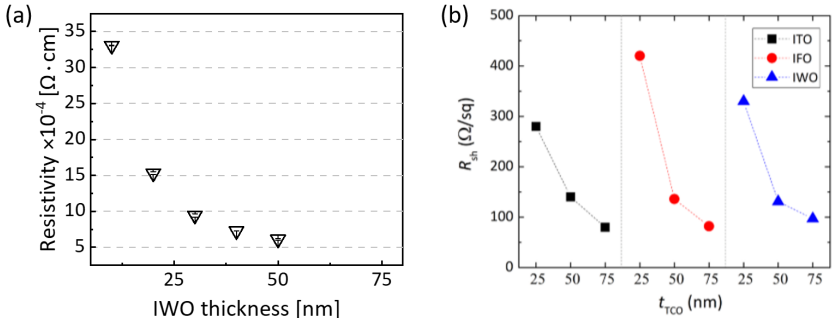

Figure B.6: (a) Resistivity an (b) sheet resistance [48] IWO (as well as ITO and IFO) as function of thickness

B.6. Minority carrier lifetime and iV_{OC} - V_{OC} of cell precursors

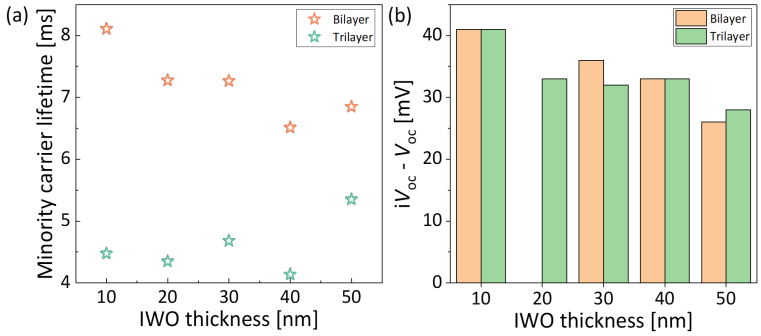

Figure B.7: (a)Minority carrier lifetime of cell precursors with bilayer and trilayer; (b) the difference between iV_{OC} (before metallization) and V_{OC} (after metallization) for bilayer and trilayer samples various IWO thickness

B.7. Certified power conversion efficiency of bifacial solar cell

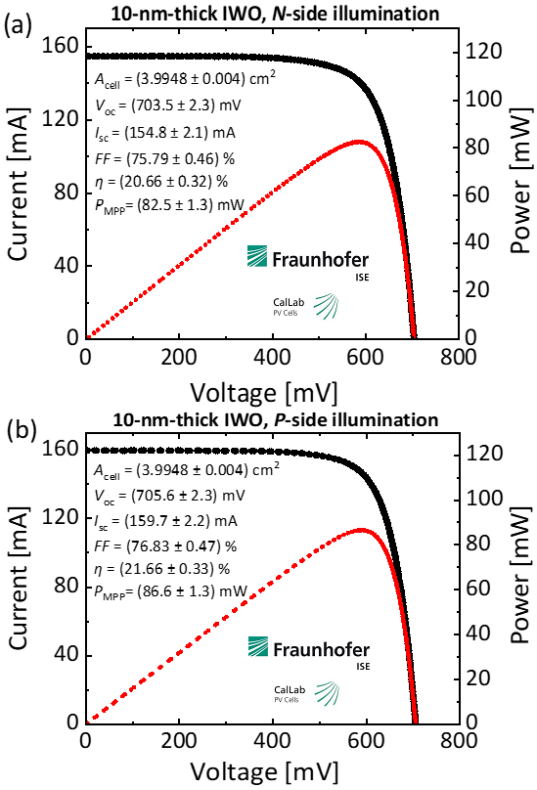

Figure B.8: Certified power conversion efficiency of bifacial solar cell with 10-nm thick IWO measured from (a) *N*-and (b) *P*-side.

C

Universal interface engineering method for applying TMO in SHJ solar cell

This appendix provides supporting information of Chapter 5, which was included in the publication in *Solar Energy Materials and Solar Cells* * [103]

C.1. Gas condition of interface engineering methods

Table C.1: Gas condition of interface engineering methods

Interface engineering method	Gas condition
noPT	-
PT	H_2, SiH_4, CO_2
PTB	H_2, SiH_4, CO_2, B_2H_6

C.2. The sketch of sample for absorbance measurement

Figure C.1: The sketch of the samples for absorptance measurement. From reflectance (R%) and transmittance spectra (T%), the absorptance of the optical system can be found as A% = A_{TMO}% + A_{glass}% = 100% - R% - T%. Considering that in the wavelength range between 400 and 1200 nm our glass is essentially lossless (A_{glass}% ~ 0%), one could assign any signal above 0% to the absorptance (A_{TMO}%) of the TMOs.

*Cao, L., Procel, P., Zhao, Y., Yan, J., Özkol, E., Kovačević, K., Zeman, M., Mazzarella, L. and Isabella, O. (2024). Universal method for applying transition metal oxides in silicon heterojunction solar cell. Solar Energy Materials and Solar Cells, 278 (2024): 113170. https://doi.org/10.1016/j.solmat.2024.113170.

C.3. Cross-sectional sketch of samples for XPS measurement

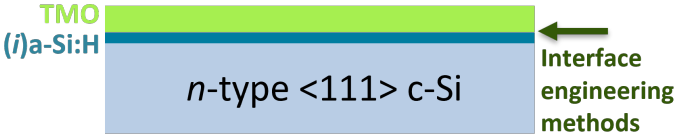

Figure C.2: Cross-sectional sketch of samples for XPS measurement.

C

C.4. XPS spectra of tungsten

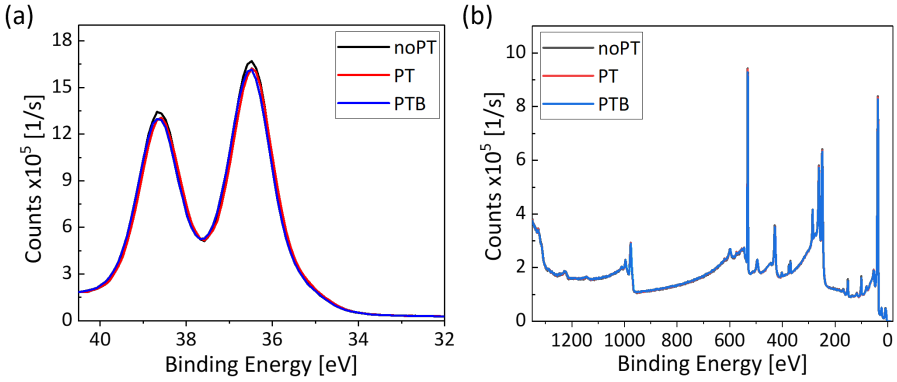

Figure C.3: The W high resolution spectra and survey spectra of samples manufactured with different interface engineering methods.

C.5. XPS spectra of vanadium

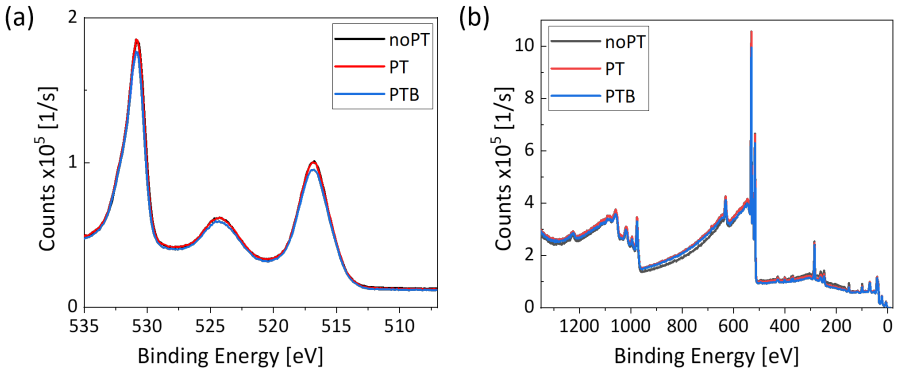

Figure C.4: The V high resolution spectra and survey spectra of samples manufactured with different interface engineering methods.

C.6. XPS spectra of boron

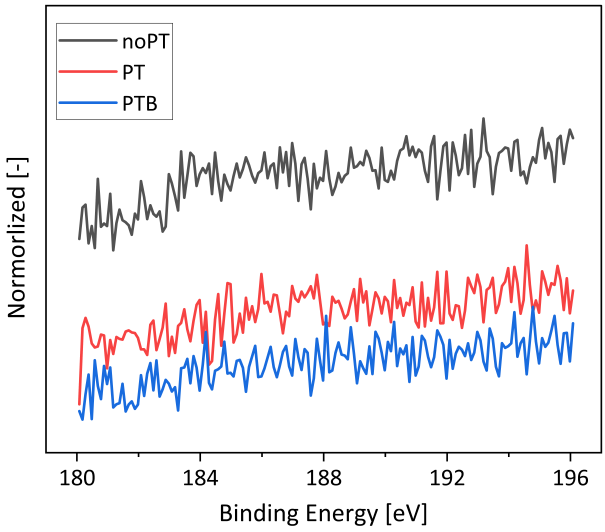

Figure C.5: The high-resolution scan of B1s spectrum of noPT, PT, and PTB samples.

C.7. Minority carriers lifetime of WO_x-based SHJ solar cell precursors

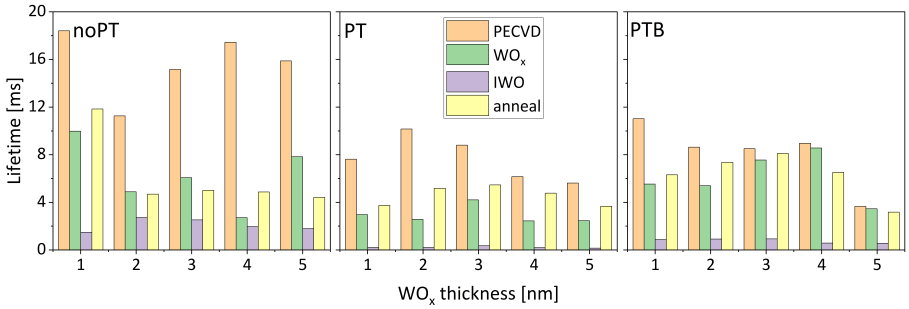

Figure C.6: Minority carriers lifetime of WO_x-based SHJ solar cell precursors manufactured with different interface engineering methods as function of WO_x thickness.

C.8. The absorptance spectrum of WO_x and V_2O_x

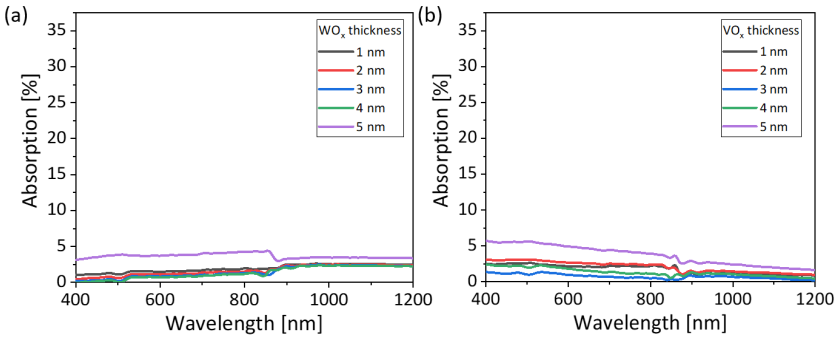

Figure C.7: The absorptance spectrum of (a) WO_x and (b) V_2O_x for different thicknesses.

C.9. Minority carriers lifetime of V_2O_x-based SHJ solar cell precursors

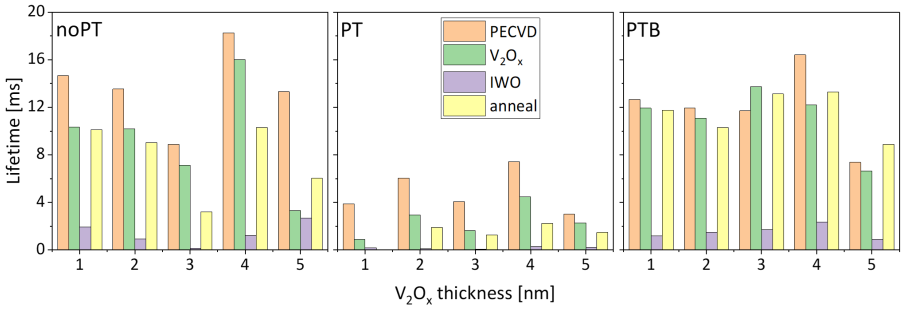

Figure C.8: Minority carriers lifetime of V_2O_x-based SHJ solar cell precursors manufactured with different interface engineering methods as function of V_2O_x thickness.

Bibliography

[1] K. Abbass, M. Z. Qasim, H. Song, M. Murshed, H. Mahmood, and I. Younis, *A review of the global climate change impacts, adaptation, and sustainable mitigation measures,* Environmental Science and Pollution Research **29**, 42539 (2022).

[2] H. Lee, K. Calvin, D. Dasgupta, G. Krinmer, A. Mukherji, P. Thorne, C. Trisos, J. Romero, P. Aldunce, K. Barret, *et al.*, *Synthesis report of the IPCC Sixth Assessment Report (AR6), Longer report. IPCC.* (2023).

[3] A. Mikhaylov, N. Moiseev, K. Aleshin, and T. Burkhardt, *Global climate change and greenhouse effect,* Entrepreneurship and Sustainability Issues **7**, 2897 (2020).

[4] J. R. Toggweiler and J. Russell, *Ocean circulation in a warming climate,* Nature **451**, 286 (2008).

[5] J. E. Overland, K. R. Wood, and M. Wang, *Warm Arctic—cold continents: climate impacts of the newly open Arctic Sea,* Polar Research **30**, 15787 (2011).

[6] J. Hansen, M. Sato, R. Ruedy, A. Lacis, and V. Oinas, *Global warming in the twenty-first century: An alternative scenario,* Proceedings of the National Academy of Sciences **97**, 9875 (2000).

[7] K. E. Trenberth, J. T. Fasullo, G. Branstator, and A. S. Phillips, *Seasonal aspects of the recent pause in surface warming,* Nature Climate Change **4**, 911 (2014).

[8] N. J. Lenssen, G. A. Schmidt, J. E. Hansen, M. J. Menne, A. Persin, R. Ruedy, and D. Zyss, *Improvements in the GISTEMP uncertainty model,* Journal of Geophysical Research: Atmospheres **124**, 6307 (2019).

[9] *GISTEMP Team, 2024: GISS Surface Temperature Analysis (GISTEMP), version 4. NASA Goddard Institute for Space Studies. Dataset accessed 2024-06-18 at data.giss.nasa.gov/gistemp/, .*

[10] J. M. Chen, *Carbon neutrality: Toward a sustainable future,* The Innovation **2** (2021).

[11] X. Zhao, X. Ma, B. Chen, Y. Shang, and M. Song, *Challenges toward carbon neutrality in China: Strategies and countermeasures,* Resources, Conservation and Recycling **176**, 105959 (2022).

[12] D. Milovanovic, M. Babic, N. Jovicic, and D. Gordic, *Energy efficiency in buildings, industry and transportation,* in *AIP Conference Proceedings*, Vol. 1499 (American Institute of Physics, 2012) pp. 71–82.

[13] M.-T. Huang and P.-M. Zhai, *Achieving Paris Agreement temperature goals requires carbon neutrality by middle century with far-reaching transitions in the whole society,* Advances in Climate Change Research **12**, 281 (2021).

[14] Y.-M. Wei, K. Chen, J.-N. Kang, W. Chen, X.-Y. Wang, and X. Zhang, *Policy and management of carbon peaking and carbon neutrality: A literature review,* Engineering **14**, 52 (2022).

[15] A. M. Omer, *Green energies and the environment,* Renewable and Sustainable Energy Reviews **12**, 1789 (2008).

[16] M. Becquerel, *Mémoire sur les effets électriques produits sous l'influence des rayons solaires,* Comptes rendus hebdomadaires des séances de l'Académie des sciences **9**, 561 (1839).

[17] M. A. Green, E. D. Dunlop, M. Yoshita, N. Kopidakis, K. Bothe, G. Siefer, X. Hao, and J. Y. Jiang, *Solar Cell Efficiency Tables (Version 65),* Progress in Photovoltaics: Research and Applications (2024).

[18] J. Mandelkorn and J. H. Lamneck Jr, *A new electric field effect in silicon solar cells,* Journal of Applied Physics **44**, 4785 (1973).

[19] J. Del Alamo, J. Eguren, and A. Luque, *Operating limits of Al-alloyed high-low junctions for BSF solar cells,* Solid-State Electronics **24**, 415 (1981).

[20] K. H. Kim, C. S. Park, J. D. Lee, J. Y. Lim, J. M. Yeon, I. H. Kim, E. J. Lee, and Y. H. Cho, *Record high efficiency of screen-printed silicon aluminum back surface field solar cell: 20.29%,* Japanese Journal of Applied Physics **56**, 08MB25 (2017).

[21] M. Green, A. Blakers, J. Shi, E. Keller, and S. Wenham, *19.1% efficient silicon solar cell,* Applied Physics Letters **44**, 1163 (1984).

[22] W. Deng, F. Ye, R. Liu, Y. Li, H. Chen, Z. Xiong, Y. Yang, Y. Chen, Y. Wang, P. P. Altermatt, *et al.*, *22.61% efficient fully screen printed PERC solar cell,* in *2017 IEEE 44th Photovoltaic Specialist Conference (PVSC)* (IEEE, 2017) pp. 2220–2226.

[23] LONGI, *LONGi Solar sets new bifacial mono-PERC solar cell world record at 24.06 percent,* LONGI Global News (2019).

[24] F. Feldmann, M. Bivour, C. Reichel, H. Steinkemper, M. Hermle, and S. W. Glunz, *Tunnel oxide passivated contacts as an alternative to partial rear contacts,* Solar Energy Materials and Solar Cells **131**, 46 (2014).

[25] *Jinkosolar's high-efficiency n-type monocrystalline silicon solar cell sets new record with maximum conversion efficiency of 26.89%,* (2023).

[26] M. Tanaka, M. Taguchi, T. Matsuyama, T. Sawada, S. Tsuda, S. Nakano, H. Hanafusa, and Y. Kuwano, *Development of new a-Si/c-Si heterojunction solar cells: ACJ-HIT (artificially constructed junction-heterojunction with intrinsic thin-layer),* Japanese Journal of Applied Physics **31**, 3518 (1992).

[27] G. Wang, Q. Su, H. Tang, H. Wu, H. Lin, C. Han, T. Wang, C. Xue, J. Lu, L. Fang, *et al.*, *27.09%-efficiency silicon heterojunction back contact solar cell and going beyond,* Nature Communications **15**, 8931 (2024).

[28] M. D. Lammert and R. J. Schwartz, *The interdigitated back contact solar cell: A silicon solar cell for use in concentrated sunlight,* IEEE Transactions on Electron Devices **24**, 337 (1977).

[29] LONGI, *34.6%! Record-breaker LONGi Once Again Sets a New World Efficiency for Silicon-perovskite Tandem Solar Cells,* LONGI Global News (2024).

[30] P. Schygulla, R. Müller, O. Höhn, M. Schachtner, D. Chojniak, A. Cordaro, S. Tabernig, B. Bläsi, A. Polman, G. Siefer, *et al.*, *Wafer-bonded two-terminal III-V//Si triple-junction solar cell with power conversion efficiency of 36.1% at AM1. 5g,* Progress in Photovoltaics: Research and Applications (2024).

[31] Y. Zhao, English*Hydrogenated nanocrystalline silicon-based layers for silicon heterojunction and perovskite/c-Si tandem solar cells*, Dissertation, Delft University of Technology (2023).

[32] M. Noman, Z. Khan, and S. T. Jan, *A comprehensive review on the advancements and challenges in perovskite solar cell technology,* RSC advances **14**, 5085 (2024).

[33] H. S. Jung and N.-G. Park, *Perovskite solar cells: from materials to devices,* Small **11**, 10 (2015).

[34] N.-G. Park, *Perovskite solar cells: an emerging photovoltaic technology,* Materials today **18**, 65 (2015).

[35] K. O. Brinkmann, P. Wang, F. Lang, W. Li, X. Guo, F. Zimmermann, S. Olthof, D. Neher, Y. Hou, M. Stolterfoht, *et al.*, *Perovskite–organic tandem solar cells,* Nature Reviews Materials **9**, 202 (2024).

[36] VDMA, *The International Technology Roadmap for Photovoltaic (ITRPV) (15th Edition, May 2024) - 15th Edition,* VDMA Report (2024).

[37] Z. Sun, X. Chen, Y. He, J. Li, J. Wang, H. Yan, and Y. Zhang, *Toward efficiency limits of crystalline silicon solar cells: recent progress in high-efficiency silicon heterojunction solar cells,* Advanced Energy Materials **12**, 2200015 (2022).

[38] H. A. Gatz, J. K. Rath, M. A. Verheijen, W. M. Kessels, and R. E. Schropp, *Silicon heterojunction solar cell passivation in combination with nanocrystalline silicon oxide emitters,* Physica Status Solidi (a) **213**, 1932 (2016).

[39] M. Zeman and D. Zhang, *Heterojunction silicon based solar cells,* in *Physics and Technology of Amorphous-Crystalline Heterostructure Silicon Solar Cells*, edited by W. G. J. H. M. van Sark, L. Korte, and F. Roca (Springer Berlin Heidelberg, Berlin, Heidelberg, 2012) pp. 13–43.

[40] S. De Wolf, A. Descoeudres, Z. C. Holman, and C. Ballif, *High-efficiency silicon heterojunction solar cells: A review,* Green **2**, 7 (2012).

[41] Y. Liu, Y. Li, Y. Wu, G. Yang, L. Mazzarella, P. Procel-Moya, A. C. Tamboli, K. Weber, M. Boccard, O. Isabella, *et al.*, *High-efficiency silicon heterojunction solar cells: materials, devices and applications,* Materials Science and Engineering: R: Reports **142**, 100579 (2020).

[42] J. Haschke, O. Dupré, M. Boccard, and C. Ballif, *Silicon heterojunction solar cells: Recent technological development and practical aspects-from lab to industry,* Solar Energy Materials and Solar Cells **187**, 140 (2018).

[43] W. Liu, L. Zhang, X. Yang, J. Shi, L. Yan, L. Xu, Z. Wu, R. Chen, J. Peng, J. Kang, *et al.*, *Damp-heat-stable, high-efficiency, industrial-size silicon heterojunction solar cells,* Joule **4**, 913 (2020).

[44] A. Louwen, W. Van Sark, R. Schropp, and A. Faaij, *A cost roadmap for silicon heterojunction solar cells,* Solar Energy Materials and Solar Cells **147**, 295 (2016).

[45] J. Yu, J. Li, Y. Zhao, A. Lambertz, T. Chen, W. Duan, W. Liu, X. Yang, Y. Huang, and K. Ding, *Copper metallization of electrodes for silicon heterojunction solar cells: Process, reliability and challenges,* Solar Energy Materials and Solar Cells **224**, 110993 (2021).

[46] Y. Zhang, M. Kim, L. Wang, P. Verlinden, and B. Hallam, *Design considerations for multi-terawatt scale manufacturing of existing and future photovoltaic technologies: challenges and opportunities related to silver, indium and bismuth consumption,* Energy & Environmental Science **14**, 5587 (2021).

[47] K. Ravichandran, N. Jabena Begum, S. Snega, and B. Sakthivel, *Properties of sprayed aluminum-doped zinc oxide films—a review,* Materials and Manufacturing Processes **31**, 1411 (2016).

[48] C. Han, R. Santbergen, M. van Duffelen, P. Procel, Y. Zhao, G. Yang, X. Zhang, M. Zeman, L. Mazzarella, and O. Isabella, *Towards bifacial silicon heterojunction solar cells with reduced TCO use,* Progress in Photovoltaics: Research and Applications **30**, 750 (2022).

[49] T. Gageot, J. Veirman, F. Jay, D. Muñoz-Rojas, C. Denis, R. Couderc, A.-S. Ozanne, R. Monna, S. Zogbo, and R. Cabal, *Feasibility test of drastic indium cut down in SHJ solar cells and modules using ultra-thin ITO layers,* Solar Energy Materials and Solar Cells **261**, 112512 (2023).

[50] L. Cao, Y. Zhao, P. Procel Moya, C. Han, K. Kovačević, E. Özkol, M. Zeman, L. Mazzarella, and O. Isabella, *Indium Reduction in Bifacial Silicon Heterojunction Solar Cells with MoO_x Hole Collector,* Advanced Energy and Sustainability Research , 2400105 (2024).

[51] Z. C. Holman, A. Descoeudres, L. Barraud, F. Z. Fernandez, J. P. Seif, S. De Wolf, and C. Ballif, *Current losses at the front of silicon heterojunction solar cells,* IEEE Journal of Photovoltaics **2**, 7 (2012).

[52] Y. Wang, S.-T. Zhang, L. Li, X. Yang, L. Lu, and D. Li, *Dopant-free passivating contacts for crystalline silicon solar cells: Progress and prospects,* EcoMat **5**, e12292 (2023).

[53] W. Rehm, R. Fischer, J. Stuke, and H. Wagner, *Photo and dark conductivity of doped amorphous silicon,* Physica Status Solidi (b) **79**, 539 (1977).

[54] S. De Wolf and M. Kondo, *Boron-doped a-Si:H/ c-Si interface passivation: Degradation mechanism,* Applied Physics Letters **91** (2007).

[55] H. Lin, M. Yang, X. Ru, G. Wang, S. Yin, F. Peng, C. Hong, M. Qu, J. Lu, L. Fang, *et al.*, *Silicon heterojunction solar cells with up to 26.81% efficiency achieved by electrically optimized nanocrystalline-silicon hole contact layers,* Nature Energy **8**, 789 (2023).

[56] C. Yu, K. Gao, C.-W. Peng, C. He, S. Wang, W. Shi, V. Allen, J. Zhang, D. Wang, G. Tian, *et al.*, *Industrial-scale deposition of nanocrystalline silicon oxide for 26.4%-efficient silicon heterojunction solar cells with copper electrodes,* Nature Energy **8**, 1375 (2023).

[57] D. Qiu, A. Lambertz, W. Duan, L. Mazzarella, P. Wagner, A. B. Morales-Vilches, G. Yang, P. Procel, O. Isabella, B. Stannowski, *et al.*, *A Review: Application of Doped Hydrogenated Nanocrystalline Silicon Oxide in High Efficiency Solar Cell Devices,* Advanced Science , 2403728 (2024).

[58] Y. Zhao, P. Procel, C. Han, L. Mazzarella, G. Yang, A. Weeber, M. Zeman, and O. Isabella, *Design and optimization of hole collectors based on nc-SiO_x: H for high-efficiency silicon heterojunction solar cells,* Solar Energy Materials and Solar Cells **219**, 110779 (2021).

[59] H. Fujiwara and M. Kondo, *Effects of a-Si:H layer thicknesses on the performance of a-Si:H/ c-Si heterojunction solar cells,* Journal of Applied Physics **101** (2007).

[60] C. Battaglia, X. Yin, M. Zheng, I. D. Sharp, T. Chen, S. McDonnell, A. Azcatl, C. Carraro, B. Ma, R. Maboudian, *et al.*, *Hole selective MoO_x contact for silicon solar cells,* Nano Letters **14**, 967 (2014).

[61] J. Bullock, M. Hettick, J. Geissbühler, A. J. Ong, T. Allen, C. M. Sutter-Fella, T. Chen, H. Ota, E. W. Schaler, S. De Wolf, *et al.*, *Efficient silicon solar cells with dopant-free asymmetric heterocontacts,* Nature Energy **1**, 1 (2016).

[62] S. Avasthi, W. E. McClain, G. Man, A. Kahn, J. Schwartz, and J. C. Sturm, *Hole-blocking titanium-oxide/silicon heterojunction and its application to photovoltaics,* Applied Physics Letters **102** (2013).

[63] M. Bivour, J. Temmler, H. Steinkemper, and M. Hermle, *Molybdenum and tungsten oxide: High work function wide band gap contact materials for hole selective contacts of silicon solar cells,* Solar Energy Materials and Solar Cells **142**, 34 (2015).

[64] J. Bullock, Y. Wan, M. Hettick, X. Zhaoran, S. P. Phang, D. Yan, H. Wang, W. Ji, C. Samundsett, Z. Hameiri, *et al.*, *Dopant-free partial rear contacts enabling 23% silicon solar cells,* Advanced Energy Materials **9**, 1803367 (2019).

[65] J. Ding, Y. Zhou, G. Dong, M. Liu, D. Yu, and F. Liu, *Solution-processed ZnO as the efficient passivation and electron selective layer of silicon solar cells,* Progress in Photovoltaics: Research and Applications **26**, 974 (2018).

[66] J. Dréon, Q. Jeangros, J. Cattin, J. Haschke, L. Antognini, C. Ballif, and M. Boccard, *23.5%-efficient silicon heterojunction silicon solar cell using molybdenum oxide as hole-selective contact,* Nano Energy **70**, 104495 (2020).

[67] G. Du, L. Li, H. Zhu, L. Lu, X. Zhou, Z. Gu, S.-T. Zhang, X. Yang, J. Wang, L. Yang, *et al.*, *High-performance hole-selective V_2O_x/SiO_x/NiO_x contact for crystalline silicon solar cells,* EcoMat **4**, e12175 (2022).

[68] J. Geissbühler, J. Werner, S. Martin de Nicolas, L. Barraud, A. Hessler-Wyser, M. Despeisse, S. Nicolay, A. Tomasi, B. Niesen, S. De Wolf, *et al.*, *22.5% efficient silicon heterojunction solar cell with molybdenum oxide hole collector,* Applied Physics Letters **107** (2015).

[69] L. G. Gerling, S. Mahato, A. Morales-Vilches, G. Masmitja, P. Ortega, C. Voz, R. Alcubilla, and J. Puigdollers, *Transition metal oxides as hole-selective contacts in silicon heterojunctions solar cells,* Solar Energy Materials and Solar Cells **145**, 109 (2016).

[70] J. Hossain, M. Rahman, M. M. A. Moon, B. K. Mondal, M. F. Rahman, and M. H. Rubel, *Guidelines for a highly efficient CuI/n-Si heterojunction solar cell,* Engineering Research Express **2**, 045019 (2020).

[71] L. Jin, L. Cai, D. Chen, W. Wang, H. Shen, and F. Zhang, *Efficient silicon solar cells applying cuprous sulfide as hole-selective contact,* Journal of Materials Science **54**, 12650 (2019).

[72] L. Li, G. Du, X. Zhou, Y. Lin, Y. Jiang, X. Gao, L. Lu, G. Li, W. Zhang, Q. Feng, *et al.*, *Interfacial engineering of Cu_2O_x passivating contact for efficient crystalline silicon solar cells with an Al_2O_3 passivation layer,* ACS Applied Materials & Interfaces **13**, 28415 (2021).

[73] J. Li, C. Guo, Y. Bai, W. Liu, Y. Chen, J. He, D. Li, X. Yang, Q. Qiu, T. Chen, *et al.*, *One-step formation of low work-function, transparent and conductive MgF_xO_y electron extraction for silicon solar cells,* Advanced Science **9**, 2202400 (2022).

[74] Z. Liang, Y. Wang, M. Su, W. Mai, J. Xu, W. Xie, and P. Liu, *Improving the Quality of the Si/Cu_2O_x Interface by Methyl-Group Passivation and Its Application in Photovoltaic Devices,* Advanced Materials Interfaces **4**, 1600833 (2017).

[75] W. Lin, W. Wu, Z. Liu, K. Qiu, L. Cai, Z. Yao, B. Ai, Z. Liang, and H. Shen, *Chromium trioxide hole-selective heterocontacts for silicon solar cells,* ACS applied materials & interfaces **10**, 13645 (2018).

[76] W. Lin, W. Wu, Q. Xie, Z. Liu, K. Qiu, L. Cai, Z. Yao, L. Meng, B. Ai, Z. Liang, *et al.*, *Conductive cuprous iodide hole-selective contacts with thermal and ambient stability for silicon solar cells,* ACS applied materials & interfaces **10**, 43699 (2018).

[77] M. Liu, Y. Zhou, G. Dong, W. Wang, J. Wang, C. Liu, F. Liu, and D. Yu, *SnO_2/Mg combination electron selective transport layer for Si heterojunction solar cells,* Solar Energy Materials and Solar Cells **200**, 109996 (2019).

[78] Y. Liu, J. Zhu, L. Cai, Z. Yao, C. Duan, Z. Zhao, C. Zhao, and W. Mai, *Solution-processed high-quality Cu_2O_x thin films as hole transport layers for pushing the conversion efficiency limit of Cu_2O_x/Si heterojunction solar cells,* Solar RRL **4**, 1900339 (2020).

[79] X. Lou, X. Wang, D. Xu, K. Gao, S. Wang, C. Xing, K. Li, W. Li, D. Li, G. Xu, *et al.*, *Polymeric Hole-Selective Contact for Crystalline Silicon Solar Cells,* Solar RRL **7**, 2300796 (2023).

[80] G. Masmitjà, L. G. Gerling, P. Ortega, J. Puigdollers, I. Martín, C. Voz, and R. Alcubilla, *V_2O_x-based hole-selective contacts for c-Si interdigitated back-contacted solar cells,* Journal of Materials Chemistry A **5**, 9182 (2017).

[81] M. Nayak, S. Mandal, A. Pandey, S. Mudgal, S. Singh, and V. K. Komarala, *Nickel oxide hole-selective heterocontact for silicon solar cells: role of SiO_x interlayer on device performance,* Solar RRL **3**, 1900261 (2019).

[82] J. Schmidt, V. Titova, and D. Zielke, *Organic-silicon heterojunction solar cells: Open-circuit voltage potential and stability,* Applied Physics Letters **103** (2013).

[83] A. Sekkat, D. Bellet, G. Chichignoud, A. Kaminski-Cachopo, D. Muñoz-Rojas, W. Favre, *et al.*, *Open-air, low-temperature deposition of phase pure Cu 2 O thin films as efficient hole-transporting layers for silicon heterojunction solar cells,* Journal of Materials Chemistry A **9**, 15968 (2021).

[84] Y. Wan, C. Samundsett, J. Bullock, T. Allen, M. Hettick, D. Yan, P. Zheng, X. Zhang, J. Cui, J. McKeon, *et al.*, *Magnesium fluoride electron-selective contacts for crystalline silicon solar cells,* ACS applied materials & interfaces **8**, 14671 (2016).

[85] Y. Wan, C. Samundsett, J. Bullock, M. Hettick, T. Allen, D. Yan, J. Peng, Y. Wu, J. Cui, A. Javey, *et al.*, *Conductive and stable magnesium oxide electron-selective contacts for efficient silicon solar cells,* Advanced Energy Materials **7**, 1601863 (2017).

[86] Y. Wan, S. K. Karuturi, C. Samundsett, J. Bullock, M. Hettick, D. Yan, J. Peng, P. R. Narangari, S. Mokkapati, H. H. Tan, *et al.*, *Tantalum oxide electron-selective heterocontacts for silicon photovoltaics and photoelectrochemical water reduction,* ACS Energy Letters **3**, 125 (2017).

[87] Q. Wang, Y. Zhou, W. Guo, Y. Yang, J. Shang, H. Chen, H. Mao, T. Zhu, Y. Zhou, and F. Liu, *p-type c-Si/SnO_2/Mg heterojunction solar cells with an induced inversion layer,* Applied Physics Letters **119** (2021).

[88] Z. Wang, Z. Liu, H. Lin, F. Ye, and P. Gao, *Hot wire Oxidation–Sublimation derived work function tunable WO_x thin films for building hole-selective contacts,* Materials Today Energy **38**, 101439 (2023).

[89] W. Wang, L. Cai, L. Meng, N. Chen, H. Wei, Y. Hong, Y. Chen, L. Zeng, and Z. Liang, *Stable Dopant-Free Electron-Selective Contact for Silicon Solar Cells,* ACS Applied Energy Materials **6**, 11234 (2023).

[90] A. Xie, G. Wang, Y. Sun, H. Cai, X. Su, P. Cao, Z. Li, Z. Chen, J. He, and P. Gao, *Bifacial silicon heterojunction solar cells using transparent-conductive-oxide-and dopant-free electron-selective contacts,* Progress in Photovoltaics: Research and Applications **32**, 664 (2024).

[91] Z. Xu, X. Liu, J. Zhou, Y. Yan, Y. Song, Q. Huang, H. Ren, Y. Ding, X. Zhang, Y. Zhao, *et al.*, *Aluminum and Molybdenum Co-Doped Zinc Oxide Films as Dual-Functional Carrier-Selective Contact for Silicon Solar Cells,* ACS Applied Materials & Interfaces **15**, 34964 (2023).

[92] D. Xu, Q. Bi, K. Li, K. Gao, X. Wang, W. Shi, S. Wang, C. Xing, X. Zhang, and X. Yang, *High-Performance Transparent Electron-Selective Contact for Crystalline Silicon Solar Cells,* Advanced Functional Materials , 2407290 (2024).

[93] M. Xue, R. Islam, A. C. Meng, Z. Lyu, C.-Y. Lu, C. Tae, M. R. Braun, K. Zang, P. C. McIntyre, T. I. Kamins, *et al.*, *Contact selectivity engineering in a 2 µm thick ultrathin c-Si solar cell using transition-metal oxides achieving an efficiency of 10.8%,* ACS applied materials & interfaces **9**, 41863 (2017).

[94] X. Yang, Q. Bi, H. Ali, K. Davis, W. V. Schoenfeld, and K. Weber, *High-Performance TiO_2-Based Electron-Selective Contacts for Crystalline Silicon Solar Cells.* Advanced Materials **28**, 5891 (2016).

[95] X. Yang, K. Weber, Z. Hameiri, and S. De Wolf, *Industrially feasible, dopant-free, carrier-selective contacts for high-efficiency silicon solar cells,* Progress in Photovoltaics: Research and Applications **25**, 896 (2017).

[96] X. Yang, E. Aydin, H. Xu, J. Kang, M. Hedhili, W. Liu, Y. Wan, J. Peng, C. Samundsett, A. Cuevas, *et al.*, *Tantalum nitride electron-selective contact for crystalline silicon solar cells,* Advanced Energy Materials **8**, 1800608 (2018).

[97] X. Yang, W. Liu, M. De Bastiani, T. Allen, J. Kang, H. Xu, E. Aydin, L. Xu, Q. Bi, H. Dang, *et al.*, *Dual-function electron-conductive, hole-blocking titanium nitride contacts for efficient silicon solar cells,* Joule **3**, 1314 (2019).

[98] X. Yang, H. Xu, W. Liu, Q. Bi, L. Xu, J. Kang, M. N. Hedhili, B. Sun, X. Zhang, and S. De Wolf, *Atomic layer deposition of vanadium oxide as hole-selective contact for crystalline silicon solar cells,* Advanced Electronic Materials **6**, 2000467 (2020).

[99] S. Zhong, M. Morales-Masis, M. Mews, L. Korte, Q. Jeangros, W. Wu, M. Boccard, and C. Ballif, *Exploring co-sputtering of ZnO: Al and SiO2 for efficient electron-selective contacts on silicon solar cells,* Solar Energy Materials and Solar Cells **194**, 67 (2019).

[100] S. Zhong, J. Dreon, Q. Jeangros, E. Aydin, S. De Wolf, F. Fu, M. Boccard, and C. Ballif, *Mitigating plasmonic absorption losses at rear electrodes in high-efficiency silicon solar cells using dopant-free contact stacks,* Advanced Functional Materials **30**, 1907840 (2020).

[101] D. Zielke, A. Pazidis, F. Werner, and J. Schmidt, *Organic-silicon heterojunction solar cells on n-type silicon wafers: The BackPEDOT concept,* Solar Energy Materials and Solar Cells **131**, 110 (2014).

[102] L. Cao, P. Procel, A. Alcañiz, J. Yan, F. Tichelaar, E. Özkol, Y. Zhao, C. Han, G. Yang, Z. Yao, *et al.*, *Achieving 23.83% conversion efficiency in silicon heterojunction solar cell with ultra-thin MoO_x hole collector layer via tailoring (i) a-Si:H/MoO_x interface,* Progress in Photovoltaics: Research and Applications **31**, 1245 (2023).

[103] L. Cao, P. Procel, A. Alcañiz, J. Yan, F. Tichelaar, E. Özkol, Y. Zhao, C. Han, G. Yang, Z. Yao, *et al.*, *Universal interface engineering method for applying transition metal oxides in silicon heterojunction solar cell,under review,* Solar Energy Materials and Solar Cells (2024).

[104] J. Bullock, A. Cuevas, T. Allen, and C. Battaglia, *Molybdenum oxide MoO_x: A versatile hole contact for silicon solar cells,* Applied Physics Letters **105** (2014).

[105] P. Gao, Z. Yang, J. He, J. Yu, P. Liu, J. Zhu, Z. Ge, and J. Ye, *Dopant-free and carrier-selective heterocontacts for silicon solar cells: recent advances and perspectives,* Advanced Science **5**, 1700547 (2018).

[106] K. Mallem, Y. J. Kim, S. Q. Hussain, S. Dutta, A. H. T. Le, M. Ju, J. Park, Y. H. Cho, Y. Kim, E.-C. Cho, *et al.*, *Molybdenum oxide: A superior hole extraction layer for replacing p-type hydrogenated amorphous silicon with high efficiency heterojunction Si solar cells,* Materials Research Bulletin **110**, 90 (2019).

[107] N. L. Chang, G. K. Poduval, B. Sang, K. Khoo, M. Woodhouse, F. Qi, M. Dehghanimadvar, W. M. Li, R. J. Egan, and B. Hoex, *Techno-economic analysis of the use of atomic layer deposited transition metal oxides in silicon heterojunction solar cells,* Progress in Photovoltaics: Research and Applications **31**, 414 (2023).

[108] Z. Chen, N. Han, R. Zheng, Z. Ren, W. Wei, and B.-J. Ni, *Design of earth-abundant amorphous transition metal-based catalysts for electrooxidation of small molecules: advances and perspectives,* SusMat **3**, 290 (2023).

[109] J. Ibarra Michel, J. Dréon, M. Boccard, J. Bullock, and B. Macco, *Carrier-selective contacts using metal compounds for crystalline silicon solar cells,* Progress in Photovoltaics: Research and Applications **31**, 380 (2023).

[110] K. Kovačević, Y. Zhao, P. Procel, L. Cao, L. Mazzarella, and O. Isabella, *Interdigitated-back-contacted silicon heterojunction solar cells featuring novel MoO_x-based contact stacks,* Progress in Photovoltaics: Research and Applications (2024).

[111] W. Wu, W. Lin, S. Zhong, B. Paviet-Salomon, M. Despeisse, Z. Liang, M. Boccard, H. Shen, and C. Ballif, *22% efficient dopant-free interdigitated back contact silicon solar cells,* in *AIP Conference Proceedings*, Vol. 1999 (AIP Publishing, 2018).

[112] G. Ma, R. Du, Y.-n. Cai, C. Shen, X. Gao, Y. Zhang, F. Liu, W. Shi, W. Du, and Y. Zhang, *Improved power conversion efficiency of silicon nanowire solar cells based on transition metal oxides,* Solar Energy Materials and Solar Cells **193**, 163 (2019).

[113] S. Marwaha and K. Ghosh, *Analysis of Silicon-perovskite Tandem Solar Cells with Transition Metal Oxides as Carrier Selective Contact Layers,* Silicon **14**, 10849 (2022).

[114] J. Li, Q.-Y. Bao, H.-X. Wei, Z.-Q. Xu, J.-P. Yang, Y.-Q. Li, S.-T. Lee, and J.-X. Tang, *Role of transition metal oxides in the charge recombination layer used in tandem organic photovoltaic cells,* Journal of Materials Chemistry **22**, 6285 (2012).

[115] Z. Tan, L. Zhang, T. Wu, B. Zhou, and X. Long, *Composition Tuned Electron Rearrangement of Transition-Metal-Based Compounds Promotes Hydrogen Generation,* The Journal of Physical Chemistry C **127**, 15747 (2023).

[116] D. Menzel, M. Mews, B. Rech, and L. Korte, *Electronic structure of indium-tungsten-oxide alloys and their energy band alignment at the heterojunction to crystalline silicon,* Applied Physics Letters **112** (2018).

[117] S. Acharyya, S. Sadhukhan, T. Panda, D. K. Ghosh, N. C. Mandal, A. Nandi, S. Bose, G. Das, S. Maity, P. Chaudhuri, *et al.*, *Dopant-free materials for carrier-selective passivating contact solar cells: A review,* Surfaces and Interfaces **28**, 101687 (2022).

[118] J. Cho, M. Debucquoy, M. R. Payo, S. Malik, M. Filipič, H. S. Radhakrishnan, T. Bearda, I. Gordon, J. Szlufcik, and J. Poortmans, *Contact resistivity reduction on lowly-doped n-type Si using a low work function metal and a thin TiO_x interfacial layer for doping-free Si solar cells,* Energy Procedia **124**, 842 (2017).

[119] Z. Yang, P. Gao, J. Sheng, H. Tong, C. Quan, X. Yang, K. W. Chee, B. Yan, Y. Zeng, and J. Ye, *Principles of dopant-free electron-selective contacts based on tunnel oxide/low work-function metal stacks and their applications in heterojunction solar cells,* Nano Energy **46**, 133 (2018).

[120] M. T. Greiner, L. Chai, M. G. Helander, W.-M. Tang, and Z.-H. Lu, *Transition metal oxide work functions: the influence of cation oxidation state and oxygen vacancies,* Advanced Functional Materials **22**, 4557 (2012).

[121] S. M. Sze, *Semiconductor devices: physics and technology* (John Wiley & Sons, 2008).

[122] A. Smets, K. Jäger, O. Isabella, R. Van Swaaij, and M. Zeman, *Solar Energy: The physics and engineering of photovoltaic conversion, technologies and systems* (Bloomsbury Publishing, 2016).

[123] S. Essig, J. Dréon, E. Rucavado, M. Mews, T. Koida, M. Boccard, J. Werner, J. Geissbühler, P. Löper, M. Morales-Masis, *et al.*, *Toward annealing-stable molybdenum-oxide-based hole-selective contacts for silicon photovoltaics,* Solar RRL **2**, 1700227 (2018).

[124] Z. Wang, J. He, W. Wang, H. Lin, Z. Xu, Q. Liu, S. Peng, J. Hou, D. He, and P. Gao, *Twenty percent efficiency crystalline silicon solar cells with solution-processed electron-selective contacts,* ACS Applied Energy Materials **4**, 3644 (2021).

[125] B. Macco, L. E. Black, J. Melskens, B. W. van de Loo, W.-J. H. Berghuis, M. A. Verheijen, and W. M. Kessels, *Atomic-layer deposited Nb_2O_5 as transparent passivating electron contact for c-Si solar cells,* Solar Energy Materials and Solar Cells **184**, 98 (2018).

[126] P. Ravindra, R. Mukherjee, and S. Avasthi, *Hole-selective electron-blocking copper oxide contact for silicon solar cells,* IEEE Journal of Photovoltaics **7**, 1278 (2017).

[127] X. Yang, Y. Lin, J. Liu, W. Liu, Q. Bi, X. Song, J. Kang, F. Xu, L. Xu, M. N. Hedhili, *et al.*, *A highly conductive titanium oxynitride electron-selective contact for efficient photovoltaic devices,* Advanced Materials **32**, 2002608 (2020).

[128] K. X. Steirer, J. P. Chesin, N. E. Widjonarko, J. J. Berry, A. Miedaner, D. S. Ginley, and D. C. Olson, *Solution deposited NiO thin-films as hole transport layers in organic photovoltaics,* Organic Electronics **11**, 1414 (2010).

[129] J. Meyer, S. Hamwi, M. Kröger, W. Kowalsky, T. Riedl, and A. Kahn, *Transition metal oxides for organic electronics: energetics, device physics and applications,* Advanced Materials **24**, 5408 (2012).

[130] L. G. Gerling, S. Mahato, C. Voz, R. Alcubilla, and J. Puigdollers, *Characterization of transition metal oxide/silicon heterojunctions for solar cell applications,* Applied Sciences **5**, 695 (2015).

[131] S. Oh, S. Jung, Y. H. Lee, J. T. Song, T. H. Kim, D. K. Nandi, S.-H. Kim, and J. Oh, *Hole-selective CoO_x/SiO_x/Si heterojunctions for photoelectrochemical water splitting,* ACS Catalysis **8**, 9755 (2018).

[132] M. Zaien, N. Ahmed, and Z. Hassan, *Fabrication and characterization of an n-CdO/p-Si solar cell by thermal evaporation in a vacuum,* International Journal of Electrochemical Science **8**, 6988 (2013).

[133] S.-H. Kim, J.-Y. Jung, R. B. Wehrspohn, and J.-H. Lee, *All-room-temperature processed 17.25%-crystalline silicon solar cell,* ACS Applied Energy Materials **3**, 3180 (2020).

[134] H. Imran, T. M. Abdolkader, and N. Z. Butt, *Carrier-selective NiO/Si and TiO 2/Si contacts for silicon heterojunction solar cells,* IEEE Transactions on Electron Devices **63**, 3584 (2016).

[135] J. Zhao, F.-J. Ma, A. Ho-Baillie, S. Bremner, *et al.*, *Spin Coated Nickel Oxide and Vanadium Oxide Layers on Silicon for a Carrier Selective Contact Solar Cell,* in *2017 IEEE 44th Photovoltaic Specialist Conference (PVSC)* (IEEE, 2017) pp. 1845–1849.

[136] W. Lin, W. Wu, J. Bao, Z. Liu, K. Qiu, L. Cai, Z. Yao, Y. Deng, Z. Liang, and H. Shen, *Novel hole selective CrOx contact for dopant-free back contact silicon solar cells,* Materials Research Bulletin **103**, 77 (2018).

[137] V.-Q. Zhuo, Y. Jiang, M. Li, E. Chua, Z. Zhang, J. Pan, R. Zhao, L. Shi, T. Chong, and J. Robertson, *Band alignment between Ta2O5 and metals for resistive random access memory electrodes engineering,* Applied Physics Letters **102** (2013).

[138] S. Ezhilvalavan and T.-Y. Tseng, *Electrical properties of Ta2O5 thin films deposited on Cu,* Thin Solid Films **360**, 268 (2000).

[139] D. Speaks, M. Mayer, K. Yu, S. Mao, E. Haller, and W. Walukiewicz, *Fermi level stabilization energy in cadmium oxide,* Journal of Applied Physics **107** (2010).

[140] L. G. Gerling, C. Voz, R. Alcubilla, and J. Puigdollers, *Origin of passivation in hole-selective transition metal oxides for crystalline silicon heterojunction solar cells,* Journal of Materials Research **32**, 260 (2017).

[141] R. Woods-Robinson, A. N. Fioretti, J. Haschke, M. Boccard, K. A. Persson, and C. Ballif, *Evaluating materials design parameters of hole-selective contacts for silicon heterojunction solar cells,* IEEE Journal of Photovoltaics **11**, 247 (2020).

[142] W. Wu, J. Bao, X. Jia, Z. Liu, L. Cai, B. Liu, J. Song, and H. Shen, *Dopant-free back contact silicon heterojunction solar cells employing transition metal oxide emitters,* Physica Status Solidi (RRL)–Rapid Research Letters **10**, 662 (2016).

[143] H. Nasser, M. Z. Borra, E. H. Çiftpınar, B. Eldeeb, and R. Turan, *Fourteen percent efficiency ultrathin silicon solar cells with improved infrared light management enabled by hole-selective transition metal oxide full-area rear passivating contacts,* Progress in Photovoltaics: Research and Applications **30**, 823 (2022).

[144] M. Bivour, J. Temmler, F. Zähringer, S. Glunz, and M. Hermle, *High work function metal oxides for the hole contact of silicon solar cells,* in *2016 IEEE 43rd Photovoltaic Specialists Conference (PVSC)* (IEEE, 2016) pp. 0215–0220.

[145] Z. Wang, P. Li, Z. Liu, J. Fan, X. Qian, J. He, S. Peng, D. He, M. Li, and P. Gao, *Hole selective materials and device structures of heterojunction solar cells: Recent assessment and future trends,* APL Materials **7** (2019).

[146] R. A. Vijayan, S. Masilamani, S. Kailasam, K. Shivam, B. Deenadhayalan, and M. Varadharajaperumal, *Study of surface passivation and charge transport barriers in DASH solar cell,* IEEE Journal of Photovoltaics **9**, 1208 (2019).

[147] P. Procel, H. Xu, A. Saez, C. Ruiz-Tobon, L. Mazzarella, Y. Zhao, C. Han, G. Yang, M. Zeman, and O. Isabella, *The role of heterointerfaces and subgap energy states on transport mechanisms in silicon heterojunction solar cells,* Progress in Photovoltaics: Research and Applications **28**, 935 (2020).

[148] Z. Liang, M. Su, Y. Zhou, L. Gong, C. Zhao, K. Chen, F. Xie, W. Zhang, J. Chen, P. Liu, *et al.*, *Interaction at the silicon/transition metal oxide heterojunction interface and its effect on the photovoltaic performance,* Physical Chemistry Chemical Physics **17**, 27409 (2015).

[149] T. Mochizuki, K. Gotoh, Y. Kurokawa, T. Yamamoto, and N. Usami, *Local Structure of High Performance TiO_x Electron-Selective Contact Revealed by Electron Energy Loss Spectroscopy,* Advanced Materials Interfaces **6**, 1801645 (2019).

[150] J. Cho, J. Melskens, M. Debucquoy, M. Recamán Payo, S. Jambaldinni, T. Bearda, I. Gordon, J. Szlufcik, W. Kessels, and J. Poortmans, *Passivating electron-selective contacts for silicon solar cells based on an a-Si:H/TiO_x stack and a low work function metal,* Progress in Photovoltaics: Research and Applications **26**, 835 (2018).

[151] J. Cho, M. Debucquoy, M. R. Payo, E. Schapmans, I. Gordon, J. Szlufcik, and J. Poortmans, *Evidence of TiO_x reduction at the SiO_x/TiO_x interface of passivating electron-selective contacts,* in *AIP Conference Proceedings*, Vol. 1999 (AIP Publishing, 2018).

[152] T. Matsui, M. Bivour, P. F. Ndione, R. S. Bonilla, and M. Hermle, *Origin of the tunable carrier selectivity of atomic-layer-deposited TiO_x nanolayers in crystalline silicon solar cells,* Solar Energy Materials and Solar Cells **209**, 110461 (2020).

[153] J. Schmidt, R. Peibst, and R. Brendel, *Surface passivation of crystalline silicon solar cells: Present and future,* Solar Energy Materials and Solar Cells **187**, 39 (2018).

[154] M. A. Hossain and B. Hoex, *Update on Non-silicon-based Low-Temperature Passivating Contacts for Silicon Solar Cells,* Photovoltaic Solar Energy: From Fundamentals to Applications **2**, 81 (2024).

[155] M. Nayak, A. Pandey, S. Mandal, and V. K. Komarala, *Nickel oxide-based hole-selective contact silicon heterojunction solar cells,* in *AIP Conference Proceedings*, Vol. 2487 (AIP Publishing, 2022).

[156] S. Boudour, I. Bouchama, M. Hadjab, and S. Laidoudi, *Optimization of defected ZnO/Si/Cu_2O_x heterostructure solar cell,* Optical Materials **98**, 109433 (2019).

[157] L. Black, B. Van De Loo, B. Macco, J. Melskens, W. Berghuis, and W. Kessels, *Explorative studies of novel silicon surface passivation materials: Considerations and lessons learned,* Solar Energy Materials and Solar Cells **188**, 182 (2018).

[158] Y. Jiang, S. Cao, L. Lu, G. Du, Y. Lin, J. Wang, L. Yang, W. Zhu, and D. Li, *Post-annealing effect on optical and electronic properties of thermally evaporated MoO_x thin films as hole-selective contacts for p-Si solar cells,* Nanoscale research letters **16**, 87 (2021).

[159] T. Zhang, C.-Y. Lee, B. Gong, and B. Hoex, *Thermal stability analysis of WO_x and MoO_x as hole-selective contacts for Si solar cells using in situ XPS,* AIP Conference Proceedings **1999**, 040027 (2018).

[160] G. Du, L. Li, X. Yang, X. Zhou, Z. Su, P. Cheng, Y. Lin, L. Lu, J. Wang, L. Yang, *et al.*, *Improved V_2O_x passivating contact for p-type crystalline silicon solar cells by oxygen vacancy modulation with a SiO_x tunnel layer,* Advanced Materials Interfaces **8**, 2100989 (2021).

[161] K. Gao, Q. Bi, X. Wang, W. Liu, C. Xing, K. Li, D. Xu, Z. Su, C. Zhang, J. Yu, *et al.*, *Progress and future prospects of wide-bandgap metal-compound-based passivating contacts for silicon solar cells,* Advanced Materials **34**, 2200344 (2022).

[162] M. T. Greiner, M. G. Helander, W.-M. Tang, Z.-B. Wang, J. Qiu, and Z.-H. Lu, *Universal energy-level alignment of molecules on metal oxides,* Nature materials **11**, 76 (2012).

[163] A. Pergament and G. Stefanovich, *Phase composition of anodic oxide films on transition metals: a thermodynamic approach,* Thin Solid Films **322**, 33 (1998).

[164] M. T. Greiner, L. Chai, M. G. Helander, W.-M. Tang, and Z.-H. Lu, *Metal/metal-oxide interfaces: how metal contacts affect the work function and band structure of MoO_3,* Advanced Functional Materials **23**, 215 (2013).

[165] M. V. Ganduglia-Pirovano, A. Hofmann, and J. Sauer, *Oxygen vacancies in transition metal and rare earth oxides: Current state of understanding and remaining challenges,* Surface Science Reports **62**, 219 (2007).

[166] M. T. Greiner and Z.-H. Lu, *Thin-film metal oxides in organic semiconductor devices: their electronic structures, work functions and interfaces,* NPG Asia Materials **5**, e55 (2013).

[167] J. Tong, T. T. Le, W. Liang, M. A. Hossain, K. R. McIntosh, P. Narangari, S. Armand, T. C. Kho, K. T. Khoo, Y. Zakaria, *et al.*, *Impact of Pregrown SiO_x on the Carrier Selectivity and Thermal Stability of Molybdenum-Oxide-Passivated Contact for Si Solar Cells,* ACS Applied Materials & Interfaces **13**, 36426 (2021).

[168] L. Li, G. Du, Y. Lin, X. Zhou, Z. Gu, L. Lu, W. Liu, J. Huang, J. Wang, L. Yang, *et al.*, *NiO_x/MoO_x bilayer as an efficient hole-selective contact in crystalline silicon solar cells,* Cell Reports Physical Science **2** (2021).

[169] M. M. Makhlouf and M. Shehata, *Multilayer emitter of molybdenum oxide/silver/molybdenum oxide thin films for silicon heterojunction solar cells: Device fabrication and electrical characterization,* Journal of Alloys and Compounds **904**, 164102 (2022).

[170] O. Akdemir, M. Zolfaghari Borra, H. Nasser, R. Turan, and A. Bek, *MoO_x/Ag/MoO_x multilayers as hole transport transparent conductive electrodes for n-type crystalline silicon solar cells,* International Journal of Energy Research **44**, 3098 (2020).

[171] E. Horynová, O. Romanyuk, L. Horák, Z. Remeš, B. Conrad, A. Peter Amalathas, L. Landová, J. Houdková, P. Jiříček, T. Finsterle, *et al.*, *Optical characterization of low temperature amorphous MoO_x, WO_x, and VO_x prepared by pulsed laser deposition,* Thin Solid Films **693**, 137690 (2020).

[172] M. Kumar, E.-C. Cho, M. F. Prodanov, C. Kang, A. K. Srivastava, and J. Yi, *MoO_x work function, interface structure, and thermal stability analysis of ITO/MoO_x/a-Si (i) stacks for hole-selective silicon heterojunction solar cells,* Applied Surface Science **553**, 149552 (2021).

[173] R. Singh, R. Sivakumar, S. Srivastava, and T. Som, *Growth angle-dependent tunable work function and optoelectronic properties of MoO_x thin films,* Applied Surface Science **507**, 144958 (2020).

[174] D. O. Scanlon, G. W. Watson, D. Payne, G. Atkinson, R. Egdell, and D. Law, *Theoretical and experimental study of the electronic structures of MoO_3 and MoO_2,* The Journal of Physical Chemistry C **114**, 4636 (2010).

[175] K. Inzani, T. Grande, F. Vullum-Bruer, and S. M. Selbach, *A van der Waals density functional study of MoO_3 and its oxygen vacancies,* The Journal of Physical Chemistry C **120**, 8959 (2016).

[176] O. Y. Khyzhun, *XPS, XES and XAS studies of the electronic structure of tungsten oxides,* Journal of Alloys and Compounds **305**, 1 (2000).

[177] C. Wu, F. Feng, and Y. Xie, *Design of vanadium oxide structures with controllable electrical properties for energy applications,* Chemical Society Reviews **42**, 5157 (2013).

[178] L. Lajaunie, F. Boucher, R. Dessapt, and P. Moreau, *Strong anisotropic influence of local-field effects on the dielectric response of α-MoO_3,* Physical Review B—Condensed Matter and Materials Physics **88**, 115141 (2013).

[179] L. Gao, F. Lemarchand, and M. Lequime, *Exploitation of multiple incidences spectrometric measurements for thin film reverse engineering,* Optics Express **20**, 15734 (2012).

[180] L. V. Rodríguez-de Marcos, J. I. Larruquert, J. A. Méndez, and J. A. Aznárez, *Self-consistent optical constants of SiO_2 and Ta_2O_5 films,* Optical Materials Express **6**, 3622 (2016).

[181] S. Sarkar, V. Gupta, M. Kumar, J. Schubert, P. T. Probst, J. Joseph, and T. A. Konig, *Hybridized guided-mode resonances via colloidal plasmonic self-assembled grating,* ACS applied materials & interfaces **11**, 13752 (2019).

[182] D. P. Kulikova, A. A. Dobronosova, V. V. Kornienko, I. A. Nechepurenko, A. S. Baburin, E. V. Sergeev, E. S. Lotkov, I. A. Rodionov, A. V. Baryshev, and A. V. Dorofeenko, *Optical properties of tungsten trioxide, palladium, and platinum thin films for functional nanostructures engineering,* Optics Express **28**, 32049 (2020).

[183] C. Stelling, C. R. Singh, M. Karg, T. A. König, M. Thelakkat, and M. Retsch, *Plasmonic nanomeshes: their ambivalent role as transparent electrodes in organic solar cells,* Scientific Reports **7**, 42530 (2017).

[184] C. Messmer, M. Bivour, J. Schön, S. W. Glunz, and M. Hermle, *Numerical simulation of silicon heterojunction solar cells featuring metal oxides as carrier-selective contacts,* IEEE Journal of Photovoltaics **8**, 456 (2018).

[185] J. Werner, J. Geissbuhler, A. Dabirian, S. Nicolay, M. Morales-Masis, S. D. Wolf, B. Niesen, and C. Ballif, *Parasitic absorption reduction in metal oxide-based transparent electrodes: application in perovskite solar cells,* ACS applied materials & interfaces **8**, 17260 (2016).

[186] G. S. Jeong, Y.-C. Jung, N. Y. Park, Y.-J. Yu, J. H. Lee, J. H. Seo, and J.-Y. Choi, *Stoichiometry and morphology analysis of thermally deposited V_2O_{5-x} thin films for Si/V_2O_{5-x} heterojunction solar cell applications,* Materials **15**, 5243 (2022).

[187] B. Hichwa and G. Caskey, *Comparison of film density, stoichiometry, optical and electrical properties of thin metal oxide films produced by reactive dc magnetron sputtering and electron beam evaporation techniques,* Surface and Coatings Technology **33**, 393 (1987).

[188] X. Ru, M. Qu, J. Wang, T. Ruan, M. Yang, F. Peng, W. Long, K. Zheng, H. Yan, and X. Xu, *25.11% efficiency silicon heterojunction solar cell with low deposition rate intrinsic amorphous silicon buffer layers,* Solar Energy Materials and Solar Cells **215**, 110643 (2020).

[189] T. Pan, J. Li, Y. Lin, Z. Xue, Z. Di, M. Yin, J. Wang, L. Lu, L. Yang, and D. Li, *Structural and optical studies of molybdenum oxides thin films obtained by thermal evaporation and atomic layer deposition methods for photovoltaic application,* Journal of Materials Science: Materials in Electronics **32**, 3475 (2021).

[190] D. J. Borah, A. Mostako, P. Saikia, and P. Dutta, *Effect of thickness and post deposition annealing temperature on the structural and optical properties of thermally evaporated molybdenum oxide films,* Materials Science in Semiconductor Processing **93**, 111 (2019).

[191] G. Dong, J. Sang, C.-W. Peng, F. Liu, Y. Zhou, and C. Yu, *Power conversion efficiency of 25.26% for silicon heterojunction solar cell with transition metal element doped indium oxide transparent conductive film as front electrode,* Progress in Photovoltaics: Research and Applications **30**, 1136 (2022).

[192] M. Diskus, O. Nilsen, H. Fjellvåg, S. Diplas, P. Beato, C. Harvey, E. van Schrojenstein Lantman, and B. M. Weckhuysen, *Combination of characterization techniques for atomic layer deposition MoO_3 coatings: From the amorphous to the orthorhombic α-MoO_3 crystalline phase,* Journal of Vacuum Science & Technology A **30** (2012).

[193] S. Bhatia, I. M. Khorakiwala, P. R. Nair, and A. Antony, *Influence of post deposition fabrication steps and quantitative estimation of band diagram of Si/MoO_x heterojunction for carrier selective solar cells,* Solar Energy **194**, 141 (2019).

[194] I. Irfan and Y. Gao, *Effects of exposure and air annealing on MoO_x thin films,* Journal of Photonics for Energy **2**, 021213 (2012).

[195] D. Scirè, P. Procel, A. Gulino, O. Isabella, M. Zeman, and I. Crupi, *Sub-gap defect density characterization of molybdenum oxide: An annealing study for solar cell applications,* Nano Research **13**, 3416 (2020).

[196] T. Wang, G. Yu, Y. Wei, W. Liu, W. Fu, Y. Lin, X. Wu, L. Xu, P. Lin, X. Yu, *et al.*, *Solution-processed vanadium oxide by low-temperature annealing for silicon solar cells with hole selective contact,* Materials Science in Semiconductor Processing **165**, 107638 (2023).

[197] T. Kamioka, Y. Hayashi, Y. Isogai, K. Nakamura, and Y. Ohshita, *Effects of annealing temperature on workfunction of MoO_x at MoO_x/SiO_2 interface and process-induced damage in indium tin oxide/MoO_x/SiO_x/Si stack,* Japanese Journal of Applied Physics **57**, 076501 (2018).

[198] A. H. T. Le, J. Dréon, J. I. Michel, M. Boccard, J. Bullock, N. Borojevic, and Z. Hameiri, *Temperature-dependent performance of silicon heterojunction solar cells with transition-metal-oxide-based selective contacts,* Progress in Photovoltaics: Research and Applications **30**, 981 (2022).

[199] O. Almora, L. G. Gerling, C. Voz, R. Alcubilla, J. Puigdollers, and G. Garcia-Belmonte, *Superior performance of V_2O_5 as hole selective contact over other transition metal oxides in silicon heterojunction solar cells,* Solar Energy Materials and Solar Cells **168**, 221 (2017).

[200] M. Jeong, J. Park, Y. J. Cho, and H. S. Chang, *Improved passivation performance of Al_2O_3 interlayer/MoO_x thin films continuously grown via atomic layer deposition,* Thin Solid Films **766**, 139667 (2023).

[201] J.-O. Carlsson and P. M. Martin, *Chemical vapor deposition,* in *Handbook of Deposition Technologies for films and coatings* (Elsevier, 2010) pp. 314–363.

[202] Y. Kim, S. Kwon, E.-J. Seo, J. H. Nam, H. Y. Jang, S.-H. Kwon, J.-D. Kwon, D.-W. Kim, and B. Cho, *Facile fabrication of a two-dimensional TMD/Si heterojunction photodiode by atmospheric-pressure plasma-enhanced chemical vapor deposition,* ACS applied materials & interfaces **10**, 36136 (2018).

[203] K.-E. Elers, T. Blomberg, M. Peussa, B. Aitchison, S. Haukka, and S. Marcus, *Film uniformity in atomic layer deposition,* Chemical Vapor Deposition **12**, 13 (2006).

[204] E. R. Costals, G. Masmitjà, E. Almache, B. Pusay, K. Tiwari, E. Saucedo, C. J. Raj, B. C. Kim, J. Puigdollers, I. Martin, *et al.*, *Atomic layer deposition of vanadium oxide films for crystalline silicon solar cells,* Materials advances **3**, 337 (2022).

[205] M. Tyona, *A theoritical study on spin coating technique,* Advances in materials Research **2**, 195 (2013).

[206] F. Li, Z. Sun, Y. Zhou, Q. Wang, Q. Zhang, G. Dong, F. Liu, Z. Fan, Z. Liu, Z. Cai, *et al.*, *Lithography-free and dopant-free back-contact silicon heterojunction solar cells with solution-processed TiO2 as the efficient electron selective layer,* Solar Energy Materials and Solar Cells **203**, 110196 (2019).

[207] N. Beyraghi, M. C. Sahiner, O. Oguz, and S. Yerci, *Optimization of a Solution-Processed TiO_x/(n) c-Si Electron-Selective Interface by Pre-and Postdeposition Treatments,* ACS Applied Materials & Interfaces **16**, 16950 (2024).

[208] L. Cao, N. Yang, S. Li, X. Ye, X. Yuan, H. Li, and H. Tong, *Alumina film deposited by spin-coating method for silicon wafer surface passivation,* Journal of Materials Science: Materials in Electronics **31**, 2686 (2020).

[209] F. Li, Y. Zhou, Y. Yang, G. Dong, Y. Zhou, F. Liu, and D. Yu, *Silicon heterojunction solar cells with MoO_x hole-selective layer by hot wire oxidation–sublimation deposition,* Solar RRL **4**, 1900514 (2020).

[210] S. Li, Z. Tang, J. Xue, G. Jianjun, Z. Shi, and X. Li, *Comparative study on front emitter and rear emitter n-type silicon heterojunction solar cells: The role of folded electrical fields,* Vacuum **149**, 313 (2018).

[211] A. Richter, M. Hermle, and S. W. Glunz, *Reassessment of the limiting efficiency for crystalline silicon solar cells,* IEEE Journal of Photovoltaics **3**, 1184 (2013).

[212] Y. Zhao, P. Procel, C. Han, L. Cao, G. Yang, E. Özkol, A. Alcañiz, K. Kovačević, G. Limodio, R. Santbergen, *et al.*, *Strategies for realizing high-efficiency silicon heterojunction solar cells,* Solar Energy Materials and Solar Cells **258**, 112413 (2023).

[213] M. Bivour, S. Schröer, M. Hermle, and S. W. Glunz, *Silicon heterojunction rear emitter solar cells: Less restrictions on the optoelectrical properties of front side TCOs,* Solar Energy Materials and Solar Cells **122**, 120 (2014).

[214] M. Q. Khokhar, S. Hussain, S. Kim, S. Lee, D. Pham, Y. Kim, E. Cho, and J. Yi, *Review of Rear Emitter Silicon Heterojunction Solar Cells,* Transactions on Electrical and Electronic Materials **21**, 138 (2020).

[215] J. Bullock, Y. Wan, Z. Xu, S. Essig, M. Hettick, H. Wang, W. Ji, M. Boccard, A. Cuevas, C. Ballif, *et al.*, *Stable dopant-free asymmetric heterocontact silicon solar cells with efficiencies above 20%,* ACS Energy Letters **3**, 508 (2018).

[216] M. Mews, A. Lemaire, and L. Korte, *Sputtered Tungsten Oxide as Hole Contact for Silicon Heterojunction Solar Cells,* IEEE Journal of Photovoltaics **7**, 1209 (2017).

[217] S. Yamaguchi, C. Yamamoto, K. Ohdaira, and A. Masuda, *Comprehensive study of potential-induced degradation in silicon heterojunction photovoltaic cell modules,* Progress in Photovoltaics: Research and Applications **26**, 697 (2018).

[218] J. Cattin, L.-L. Senaud, J. Haschke, B. Paviet-Salomon, M. Despeisse, C. Ballif, and M. Boccard, *Influence of light soaking on silicon heterojunction solar cells with various architectures,* IEEE Journal of Photovoltaics **11**, 575 (2021).

[219] A. H. T. Le, R. S. Bonilla, L. E. Black, J. P. Seif, T. G. Allen, R. Dumbrell, C. Samundsett, and Z. Hameiri, *Recombination in passivating contacts: investigation into the impact of the contact work function on the obtained passivation,* Solar RRL **7**, 2201050 (2023).

[220] C. Ballif, F.-J. Haug, M. Boccard, P. J. Verlinden, and G. Hahn, *Status and perspectives of crystalline silicon photovoltaics in research and industry,* Nature Reviews Materials **7**, 597 (2022).

[221] J. Shi, L. Shen, Y. Liu, J. Yu, J. Liu, L. Zhang, Y. Liu, J. Bian, Z. Liu, and F. Meng, *MoO_x modified ITO/a-Si:H (p) contact for silicon heterojunction solar cell application,* Materials Research Bulletin **97**, 176 (2018).

[222] J. Peter Seif, A. Descoeudres, M. Filipič, F. Smole, M. Topič, Z. Charles Holman, S. De Wolf, and C. Ballif, *Amorphous silicon oxide window layers for high-efficiency silicon heterojunction solar cells,* Journal of Applied Physics **115**, 024502 (2014).

[223] Y. Zhong, M. Huang, H. Ma, W. Dong, Y. Wang, and N. Zhao, *In situ study on Cu–Ni cross-interaction in Cu/Sn/Ni solder joints under temperature gradient,* Journal of Materials Research **31**, 609 (2016).

[224] H. Ali, S. Koul, G. Gregory, J. Bullock, A. Javey, A. Kushima, and K. O. Davis, *In situ transmission electron microscopy study of molybdenum oxide contacts for silicon solar cells,* Physica Status Solidi (a) **216**, 1800998 (2019).

[225] L. Mazzarella, A. Alcañiz, P. Procel, E. Kawa, Y. Zhao, U. Tiringer, C. Han, G. Yang, P. Taheri, M. Zeman, *et al., Strategy to mitigate the dipole interfacial states in (i) a-Si:H/MoO_x passivating contacts solar cells,* Progress in Photovoltaics: Research and Applications **29**, 391 (2021).

[226] J. J. Jasieniak, J. Seifter, J. Jo, T. Mates, and A. J. Heeger, *A solution-processed MoO_x anode interlayer for use within organic photovoltaic devices,* Advanced Functional Materials **22**, 2594 (2012).

[227] B. Macco, M. Vos, N. Thissen, A. Bol, and W. Kessels, *Low-temperature atomic layer deposition of MoO_x for silicon heterojunction solar cells,* Physica Status Solidi (RRL)–Rapid Research Letters **9**, 393 (2015).

[228] J. Tong, Y. Wan, J. Cui, S. Lim, N. Song, and A. Lennon, *Solution-processed molybdenum oxide for hole-selective contacts on crystalline silicon solar cells,* Applied Surface Science **423**, 139 (2017).

[229] F. Wang, S. Zhao, B. Liu, Y. Li, Q. Ren, R. Du, N. Wang, C. Wei, X. Chen, G. Wang, *et al., Silicon solar cells with bifacial metal oxides carrier selective layers,* Nano Energy **39**, 437 (2017).

[230] L. Neusel, M. Bivour, and M. Hermle, *Selectivity issues of MoO_x based hole contacts,* Energy Procedia **124**, 425 (2017).

[231] T. Zhang, C.-Y. Lee, Y. Wan, S. Lim, and B. Hoex, *Investigation of the thermal stability of MoO_x as hole-selective contacts for Si solar cells,* Journal of Applied Physics **124**, 073106 (2018).

[232] J. Cho, N. Nawal, A. Hadipour, M. R. Payo, A. van der Heide, H. S. Radhakrishnan, M. Debucquoy, I. Gordon, J. Szlufcik, and J. Poortmans, *Interface analysis and intrinsic thermal stability of MoO_x based hole-selective contacts for silicon heterojunction solar cells,* Solar Energy Materials and Solar Cells **201**, 110074 (2019).

[233] D. Sacchetto, Q. Jeangros, G. Christmann, L. Barraud, A. Descoeudres, J. Geissbühler, M. Despeisse, A. Hessler-Wyser, S. Nicolay, and C. Ballif, *ITO/MoO_x/a-Si:H (i) hole-selective contacts for silicon heterojunction solar cells: degradation mechanisms and cell integration,* IEEE Journal of Photovoltaics **7**, 1584 (2017).

[234] S. Cao, J. Li, J. Zhang, Y. Lin, L. Lu, J. Wang, M. Yin, L. Yang, X. Chen, and D. Li, *Stable MoO_x-Based Heterocontacts for p-Type Crystalline Silicon Solar Cells Achieving 20% Efficiency,* Advanced Functional Materials **30**, 2004367 (2020).

[235] G. Yang, C. Han, P. Procel, Y. Zhao, M. Singh, L. Mazzarella, M. Zeman, and O. Isabella, *Oxygen-alloyed poly-Si passivating contacts for high-thermal budget c-Si heterojunction solar cells,* Progress in Photovoltaics: Research and Applications **30**, 141 (2022).

[236] Y. Zhao, L. Mazzarella, P. Procel, C. Han, F. D. Tichelaar, G. Yang, A. Weeber, M. Zeman, and O. Isabella, *Ultra-thin electron collectors based on nc-Si: H for high-efficiency silicon heterojunction solar cells,* Progress in Photovoltaics: Research and Applications **30**, 809 (2022).

[237] Y. Zhao, L. Mazzarella, P. Procel, C. Han, G. Yang, A. Weeber, M. Zeman, and O. Isabella, *Doped hydrogenated nanocrystalline silicon oxide layers for high-efficiency c-Si heterojunction solar cells,* Progress in Photovoltaics: Research and Applications **28**, 425 (2020).

[238] Y. Zhao, L. Mazzarella, P. Procel, C. Han, G. Yang, A. Weeber, M. Zeman, and O. Isabella, *Effects of (i)a-Si:H deposition temperature on high-efficiency silicon heterojunction solar cells,* Progress in Photovoltaics: Research and Applications **under review** (2022).

[239] C. Han, Y. Zhao, L. Mazzarella, R. Santbergen, A. Montes, P. Procel, G. Yang, X. Zhang, M. Zeman, and O. Isabella, *Room-temperature sputtered tungsten-doped indium oxide for improved current in silicon heterojunction solar cells,* Solar Energy Materials and Solar Cells **227**, 111082 (2021).

[240] G. Limodio, Y. De Groot, G. Van Kuler, L. Mazzarella, Y. Zhao, P. Procel, G. Yang, O. Isabella, and M. Zeman, *Copper-plating metallization with alternative seed layers for c-si solar cells embedding carrier-selective passivating contacts,* IEEE Journal of Photovoltaics **10**, 372 (2019).

[241] C. Han, G. Yang, P. Procel, D. O'Connor, Y. Zhao, A. Gopalakrishnan, X. Zhang, M. Zeman, L. Mazzarella, and O. Isabella, *Controllable Simultaneous Bifacial Cu-Plating for High-Efficiency Crystalline Silicon Solar Cells,* Solar RRL **6**, 2100810 (2022).

[242] E. Özkol, P. Wagner, F. Ruske, B. Stannowski, and L. Korte, *Optimization of Silicon Heterojunction Interface Passivation on p-and n-Type Wafers Using Optical Emission Spectroscopy,* Physica Status Solidi (a) **219**, 2100511 (2022).

[243] E. Zhu, Y. Li, C.-Y. Chiu, X. Huang, M. Li, Z. Zhao, Y. Liu, X. Duan, and Y. Huang, *In situ development of highly concave and composition-confined PtNi octahedra with high oxygen reduction reaction activity and durability,* Nano Research **9**, 149 (2016).

[244] T. Sun, R. Wang, R. Liu, C. Wu, Y. Zhong, Y. Liu, Y. Wang, Y. Han, Z. Xia, Y. Zou, *et al.*, *Investigation of MoO_x/n-Si strong inversion layer interfaces via dopant-free hetero-contact,* Physica Status Solidi (RRL)–Rapid Research Letters **11**, 1700107 (2017).

[245] G. Andersson, A. Magneli, L. Sillén, and M. Rottenberg, *On the crystal structure of molybdenum trioxide,* Acta Chem. Scand **4**, 793 (1950).

[246] I. A. De Castro, R. S. Datta, J. Z. Ou, A. Castellanos-Gomez, S. Sriram, T. Daeneke, and K. Kalantar-zadeh, *Molybdenum oxides–from fundamentals to functionality,* Advanced Materials **29**, 1701619 (2017).

[247] T. Hom, W. Kiszenik, and B. Post, *Accurate lattice constants from multiple reflection measurements. II. Lattice constants of germanium silicon, and diamond,* Journal of Applied Crystallography **8**, 457 (1975).

[248] D. A. Neamen, *Semiconductor physics and devices: basic principles* (McGraw-hill, 2003).

[249] C. He, *Work function of (0 0 1) and (0 0 -1) surface of α-Fe_2O_3,* Modern Physics Letters B **32**, 1850188 (2018).

[250] B. Höffling, *The interfaces between silicon and transparent conducting oxides*, Ph.D. thesis, Jena, Friedrich-Schiller-Universität Jena, Diss., 2015 (2015).

[251] S. D. U. Guide, *Sentaurus Device User Guide,* CA, USA: Synopsys Inc (2013).

[252] R. Santbergen, T. Meguro, T. Suezaki, G. Koizumi, K. Yamamoto, and M. Zeman, *GenPro4 optical model for solar cell simulation and its application to multijunction solar cells,* IEEE Journal of Photovoltaics **7**, 919 (2017).

[253] P. Procel, G. Yang, O. Isabella, and M. Zeman, *Theoretical evaluation of contact stack for high efficiency IBC-SHJ solar cells,* Solar Energy Materials and Solar Cells **186**, 66 (2018).

[254] U. Würfel, M. Seßler, M. Unmüssig, N. Hofmann, M. List, E. Mankel, T. Mayer, G. Reiter, J.-L. Bubendorff, L. Simon, *et al.*, *How molecules with dipole moments enhance the selectivity of electrodes in organic solar cells–a combined experimental and theoretical approach,* Advanced Energy Materials **6**, 1600594 (2016).

[255] J. Bisquert, *Nanostructured energy devices: equilibrium concepts and kinetics* (Crc Press, 2014).

[256] A. L. Cauduro, R. Dos Reis, G. Chen, A. K. Schmid, H.-G. Rubahn, and M. Madsen, *Work function mapping of MoO_x thin-films for application in electronic devices,* Ultramicroscopy **183**, 99 (2017).

[257] Irfan, H. Ding, Y. Gao, C. Small, D. Y. Kim, J. Subbiah, and F. So, *Energy level evolution of air and oxygen exposed molybdenum trioxide films,* Applied Physics Letters **96**, 116 (2010).

[258] I. Irfan, A. James Turinske, Z. Bao, and Y. Gao, *Work function recovery of air exposed molybdenum oxide thin films,* Applied Physics Letters **101**, 093305 (2012).

[259] Z. Zhang, Y. Xiao, H.-X. Wei, G.-F. Ma, S. Duhm, Y.-Q. Li, and J.-X. Tang, *Impact of oxygen vacancy on energy-level alignment at MoO_x/organic interfaces,* Applied Physics Express **6**, 095701 (2013).

[260] F. He, X. Yin, J. Li, S. Lin, L. Wu, X. Hao, J. Zhang, and L. Feng, *Characterization of sputtered MoO_x thin films with different oxygen content and their application as back contact in CdTe solar cells,* Vacuum **176**, 109337 (2020).

[261] T. Mueller, J. Ge, M. Tang, J. Wong, Z. P. Ling, Z. Zhang, M. Doerr, T. Dippell, O. Hohn, M. Huber, *et al.*, *Inductively coupled plasma deposited amorphous silicon alloys using industrial equipment for heterojunction silicon solar cells,* in *2014 IEEE 40th Photovoltaic Specialist Conference (PVSC)* (IEEE, 2014) pp. 0625–0628.

[262] C. W. Hand and L. K. Derr, *Reaction of oxygen atoms with diborane,* Inorganic Chemistry **13**, 339 (1974).

[263] B. Terheiden, *CVD Boron Containing Glasses–An Attractive Alternative Diffusion Source for High Quality Emitters and Simplified Processing-A Review,* Energy Procedia **92**, 486 (2016).

[264] Z. Wu, W. Duan, A. Lambertz, D. Qiu, M. Pomaska, Z. Yao, U. Rau, L. Zhang, Z. Liu, and K. Ding, *Low-resistivity p-type a-Si:H/AZO hole contact in high-efficiency silicon heterojunction solar cells,* Applied Surface Science **542**, 148749 (2021).

[265] Q. Tang, W. Duan, A. Lambertz, K. Bittkau, M. A. Yaqin, Y. Zhao, K. Zhang, Q. Yang, D. Qiu, F. Gunkel, *et al.*, *> 85% indium reduction for high-efficiency silicon heterojunction solar cells with aluminum-doped zinc oxide contacts,* Solar Energy Materials and Solar Cells **251**, 112120 (2023).

[266] A. B. Morales-Vilches, A. Cruz, S. Pingel, S. Neubert, L. Mazzarella, D. Meza, L. Korte, R. Schlatmann, and B. Stannowski, *ITO-free silicon heterojunction solar cells with ZnO: Al/SiO 2 front electrodes reaching a conversion efficiency of 23%,* IEEE Journal of Photovoltaics **9**, 34 (2018).

[267] A. Cruz, E.-C. Wang, A. B. Morales-Vilches, D. Meza, S. Neubert, B. Szyszka, R. Schlatmann, and B. Stannowski, *Effect of front TCO on the performance of rear-junction silicon heterojunction solar cells: Insights from simulations and experiments,* Solar Energy Materials and Solar Cells **195**, 339 (2019).

[268] D. Greiner, S. Gledhill, C. Köble, J. Krammer, and R. Klenk, *Damp heat stability of Al-doped zinc oxide films on smooth and rough substrates,* Thin Solid Films **520**, 1285 (2011).

[269] J. I. Kim, W. Lee, T. Hwang, J. Kim, S.-Y. Lee, S. Kang, H. Choi, S. Hong, H. H. Park, T. Moon, *et al.*, *Quantitative analyses of damp-heat-induced degradation in transparent conducting oxides,* Solar Energy Materials and Solar Cells **122**, 282 (2014).

[270] S. Li, M. Pomaska, A. Lambertz, W. Duan, K. Bittkau, D. Qiu, Z. Yao, M. Luysberg, P. Steuter, M. Köhler, *et al.*, *Transparent-conductive-oxide-free front contacts for high-efficiency silicon heterojunction solar cells,* Joule **5**, 1535 (2021).

[271] J. He, G. Wang, Y. Qiu, Z. Tang, F. Ye, C. Zhang, S. Wang, L. Cai, T. Yu, and P. Gao, *Enabling transparent-conductive-oxide free efficient heterojunction solar cells by flexibly using dopant-free contact,* Advanced Functional Materials **32**, 2205901 (2022).

[272] P. Wagner, A. Cruz, J.-C. Stang, and L. Korte, *Low-resistance hole contact stacks for interdigitated rear-contact silicon heterojunction solar cells,* IEEE Journal of Photovoltaics **11**, 914 (2021).

[273] Z. C. Holman, A. Descoeudres, S. De Wolf, and C. Ballif, *Record infrared internal quantum efficiency in silicon heterojunction solar cells with dielectric/metal rear reflectors,* IEEE Journal of Photovoltaics **3**, 1243 (2013).

[274] A. Cruz, D. Erfurt, P. Wagner, A. B. Morales-Vilches, F. Ruske, R. Schlatmann, and B. Stannowski, *Optoelectrical analysis of TCO+ Silicon oxide double layers at the front and rear side of silicon heterojunction solar cells,* Solar Energy Materials and Solar Cells **236**, 111493 (2022).

[275] T. S. Liang, M. Pravettoni, C. Deline, J. S. Stein, R. Kopecek, J. P. Singh, W. Luo, Y. Wang, A. G. Aberle, and Y. S. Khoo, *A review of crystalline silicon bifacial photovoltaic performance characterisation and simulation,* Energy & Environmental Science **12**, 116 (2019).

[276] L. Mazzarella, A. Morales-Vilches, L. Korte, R. Schlatmann, and B. Stannowski, *Ultra-thin nanocrystalline n-type silicon oxide front contact layers for rear-emitter silicon heterojunction solar cells,* Solar Energy Materials and Solar Cells **179**, 386 (2018).

[277] A. Richter, V. Smirnov, A. Lambertz, K. Nomoto, K. Welter, and K. Ding, *Versatility of doped nanocrystalline silicon oxide for applications in silicon thin-film and heterojunction solar cells,* Solar Energy Materials and Solar Cells **174**, 196 (2018).

[278] L. Mazzarella, S. Kirner, B. Stannowski, L. Korte, B. Rech, and R. Schlatmann, *p-type microcrystalline silicon oxide emitter for silicon heterojunction solar cells allowing current densities above 40 mA/cm2,* Applied Physics Letters **106** (2015).

[279] R. Martins, A. Macarico, I. Ferreira, R. Nunes, A. Bicho, and E. Fortunato, *Highly conductive and highly transparent n-type microcrystalline silicon thin films,* Thin Solid Films **303**, 47 (1997).

[280] Y. Yang, W. Liu, L. Zhang, S. Huang, X. Li, K. Jiang, Z. Li, Z. Yan, S. Lan, X. Wu, *et al.*, *N-type nc-SiO$_x$: H film enables efficient and stable silicon heterojunction solar cells in sodium environment,* Materials Letters **309**, 131360 (2022).

[281] R. A. Afre, N. Sharma, M. Sharon, and M. Sharon, *Transparent conducting oxide films for various applications: A review,* Reviews on Advanced Materials Science **53**, 79 (2018).

[282] R. K. Gupta, K. Ghosh, and P. Kahol, *Thickness dependence of optoelectrical properties of tungsten-doped indium oxide films,* Applied Surface Science **255**, 8926 (2009).

[283] T. Yamamoto, H. Song, and H. Makino, *Effects of grain boundary scattering on carrier transport of highly transparent conductive Ga-doped ZnO polycrystalline films,* Physica Status Solidi (c) **10**, 603 (2013).

[284] L. Yan and R. Schropp, *Changes in the structural and electrical properties of vacuum post-annealed tungsten-and titanium-doped indium oxide films deposited by radio frequency magnetron sputtering,* Thin Solid Films **520**, 2096 (2012).

[285] J. Shi, L. Shen, F. Meng, and Z. Liu, *Structural, electrical and optical properties of highly crystalline indium tin oxide films fabricated by RPD at room temperature,* Materials Letters **182**, 32 (2016).

[286] S. Huang, W. Liu, X. Li, Z. Li, Z. Wu, W. Huang, Y. Yang, K. Jiang, J. Shi, L. Zhang, *et al.*, *Prolonged annealing improves hole transport of silicon heterojunction solar cells,* Physica Status Solidi (RRL)–Rapid Research Letters **15**, 2100015 (2021).

[287] Y. Furubayashi, M. Maehara, and T. Yamamoto, *Factors limiting carrier transport of ultrathin W-doped In2O3 films,* Journal of Physics D: Applied Physics **53**, 375103 (2020).

[288] Y. Shigesato, S. Takaki, and T. Haranoh, *Electrical and structural properties of low resistivity tin-doped indium oxide films,* Journal of Applied Physics **71**, 3356 (1992).

[289] H. Liu, V. Avrutin, N. Izyumskaya, Ü. Özgür, and H. Morkoç, *Transparent conducting oxides for electrode applications in light emitting and absorbing devices,* Superlattices and Microstructures **48**, 458 (2010).

[290] B. G. Lewis and D. C. Paine, *Applications and processing of transparent conducting oxides,* MRS bulletin **25**, 22 (2000).

[291] D. Menzel and L. Korte, *Evolution of Optical, Electrical, and Structural Properties of Indium Tungsten Oxide upon High Temperature Annealing,* physica status solidi (a) **217**, 2000165 (2020).

[292] Q. Zhang, X. Li, and G. Li, *Dependence of electrical and optical properties on thickness of tungsten-doped indium oxide thin films,* Thin Solid Films **517**, 613 (2008).

[293] T. Gan, J. Li, L. Wu, J. Zhang, X. Hao, Q. Zhang, R. Li, and W. Shi, *High carrier mobility tungsten-doped indium oxide films prepared by reactive plasma deposition in pure argon and post annealing,* Materials Science in Semiconductor Processing **138**, 106257 (2022).

[294] I. Devices-Part, *Part 1-2: Measurement of current-voltage characteristics of bifacial photovoltaic (PV) devices,* IEC TS , 60904 (2019).

[295] A. Tomasi, F. Sahli, J. P. Seif, L. Fanni, S. M. de Nicolas Agut, J. Geissbühler, B. Paviet-Salomon, S. Nicolay, L. Barraud, B. Niesen, *et al.*, *Transparent electrodes in silicon heterojunction solar cells: Influence on contact passivation,* IEEE Journal of Photovoltaics **6**, 17 (2015).

[296] J. Yan, C. Zhang, H. Li, X. Yang, L. Wan, F. Li, K. Qiu, J. Guo, W. Duan, A. Lambertz, *et al.*, *Stable organic passivated carbon nanotube–silicon solar cells with an efficiency of 22%,* Advanced Science **8**, 2102027 (2021).

[297] L. Yu, A. S. Bati, T. S. Grace, M. Batmunkh, and J. G. Shapter, *$Ti_3C_2T_x$ (MXene)-Silicon Heterojunction for Efficient Photovoltaic Cells,* Advanced Energy Materials **9**, 1901063 (2019).

[298] W. Wang, L. Cai, L. Meng, L. Zhang, N. Chen, H. Shen, and Z. Liang, *Cerous fluoride dopant-free electron-selective contact for crystalline silicon solar cells,* Physica Status Solidi (RRL)–Rapid Research Letters **15**, 2100135 (2021).

[299] C. Xing, W. Gu, Z. Xiang, X. Lou, X. Wang, X. Zhang, Y. Wang, X. Yang, and B. Sun, *Post-annealing-free BaO_xF_y/LiF-based stack electron-selective contacts for high efficiency crystalline silicon solar cells featuring ultra-low contact resistivity,* Chemical Engineering Journal **481**, 148568 (2024).

[300] M. Bivour, F. Zahringer, P. Ndione, and M. Hermle, *Sputter-deposited WO_x and MoO_x for hole selective contacts,* Energy Procedia **124**, 400 (2017).

[301] M. Abdelhameed, M. F. Abdelbar, M. Esmat, W. Jevasuwan, and N. Fukata, *Hole-injection role of solution-processed thermally treated VO_x thin films in Si nanowire-based solar cells,* Nano Energy **99**, 107373 (2022).

[302] Z. Xu, S. Peng, H. Lin, S. Tian, Z. Wang, J. He, L. Cai, J. Hou, and P. Gao, *Solution-processed copper-doped chromium oxide with tunable oxygen vacancy for crystalline silicon solar cells hole-selective contacts,* Solar RRL **5**, 2100064 (2021).

[303] B. Macco, M. Bivour, J. Deijkers, S. Basuvalingam, L. Black, J. Melskens, B. Van De Loo, W. Berghuis, M. Hermle, and W. Kessels, *Effective passivation of silicon surfaces by ultrathin atomic-layer deposited niobium oxide,* Applied Physics Letters **112** (2018).

[304] M. Nayak, K. Bergum, G. E. Stan, I.-H. Lee, and A. Kuznetsov, *Sub-Stochiometric Nickel Oxide Hole-Selective Contacts in Solar Cells: Comparison of Simulations and Experiments with Sputtered Films,* Physica Status Solidi (a) **220**, 2200651 (2023).

[305] L. Zhang, J. Qiu, H. Cheng, Y. Zhang, S. Zhong, L. Shi, H. Yin, R. Tong, Z. Sun, W. Shen, *et al.*, *Low-temperature Ta-doped TiO_x electron-selective contacts for high-performance silicon solar cells,* Solar Energy Materials and Solar Cells **266**, 112703 (2024).

[306] Z. Liu, H. Lin, Z. Wang, L. Chen, T. Wu, Y. Pang, L. Cai, J. He, S. Peng, H. Shen, *et al.*, *Dual functional dopant-free contacts with titanium protecting layer: boosting stability while balancing electron transport and recombination losses,* Advanced Science **9**, 2202240 (2022).

[307] Y. Z. Paul Procel and O. Isabella, *To be submitted,* to be submitted (2024).

[308] J. Li, T. Pan, J. Wang, S. Cao, Y. Lin, B. Hoex, Z. Ma, L. Lu, L. Yang, B. Sun, *et al.*, *Bilayer MoO_x/CrO_x Passivating Contact Targeting Highly Stable Silicon Heterojunction Solar Cells,* ACS applied materials & interfaces **12**, 36778 (2020).

[309] M. M. Shehata, T. N. Truong, G. Bartholazzi, D. H. Macdonald, and L. E. Black, *Addressing the stability challenges of TiO_x-based passivating contacts for high-efficiency c-Si solar cells,* Journal of Materials Chemistry A **12**, 8826 (2024).

[310] H. Nasser, G. Kökbudak, H. Mehmood, and R. Turan, *Dependence of n-cSi/MoO_x heterojunction performance on cSi doping concentration,* Energy Procedia **124**, 418 (2017).

[311] H. Nasser, F. Es, M. Zolfaghari Borra, E. Semiz, G. Kökbudak, E. Orhan, and R. Turan, *On the application of hole-selective MoO_x as full-area rear contact for industrial scale p-type c-Si solar cells,* Progress in Photovoltaics: Research and Applications **29**, 281 (2021).

[312] C. Lu, A. B. Prakoso, H. Wang, *et al.*, *Hole selective WO_x and V_2O_x contacts using solution process for silicon solar cells application,* Materials Chemistry and Physics **273**, 125101 (2021).

[313] C. Liu, L. Zhang, G. Yu, T. Wang, X. Wu, L. Xu, P. Lin, C. Cui, X. Yu, and P. Wang, *Tuning oxygen vacancies in vanadium-doped molybdenum oxide for silicon solar cells with hole selective contact,* Materials Science in Semiconductor Processing **146**, 106687 (2022).

[314] M. Mews, L. Korte, and B. Rech, *Oxygen vacancies in tungsten oxide and their influence on tungsten oxide/silicon heterojunction solar cells,* Solar Energy Materials and Solar Cells **158**, 77 (2016).

[315] H.-J. Zhai, B. Kiran, L.-F. Cui, X. Li, D. A. Dixon, and L.-S. Wang, *Electronic Structure and Chemical Bonding in MO_n^- and MO_n Clusters (M= Mo, W; n= 3- 5): A Photoelectron Spectroscopy and ab Initio Study,* Journal of the American Chemical Society **126**, 16134 (2004).

[316] S. F. Vyboishchikov and J. Sauer, *Gas-phase vanadium oxide anions: Structure and detachment energies from density functional calculations,* The Journal of Physical Chemistry A **104**, 10913 (2000).

[317] J. Kumari, J. S. Bhardwaj, Rahul, and P. Agarwal, *Oxygen Plasma Treatment of Thermally Evaporated MoO_{3-x} Films: An Approach to Tune the Work Function,* ACS Applied Electronic Materials **5**, 4103 (2023).

[318] D. Wrana, K. Cieślik, W. Belza, C. Rodenbücher, K. Szot, and F. Krok, *Kelvin probe force microscopy work function characterization of transition metal oxide crystals under ongoing reduction and oxidation,* Beilstein Journal of Nanotechnology **10**, 1596 (2019).

[319] S. Chen, J. R. Manders, S.-W. Tsang, and F. So, *Metal oxides for interface engineering in polymer solar cells,* Journal of Materials Chemistry **22**, 24202 (2012).

[320] Ü. Akın and H. Şafak, *Thickness dependence of dispersion parameters of the MoO_x thin films prepared using the vacuum evaporation technique,* Journal of Alloys and Compounds **647**, 146 (2015).

[321] L. Giordano and G. Pacchioni, *Oxide films at the nanoscale: new structures, new functions, and new materials,* Accounts of Chemical Research **44**, 1244 (2011).

[322] Y. Guo and J. Robertson, *Origin of the high work function and high conductivity of MoO_3,* Applied Physics Letters **105** (2014).

[323] T. Matsui, M. Bivour, M. Hermle, and H. Sai, *Atomic-Layer-Deposited TiO_x Nanolayers Function as Efficient Hole-Selective Passivating Contacts in Silicon Solar Cells,* ACS Applied Materials & Interfaces **12**, 49777 (2020).

[324] T. Matsui, S. McNab, R. S. Bonilla, and H. Sai, *Full-Area Passivating Hole Contact in Silicon Solar Cells Enabled by a TiO_x/Metal Bilayer,* ACS Applied Energy Materials **5**, 12782 (2022).

[325] C. Chen, Y. Jiang, Y. Wu, J. Guo, X. Kong, X. Wu, Y. Li, D. Zheng, S. Wu, X. Gao, *et al.*, *Low-temperature-processed WO_x as electron transfer layer for planar perovskite solar cells exceeding 20% efficiency,* Solar RRL **4**, 1900499 (2020).

[326] H. Sun, X. Hou, Q. Wei, H. Liu, K. Yang, W. Wang, Q. An, and Y. Rong, *Low-temperature solution-processed p-type vanadium oxide for perovskite solar cells.* Chemical Communications **52 52**, 8099 (2016).

[327] J. You, L. Meng, T. Song, T. Guo, Y. Yang, W. Chang, Z. Hong, H. Chen, H. Zhou, Q. Chen, Y. Liu, N. D. Marco, and Y. Yang, *Improved air stability of perovskite solar cells via solution-processed metal oxide transport layers.* Nature Nanotechnology **11 1**, 75 (2016).

[328] J. Peng, T. Duong, X. Zhou, H. Shen, Y. Wu, H. K. Mulmudi, Y. Wan, D. Zhong, J. Li, T. Tsuzuki, *et al.*, *Efficient indium-doped TiO_x electron transport layers for high-performance perovskite solar cells and perovskite-silicon tandems,* Advanced Energy Materials **7**, 1601768 (2017).

[329] Y. Hu, L. Song, Y. Chen, and W. Huang, *Two-terminal perovskites tandem solar cells: recent advances and perspectives,* Solar RRL **3**, 1900080 (2019).

[330] L. Duan, D. Walter, N. Chang, J. Bullock, D. Kang, S. P. Phang, K. Weber, T. White, D. Macdonald, K. Catchpole, *et al.*, *Stability challenges for the commercialization of perovskite–silicon tandem solar cells,* Nature Reviews Materials **8**, 261 (2023).

[331] Y. Lin, W. Yang, H. Gu, F. Du, J. Liao, D. Yu, J. Xia, H. Wang, S. Yang, G. Fang, *et al.*, *Recombination Layers Design and Rational Characterizations for Efficient Two-terminal Perovskite-based Tandem Solar Cells,* Advanced Materials , 2405684 (2024).

[332] W. Chi, S. K. Banerjee, K. Jayawardena, S. R. P. Silva, and S. I. Seok, *Perovskite/silicon tandem solar cells: choice of bottom devices and recombination layers,* ACS Energy Letters **8**, 1535 (2023).

[333] W. Yoon, D. Scheiman, Y. Ok, Z. Song, C. Chen, G. Jernigan, A. Rohatgi, Y. Yan, and P. Jenkins, *Sputtered indium tin oxide as a recombination layer formed on the tunnel oxide/poly-Si passivating contact enabling the potential of efficient monolithic perovskite/Si tandem solar cells,* Solar Energy Materials and Solar Cells **210**, 110482 (2020).

[334] C. McDonald, H. Sai, V. Švrček, A. Kogo, T. Miyadera, T. Murakami, M. Chikamatsu, Y. Yoshida, and T. Matsui, *In Situ Grown Nanocrystalline Si Recombination Junction Layers for Efficient Perovskite-Si Monolithic Tandem Solar Cells: Toward a Simpler Multijunction Architecture.* ACS Applied Materials Interfaces (2022), 10.1021/acsami.2c05662.

[335] R. Sheng, M. T. Hörantner, Z. Wang, Y. Jiang, W. Zhang, A. Agosti, S. Huang, X. Hao, A. Ho-baillie, M. Green, and H. Snaith, *Monolithic Wide Band Gap Perovskite/ Perovskite Tandem Solar Cells with Organic Recombination Layers,* Journal of Physical Chemistry C **121**, 27256 (2017).

[336] L. Mao, T. Yang, H. Zhang, J. Shi, Y. Hu, P. Zeng, F. Li, J. Gong, X. Fang, Y. Sun, *et al.*, *Fully textured, production-line compatible monolithic perovskite/silicon tandem solar cells approaching 29% efficiency,* Advanced Materials **34**, 2206193 (2022).

[337] S. Mahjabin, M. I. Hossain, M. M. Haque, M. Bashar, M. Jamal, M. Shahiduzzaman, G. Muhammad, K. Sopian, and M. Akhtaruzzaman, *Sputtered WO_x thin film as the electron transport layer for efficient perovskite solar cells,* Applied Physics A **128**, 358 (2022).

[338] F. Wang, Y. Zhang, M. Yang, J. Du, L. Xue, L. Yang, L. Fan, Y. Sui, J. Yang, and X. Zhang, *Exploring low-temperature processed a-WO_x/SnO_2 hybrid electron transporting layer for perovskite solar cells with efficiency> 20.5%,* Nano Energy **63**, 103825 (2019).

[339] X. Yang, P. Zheng, Q. Bi, and K. Weber, *Silicon heterojunction solar cells with electron selective TiO_x contact,* Solar Energy Materials and Solar Cells **150**, 32 (2016).

[340] D. Quispe, B. J. Coppa, T. Newhouse-Illige, P. Firth, and Z. C. Holman, *Assessing TiO_x as a hole-selective contact for silicon heterojunction solar cells,* in *2021 IEEE 48th Photovoltaic Specialists Conference (PVSC)* (IEEE, 2021) pp. 1492–1494.

[341] M. De Bastiani, A. S. Subbiah, E. Aydin, F. H. Isikgor, T. G. Allen, and S. De Wolf, *Recombination junctions for efficient monolithic perovskite-based tandem solar cells: physical principles, properties, processing and prospects,* Materials Horizons **7**, 2791 (2020).

[342] T. Becker, S. Trost, A. Behrendt, I. Shutsko, A. Polywka, P. Görrn, P. Reckers, C. Das, T. Mayer, D. Di Carlo Rasi, *et al.*, *All-Oxide MoO_x/SnO_x Charge Recombination Interconnects for Inverted Organic Tandem Solar Cells,* Advanced Energy Materials **8**, 1702533 (2018).

Acknowledgements

Time flies, and perhaps the wheels of fate began turning back at the PVSC conference in 2018. It was then that I first met Prof. dr. Olindo Isabella; we were both at the same poster session, with Prof. dr. Olindo Isabella just standing across from me. The memory of my first interview for the PhD position remains vivid. It's often said that in life, you need someone to believe in you and a mentor to guide you. First and foremost, I would like to express my gratitude to Prof. dr. Olindo Isabella and Prof. dr. Miro Zeman for giving me the opportunity to join PVMD. They provided me with many opportunities to attend international conferences and interact with other researchers. I'm also thankful to Olindo for recognizing my work. Special thanks to my daily supervisor, Dr. Luana Mazzarella, for our daily exchanges, her valuable suggestions, and the inspiration she provided. Thank you all for your support during the thesis writing.

In the group, I met many outstanding peers. Even before I arrived in the Netherlands, I received help from Yifeng Zhao, who eased my concerns during the pandemic by providing detailed information about the situation in Europe and the Netherlands. After arriving, I often felt homesick. Fortunately, I met Jin Yan, who joined around the same time and guided me through Delft, showing me where to purchase essentials. Later, I met Hu Xiao, and through him, I was introduced to the "Group of Six." Miao Xueqing, Zhang Yaqian, Liu Le, and Liu Yigu. They all are good cookers which allowed me to enjoy many delicious meals.

During the start of my experiments in the first year, Yifeng offered me tremendous support. Whenever I encountered any issues in the lab, I could always count on his advice. With his extensive experience, he was always willing to share his knowledge. Most of what I know about practical lab work, I learned from him. In life, he also became a good friend,

and our shared interest in cycling led us to purchase road bikes and gear together. Yifeng is incredibly meticulous; after careful comparison, he decided on the bike we bought, and we also discussed and purchased many cycling accessories together. In the summer of 2022, we cycled hundreds of kilometers together, but our rides were put on hold during his dissertation writing. I hope we can ride together again soon.

I would also like to give special thanks to Paul Procel. He is like a kind elder brother. We co-authored my first paper, and I learned a lot about writing from him. I often discussed various challenges I encountered with him. As one of the smartest people I know, he always had advice and answers to offer. I am also very grateful to Engin; your humor and wit always made our coffee breaks relaxing. You have always been my No. 1.

I also want to thank Jian Zhang. By chance, we met on the basketball court, and for some reason, there was an instant sense of familiarity. Jian is a person who truly knows how to live; having lived in Delft for four years, he was much more experienced than I was. He introduced me to nice supermarkets in Delft and took me to the outdoor market in The Hague. Knowing that I love eating meat, he even introduced me to a butcher in Rotterdam, and we rode there together to buy meat. As a warm-hearted dongbeier, Jian also invited me to taste the famous dish "Di San Xian," which I successfully learned to cook and have now come to love. Through basketball, I also met Rui Yan, Hanqing Liu, Mingyan Fu, Zhiqiang Peng, and Chao Ma. I still remember the days of playing basketball and then eating, drinking, and chatting with the guys afterward. I also met Zichao Li through working out, and in this final year, working out together became my best way to relax during thesis writing.

I am also very grateful to Guangtao Yang and Can Han. Our discussions provided me with a lot of inspiration. I sincerely thank Zhirong Yao, Lory, Haoxu Wang, Yinwen Zhao, Yi Zheng, and Wenxian Wang. Being with you all felt like being home again. I also want to thank David van Nijen. I enjoy the days we were office mates and I am grateful for your invitation to visit your home. I would also like to thank Katarina Kovačević; we

shared similar topics and had many fruitful discussions. I would like to thank Peer Sluijs for helping me with the translation of the summary. I would like to thank Paula Perez Rodriguez for the chill talks during coffee breaks. I am grateful to meet all the colleagues in PVMD groups, you are so kind and helpful.

I am deeply thankful to my girlfriend for bringing so much joy to my life. Before, my weekends were only about working out, playing basketball, and cycling—an unchanging routine. Since you came into my life, we've hiked together, watched movies, cooked, traveled, and visited many places I had never been. During my thesis writing period, you were my reliable support, allowing me to fully focus on my writing, which enabled me to complete my thesis ahead of schedule. I also want to thank the game Rusty Lake, which brought us closer together.

Finally, I want to thank my parents for their love and support. You always try to give me the best. I love you both. I am happy to be your child. I wish for your continued good health, granting me ample opportunity to properly express my love and repay all that you have done for me.

感谢相遇！

List of Publications

Peer-reviewed journal articles

First-authored peer-reviewed journal articles

1. **L. Cao**, **P. Procel**, A. Alcañiz, J. Yan, F. Tichelaar, E. Özkol, Y. Zhao, C. Han, G. Yang, Z. Yao, M. Zeman, R. Santbergen, L. Mazzarella, and O. Isabella, *Achieving 23.83% conversion efficiency in silicon heterojunction solar cell with ultra-thin MoO_x hole collector layer via tailoring (i)a-Si:H/MoO_x interface*, Progress in Photovoltaics: Research and Applications, **31**, 1245-1254, (2022). † ‡

2. **L. Cao**, Y. Zhao, P. Procel, C. Han, K. Kovačević, E. Özkol, M. Zeman, L. Mazzarella, and O. Isabella, *Indium reduction in bifacial silicon heterojunction solar cells with MoO_x hole collector*, Advanced Energy and Sustainability Research, 2400105, (2024).

3. **L. Cao**, Y. Zhao, J. Yan, E. Özkol, K. Kovačević, M. Zeman, L. Mazzarella, and O. Isabella, *Universal method for applying transition metal oxides in silicon heterojunction solar cells*, Solar Energy Materials and Solar Cells, **278**, 113170, (2024).

Co-authored peer-reviewed journal articles

1. K. Kovačević, , Y. Zhao, P. Procel, **L. Cao**, L. Mazzarella, and O. Isabella, *Interdigitated-back-contacted silicon heterojunction solar cells featuring novel MoO_x-based contact stacks*, Progress in Photovoltaics: Research and Applications, (2024).

2. Y. Zhao, P. Procel, C. Han, **L. Cao**, G. Yang, E. Özkol, A. Alcañiz, K. Kovačević, G. Limodio, R. Santbergen, A. Smets, A. Weeber, M. Zeman, L. Mazzarella, and O. Isabella, *Strategies for realizing high-efficiency silicon heterojunction solar cells*, Solar Energy Materials and Solar Cells, **258**, 112413, (2023).

3. Y. Zhao, P. Procel, A. Smets, L. Mazzarella, C. Han, G. Yang, **L. Cao**, Z. Yao, A. Weeber, M. Zeman, and O. Isabella, *Effects of (i)a-Si:H deposition temperature on high-efficiency silicon heterojunction solar cells*, Progress in Photovoltaics: Research and Applications, **31**, 1170-1180, (2021).

4. Z. Yao, G. Yang, C. Han, P. Procel, E. Özkol, J. Yan, Y. Zhao, **L. Cao**, R. van Swaaij, L. Mazzarella, and O. Isabella, *Poly-SiOx Passivating Contacts with Plasma-Assisted N2O Oxidation of Silicon (PANO-SiOx)*, Solar RRL, 2300186, (2023).

---

† L. Cao and P. Procel contributed equally to this work.

‡ This work is also reported by PV Magazine via *https://www.pv-magazine.com/2022/11/03/silicon-heterojunction-solar-cell-with-23-83-efficiency-via-molybdenum-oxide-hole-collector/*.

Patent applications

1. P. Procel, Y. Zhao, **L. Cao**, K. Kovačević, and O. Isabella, Simplified processing of interdigitated-back-contacted silicon heterojuntion solar cells, the Netherlands, NL2033406.

2. **L. Cao**, P. Procel, Y. Zhao, L. Mazzarella, M. Zeman, O. Isabella and K. Kovačević, TMO as recombination junction in tandem solar cells, the Netherlands, unfiled. [§]

Conference contributions

First-authored conference contributions

1. Poster presentation @ PVSEC-35 : **Liqi Cao**, Roel Theeuwes, Yifeng Zhao, Paul Procel, Erwin Kessels, Miro Zeman, Luana Mazzarella, and Olindo Isabella, *ALD-TiO_x and PVD-MoO_x in dopant-free silicon heterojunction solar cells*, Numazu, Japan, 2024.

2. Poster presentation @ EU PVSEC 2024: **Liqi Cao**, Paul Procel, Yifeng Zhao, Luana Mazzarella, Katarina Kovačević, Engin Özkol, Miro Zeman, and Olindo Isabella, *Universal interface treatment for dopant-free materials applied to silicon heterojunction solar cells*, Bilbao, Spain, 2024.

3. Oral presentation @ SiliconPV 2024: **Liqi Cao**, Paul Procel, Yifeng Zhao, Luana Mazzarella, Katarina Kovačević, Engin Özkol, Miro Zeman, and Olindo Isabella, *Universal Method for Applying Transition Metal Oxides in Silicon Heterojunction Solar Cells*, Chamberry, France, 2024.

4. Oral presentation @ PVSEC-34: **Liqi Cao**, Paul Procel, Yifeng Zhao, Luana Mazzarella, Katarina Kovačević, Miro Zeman, and Olindo Isabella, *Universal Interface Treatment for applying Transition Metal Oxides in Silicon Heterojunction Solar Cells*, Shenzhen, China, 2023.[¶]

5. Oral presentation @ EU PVSEC 2023: **Liqi Cao**, Paul Procel, Luana Mazzarella, Yifeng Zhao, Can Han, Katarina Kovačević, Engin Özkol, Zhirong Yao, Miro Zeman, and Olindo Isabella, *Cu-Plated Bifacial Silicon Heterojunction Solar Cells With MoO_x as Hole Collector and ultra-thin TCO layers*, Lisbon, Portugal, 2023.

6. Oral presentation @ SiliconPV 2023: **Liqi Cao**, Paul Procel, Luana Mazzarella, Yifeng Zhao, Can Han, Katarina Kovačević, Engin Özkol, Zhirong Yao, Miro Zeman, and Olindo Isabella, *Cu-Plated Bifacial Silicon Heterojunction Solar Cells With MoO_x as Hole Collector and ultra-thin TCO layers*, Delft, Netherlands, 2023.

7. Oral presentation @ MRS Fall 2022: **Liqi Cao**, Luana Mazzarella, Paul Procel, Yifeng Zhao, Jin Yan, Can Han, Guangtao Yang, Zhirong Yao, Miro Zeman, and Olindo Isabella, *Interface Treatment for High-Efficient Dopant-Free MoO_x Silicon Heterojunction Solar Cells*, online, 2022.

8. Oral presentation @ PVSEC-33: **Liqi Cao**, Luana Mazzarella, Paul Procel, Yifeng Zhao, Jin Yan, Can Han, Guangtao Yang, Zhirong Yao, Miro Zeman, and Olindo Isabella, *Interface*

[§] L. Cao and P. Procel are co-first authors.
[¶] This work has won "Student Award" at PVSEC 2023.

Treatment for High-Efficient Dopant-Free MoO_x Silicon Heterojunction Solar Cells, Nagoya, Japan, 2022.‖

9. Oral presentation @ 8th World Conference on Photovoltaic Energy Conversion: **Liqi Cao**, Luana Mazzarella, Paul Procel, Yifeng Zhao, Jin Yan, Can Han, Guangtao Yang, Zhirong Yan, Miro Zeman, and Olindo Isabella, *Interface Treatment for High-Efficient Dopant-Free MoO_x Silicon Heterojunction Solar Cells*, Milan, Italy, 2022.

10. Oral presentation @ MRS Fall meeting: **Liqi Cao**, Yifeng Zhao, Can Han, Guangtao Yang, Miro Zeman, Luana Mazzarella and Olindo Isabella, *The application of ultra-thin MoO_x in silicon heterojunction solar cells*, online, 2022.

11. Poster presentation @ 5th International workshop on Silicon Heterojunction solar cells: **Liqi Cao**, Paul Procel, Luana Mazzarella, Yifeng Zhao, Engin Özkol, Jin Yan, Can Han, Guangtao Yang, Miro Zeman, and Olindo Isabella, *The application of ultra-thin MoO_x in c-Si heterojunction solar cells*, Aix-les-Bains, France, 2022.

Conference proceeding

1. Invited talk @ ECS meeting 2023: Olindo Isabella, **Liqi Cao**, Paul Procel, Luana Mazzarella, Yifeng Zhao, Engin Özkol, Jin Yan, Can Han, Guangtao Yang and Miro Zeman *Interface Treatments for High-Efficiency MoO_x Based Silicon Heterojunction Solar Cells* , Gothenburg, Sweden, 2023.

Co-authored conference contributions

1. Poster presentation @ SiliconPV 2024: Engin Özkol, Maria Magalhães, Yifeng Zhao, **Liqi Cao**, Paula Perez RodriguezKatarina, Kovačević, Paul Procel, Manuel João de Moura Dias Mendes, Miro Zeman, and Olindo Isabella, *Understanding the electron transport mechanisms in MoO_x-based layer stack for application in simplified IBC-SHJ solar cells*, Chamberry, France, 2024.

2. Poster presentation @ SiliconPV 2024: Katarina Kovačević, Yifeng Zhao, Paul Procel, **Liqi Cao**, Luana Mazzarella, and Olindo Isabella, *Optimization of RF Sputtered ICO(:H) Thin Films Fabricated at Room Temperature for SHJ Solar Cell Applications*, Chamberry, France, 2024.

3. Oral presentation @ SiliconPV 2023: Yifeng Zhao, Paul Procel, Can Han, Luana Mazzarella, **Liqi Cao**, Guangtao Yang, Rudi Santbergen, Katarina Kovačević, Alba Alcañiz, Gianluca Limodio, Engin Özkol, Arno Smets, Arthur Weeber, Miro Zeman, and Olindo Isabella, *Strategies for realizing high-efficiency silicon heterojunction solar cells featuring reduced consumption of indium and silver*, Delft, Netherlands, 2023.

4. Oral presentation @ PVSEC-33: Yifeng Zhao, Can Han, Paul Procel, Arno Smets, Luana Mazzarella, Guangtao Yang, **Liqi Cao**, Zhirong Yao, Authur Weeber, Miro Zeman, and Olindo Isabella, *Effects of (i)a-Si:H deposition temperature and strategies to reduce In-based TCO and Ag use in high-efficiency SHJ solar cells*, Nagoya, Japan, 2022.

5. Oral presentation @ WCPEC-8: Yifeng Zhao, Paul Procel, Luana Mazzarella, Can Han, Guangtao Yang, **Liqi Cao**, Zhirong Yao, Dong Zhang, Valerio Zardetto, Mehrdad Najafi, Adriana

‖This work has won "Student Award" at PVSEC 2022.

Creatore, René Janssen, Sjoerd Veenstra, Gianluca Coletti, Arthur W. Weeber, Miro Zeman, Olindo Isabella, *Effects of (i)a-Si:H Deposition Temperature on High-Efficiency Silicon Heterojunction Solar Cells for High-Efficiency Four-Terminal Tandem Solar Cells*, Milan, Italy, 2022. **

6. Oral presentation @ WCPEC-8: Paul Procel, Alba Alcañiz, **Liqi Cao**, Luana Mazzarella, Yifeng Zhao, Can Han, Guangtao Yang, Rudi Santbergen, Miro Zeman, and Olindo Isabella, *Insights into MoOx/i-aSi:H interface for high efficiency solar cells*, Milan, Italy, 2022.

7. Poster presentation @ SiliconPV 2022: Zhirong Yao, Guangtao Yang, Can Han, Paul Procel, Yifeng Zhao, **Liqi Cao**, Roald van der Kolk, Luana Mazzarella, Miro Zeman, and Olindo Isabella, *PECVD Plasma-SiOx/poly-SiOx Passivating Contacts*, Konstanz, Germany, 2022. ††

8. Oral presentation @ PVSC-49: Yifeng Zhao, Paul Procel, Arno Smets, Luana Mazzarella, Can Han, Guangtao Yang, **Liqi Cao**, Zhirong Yao, Authur Weeber, Miro Zeman, and Olindo Isabella, *Effects of (i)a-Si:H Deposition Temperature on High-Efficiency Silicon Heterojunction Solar Cells*, Philadelphia, USA, 2022.

9. Oral presentation @ SiliconPV 2022: Paul Procel, Alba Alcañiz, **Liqi Cao**, Luana Mazzarella, Yifeng Zhao, Can Han, Guangtao Yang, Rudi Santbergen, Miro Zeman, and Olindo Isabella, *Insights into MoOx/i-aSi:H interface for high efficiency solar cells*, Konstanz, Germany, 2022.

10. Oral presentation @ Metallisation and Interconnection Workshop 2021: Can Han, Guangtao Yang, Daragh O'Connor, Yifeng Zhao, Anirudh Gopalakrishnan, **Liqi Cao**, Paul Procel, Xiaodan Zhang, Miro Zeman, Luana Mazzarella, and Olindo Isabella, *Controllable simultaneous bifacial Cu-plating for high efficiency crystalline silicon solar cells*, Genk, Belgium, 2021.

11. Invited talk @ the 4th international workshop on SHJ solar cells: Can Han, Guangtao Yang, Daragh O'Connor, Yifeng Zhao, Anirudh Gopalakrishnan, **Liqi Cao**, Paul Procel, Xiaodan Zhang, Miro Zeman, Luana Mazzarella, and Olindo Isabella, *Controllable simultaneous bifacial Cu-plating for high efficiency crystalline silicon solar cells*, online, 2021.

**This work has won "Student Award" at WCPEC-8 2022.
††This work has won "SiliconPV Poster Award" at SiliconPV 2022.

Curriculum Vitae

Liqi Cao

Oct. 2020 – Aug. 2024	Ph.D candidate in Photovoltaic Materials and Devices group Delft University of Technology, Delft, the Netherlands **Thesis**: Transition metal oxides as selective carrier transport layers in silicon heterojunction solar cells **Promotors**: Prof. dr. Miro Zeman Prof. dr. Olindo Isabella
Sep. 2017 – July 2020	M.Sc Material Science East China University of Science and Technology, Shanghai, China **Thesis**: Study on preparation of passivation layer of crystalline silicon solar cells by sol-gel method **Supervisors**: Prof. Xiao Yuan Prof. dr. Hongbo Li
Sep. 2012 – July 2016	B.Sc Inorganic Non-metallic Materials Science and Engineering East China University of Science and Technology, Shanghai, China **Thesis**: Photovoltaic system efficiency analysis **Supervisor**: Dr. Guoqiang Hao